CHAPTER 2

Acylpyrazolone ligands and their Uranyl metal complexes: Synthesis, Characterization and Structural Features.

Part (a): Synthesis, Characterization and Crystal Features of Bidentate and Tridentate acylpyrazolone ligands.

2a.1 Introduction

The widely recognized synthesis of pyrazolone is used to generate a diverse range of compounds, holding significant promise for progress in medicinal and coordination chemistry [1]. Acyl Pyrazolone exhibits diverse electrical, optical, and biological activities within the realm of science [2]. It is a significant component of the pyrazolone family, characterized by a five-membered heterocyclic backbone. Its exclusive attraction lies in its coordination background, attributed to two adjacent heterocyclic nitrogen atoms and an additional C=O group. Of particular interest are derivatives of 4-acyl pyrazolone due to their chelating arm containing β-diketone in the structure. As per Jensen [3], Acylation readily occurs at the C-4 position of the pyrazole ring in basic conditions, such as calcium hydroxide in dioxane at reflux. Subsequent treatment with an acid-aqueous solution yields acyl pyrazolone in high yield as a solid powder insoluble in water. Numerous derivatives of acyl pyrazolones have been synthesized, primarily through facile functionalization using the acyl (-COR) group on the fourth carbon of pyrazolone and reaction with selected amines. It's frequent to encounter numerous acylated pyrazolones and their complexes exhibiting various geometries [2,4].

The acylation method is gaining popularity for synthesising chelating ligands with expanding donor atom capabilities. A characteristic reaction of acylpyrazolones involves the synthesis of Schiff bases, which enhances donor capacity and denticity within the coordination environment [5]. Under acidic conditions, the amine group undergoes a reaction with the carbonyl of acylpyrazolone, resulting in the formation of a ligand containing a C=N bond. Schiff bases derived from hydrazine-based compounds with acylpyrazolones have various applications [6–10]. Notably, tridentate ligands derived from benzohydrazides are renowned for their O-N-O donor sites [11,12]. These ligands can form complexes with transition and inner transition metals, exhibiting diverse geometries such as pentagonal bipyramidal, tricapped trigonal prismatic, and square antiprismatic [5]. It is crucial, invaluable, and informative in the field of research to assess the crystal strength of acylpyrazolones through various characterization methods. This evaluation helps in understanding the interaction energy and covalency between metal-ligand bonds, which are fundamental aspects influencing the properties of complexes. Considering these aspects, this chapter elucidates the synthesis and characterization of bidentate and tridentate acylpyrazolone ligands.

2a.2 Experimental section

2a.2.1 Materials and Methods

All chemicals used in the current study underwent purification using standard methods [13]. The pyrazolone source and 3,5-dimethyl-benzoyl chloride were provided as complimentary samples by Sidhdhanath Industries, Sachin (Surat), India, and Shiva Pharmachem Limited, Vadodara (Gujarat), respectively. AR-grade solvents for recrystallization were procured from Central Drug House (P) Ltd. (CDH) chemicals.

2a.2.2 Synthesis of ligands

Three ligands denoted as HL^1 (p-chlorobenzoyl 1-phenyl 3-methyl 5-pyrazolone), HL^2 (p-chlorobenzoyl 1-(m-chlorophenyl) 3-methyl 5-pyrazolone), and HL^3 (p-chlorobenzoyl 1-(p-tolyl) 3-methyl 5-pyrazolone), were directly synthesized and used as mentioned in our research group publications [11,14]. Figure 2a.1 represents the structures of HL^1, HL^2, and HL^3 ligands. Bidentate ligands HL^4, HL^5, and HL^6 were synthesized according to the procedure outlined in Figure 2a.2 and recrystallized using rectified spirit.

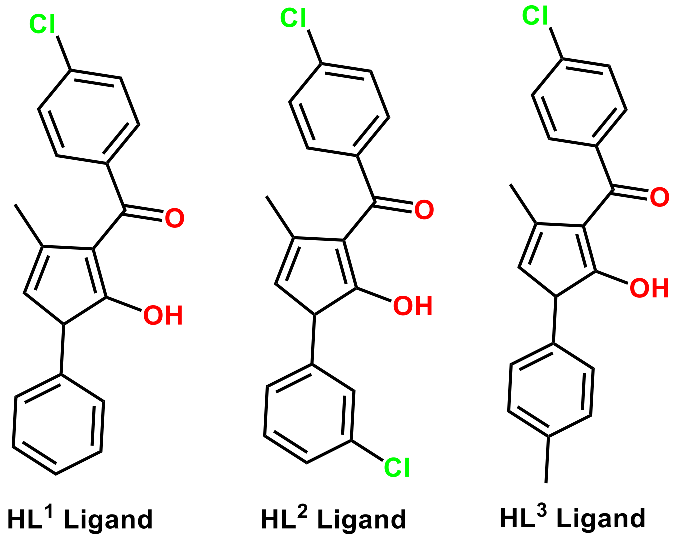

Figure 2a.1 Structures of HL^1, HL^2, and HL^3 ligands.

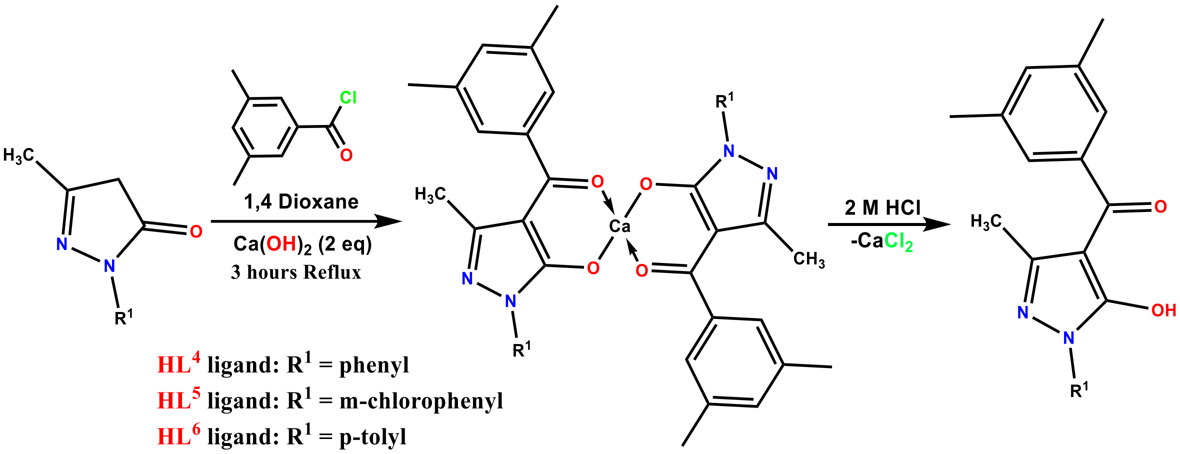

Figure 2a.2 Synthetic route for HL^4, HL^5, and HL^6 ligands.

Synthesis of HL^4 ligand

The ligand HL^4 was synthesized and recrystallized in the enol form using rectified spirit. The synthesis involved the combination of 1 eq 1-phenyl-3-methyl-5-pyrazolone (50 mmol, 8.7 g), 40 ml of 1,4-dioxane, 2 eq $Ca(OH)_2$, and 1 eq 3,5-dimethyl-benzoyl chloride (50 mmol, 7.668 ml), followed by treatment with 2 M HCl (200 ml). This resulted in the formation of bright, pale yellow, shiny prism-type crystals. Yield (%): 93.34%, M.P.: 142 °C, Molecular formula: $C_{19}H_{18}N_2O_2$, Formula wt: 306.37, Λ_M = 3 Ω^{-1} cm^2 mol^{-1}. Mass peaks (see Figure 2a.3) (m/z) = 306.19 (96.34%, $[C_{19}H_{18}N_2O_2]^+$), 291.04 (48.77%, $[C_{18}H_{15}N_2O_2]^+$), 200.09 (100%, $[C_{11}H_8N_2O_2]^+$), 133.11 (38.46%, $[C_9H_9O]^+$), 105.10 (45.09%, $[C_8H_9]^+$), 77.11 ($[C_6H_5]^+$). **FTIR (KBr, cm^{-1}):** 2862 (m, $\upsilon_{\text{O-H stretching}}$), 1595 (s, $\upsilon_{\text{C=O acyl}}$), 1527 (s, $\upsilon_{\text{C=N cyclic}}$). **^{1}H-NMR δ-ppm (400MHz, $CDCl_3$):** 2.135 (s, 3H, $CH_{3(\text{pyz})}$), 7.0-8.0 (m, Ar-H_{L4}), 2.419 (s, 6H, benzoyl-CH_3). **^{13}C-NMR δ-ppm (100 MHz, $CDCl_3$):** 15.91 (pyrazolone CH_3), 21.24 (Dimethyl-benzoyl ring CH_3), 103.61 (pyrazolone ring-C), 120.73, 125.69, 126.63, 129.14, 133.52, 137.29, 137.38, 138.14, 148.06, 161.66 (C-O), 192.18 (C=O).

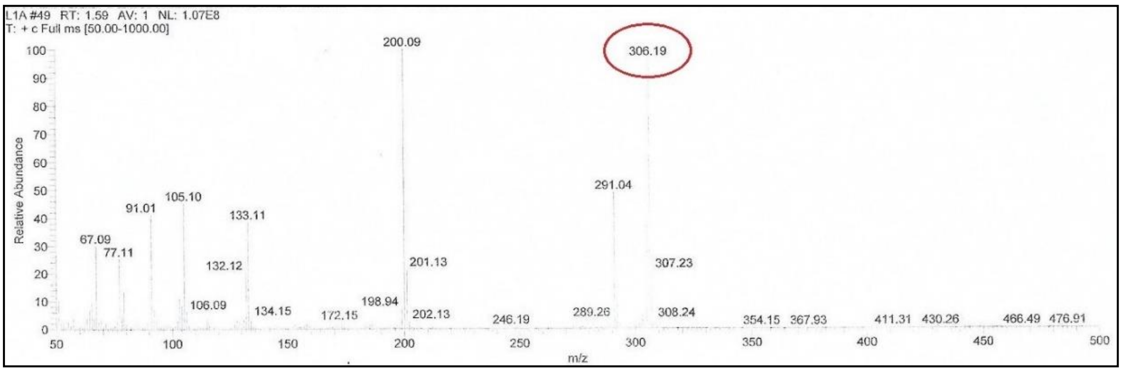

Figure 2a.3 Mass spectrum of HL^4 ligand.

Synthesis of HL^5 ligand

The ligand HL^5 was synthesized and recrystallized in the enol form using rectified spirit. The synthesis involved the combination of 1 eq 1-(m-chlorophenyl)-3-methyl-5-pyrazolone (50 mmol, 10.425 g), 40 ml of 1,4-dioxane, 2 eq $Ca(OH)_2$, and 1 eq 3,5-dimethyl-benzoyl chloride (50 mmol, 7.668 ml), followed by treatment with 2 M HCl (200 ml). This resulted in the formation of bright, colourless, needle-type crystals. Yield (%): 89.8%, M.P.: 110 °C, Molecular formula: $C_{19}H_{17}ClN_2O_2$, Formula wt: 340.10, Λ_M = 5.06 Ω^{-1} cm^2 mol^{-1}. Mass peaks (see Figure 2a.4) (m/z) = 340.15 (43.84%, $[C_{19}H_{17}ClN_2O_2]^+$), 325.11 (26.85%, $[C_{19}H_{16}ClN_2O]^+$), 233.98 (100%, $[C_{11}H_8ClN_2O_2]^+$), 133.10 (63.85%, $[C_9H_9O]^+$), 110.94 (18.79%, $[C_6H_4Cl]^+$), 105.09 (83.61 %, $[C_8H_9]^+$). **FTIR (KBr, cm^{-1}):** 1621 (s, $\upsilon_{C\text{-}O\ \text{dimethyl-benzoyl}}$), 1589 (s, $\upsilon_{C=O\ \text{acyl-pyz}}$), 1554 (s, $\upsilon_{C=N\ \text{acyl-pyz}}$). **^{1}H-NMR δ-ppm (400MHz, $CDCl_3$):** 2.127 ($CH_{3(pyz)}$, s, 3H), 7.2-8.0 (ArH, m), 2.421 (dimethyl-benzoyl-CH_3, s, 6H). **^{13}C-NMR δ-ppm (100 MHz, $CDCl_3$):** 16.00 (acylpyz-CH_3), 21.24 (dimethyl-benzoyl-CH_3), 103.85 (acylpyz ring-C), 118.13, 120.35, 125.81, 126.31, 130.14, 133.76, 134.86, 136.57, 138.21, 138.44, 148.37 (C-O), 190.83 (C=O).

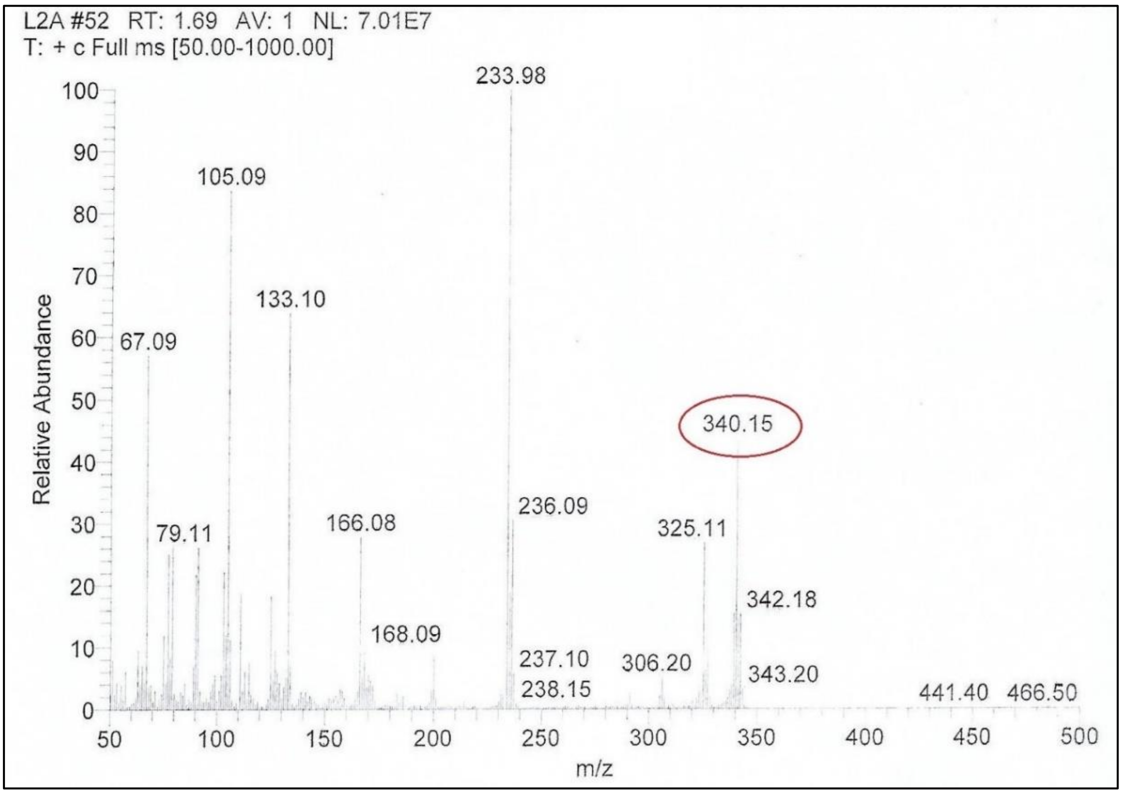

Figure 2a.4 Mass spectrum of HL^5 ligand.

Synthesis of HL^6 ligand

The ligand HL^6 was synthesized by taking the combination of 1 eq 1-(p-tolyl)-3-methyl-5-pyrazolone (50 mmol, 10.425 g), 40 ml of 1,4-dioxane, 2 eq $Ca(OH)_2$, and 1 eq 3,5-dimethyl- benzoyl chloride (50 mmol, 7.668 ml), followed by treatment with 2 M HCl (200 ml). Yield (%): 86.73, M.P.: 130-135 °C, Molecular formula: $C_{20}H_{20}N_2O_2$, Formula wt: 320.39, $\Lambda_M = 3\ \Omega^{-1}\ cm^2\ mol^{-1}$. Mass peaks (see Figure 2a.5) (m/z) = 320.23 (52.88%, $[C_{20}H_{20}N_2O_2]^+$), 305.19 (24.38%, $[C_{19}H_{17}N_2O_2]^+$), 304.16 ($[C_{20}H_{20}N_2O]^+$), 214.07 (69.36%, $[C_{12}H_{11}N_2O_2]^+$), 146.16 (8.28%, $[C_9H_8N_2]^+$), 133.12 (50.90%, $[C_9H_{10}O]^+$), 105.09 (100%, $[C_8H_9]^+$), 91.11 (38.45%, $[C_7H_7]^+$). **FTIR (KBr, cm^{-1}):** 1621 (s, $\upsilon_{\text{C-O dimethyl-benzoyl}}$), 1547 (s, $\upsilon_{\text{C=O acyl-pyz}}$), 1422 (s, $\upsilon_{\text{C=N acyl-pyz}}$). **^{1}H-NMR δ-ppm (400MHz, DMSO-d$_6$):** 2.501 ($CH_{3(pyz)}$, s, 3H), 7.2-8.0 (ArH, m), 2.082 (dimethyl-benzoyl-CH_3, s, 6H), 2.322 (p-tolyl-CH_3, s, 3H). **^{13}C-NMR δ-ppm (100 MHz, DMSO-d$_6$):** 14.9 (acylpyz-CH_3), 21.23 (dimethyl-benzoyl-CH_3), 21 (p-tolyl-CH_3) 104.79 (acylpyz ring-C), 121.76, 126.78, 129.88, 133.57, 135.10, 136.12, 137.66, 139.41, 149, 168 (C-O), 190.44 (C=O).

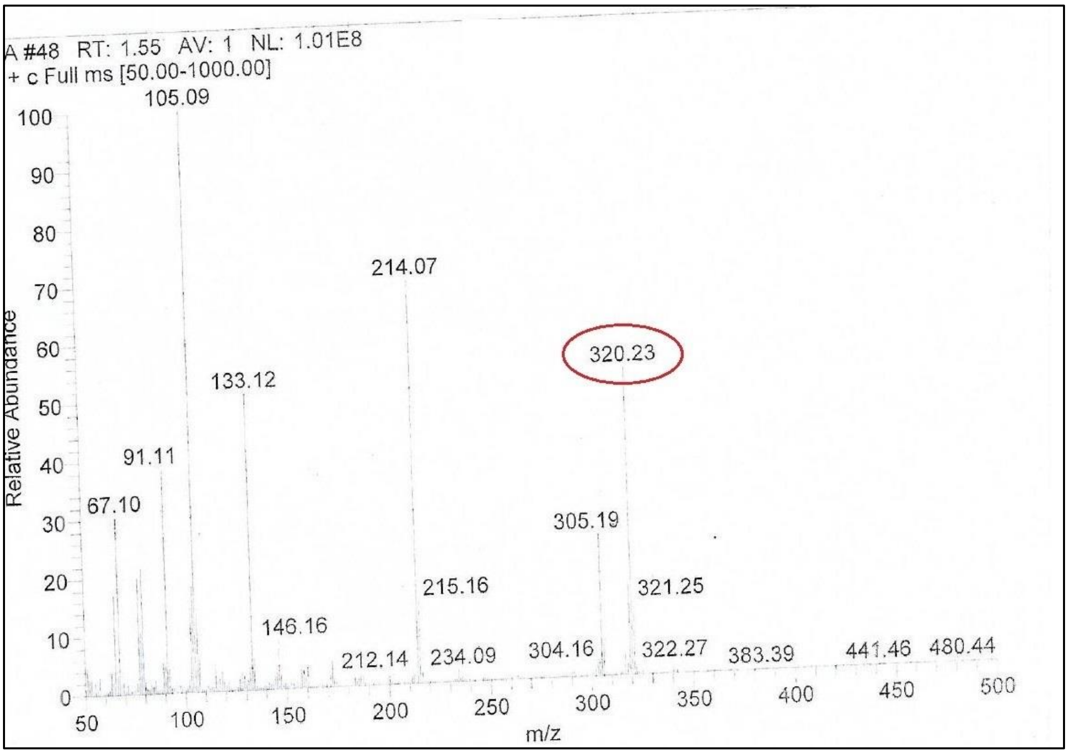

Figure 2a.5 Mass spectrum of HL^6 ligand.

Synthesis of HL^7 ligand

Bright yellow crystals of (E)-N'-((1-(3-chlorophenyl)-5-hydroxy-3-methyl-1H-pyrazol-4-yl)(3,5-dimethylphenyl)methylene)benzohydrazide ligand (**HL^7**) were directly obtained by applying Schiff base reaction between 1 eq ethanolic HL^5 solution (1 mmol, 0.340 g) and 1 eq ethanolic benzoichydrazide solution (1 mmol, 0.136 g) at 80 °C with constant stirring in the R.B. flask for 3-4 hours as illustrated in Figure 2a.6. 2-3 drops of glacial acetic acid were added as a catalyst. Yield (%): 93.04%, M.P.: 200 °C, Molecular formula: $C_{26}H_{23}ClN_4O_2$, Formula wt: 458.95, $\Lambda_M = 4.23\ \Omega^{-1}\ cm^2\ mol^{-1}$. **FTIR (KBr, cm^{-1}):** 3439 (w, $\upsilon_{\text{N-H near to acylpyz}}$), 2988 (w, $\upsilon_{\text{N-H near BZ}}$), 1640 (s, $\upsilon_{\text{C=O BZ group}}$), 1595 (s, $\upsilon_{\text{C=O acylpyz}}$), 1518, 1482 (s, $\upsilon_{\text{C=N acylpyz}}$). **^{1}H-NMR δ-ppm (400MHz, $CDCl_3$):** 15.509 (s, 1H, near BZ), 2.388 (s, 3H, $CH_{3(\text{dimethyl-benzoyl})}$), 2.261 (s, 3H, $CH_{3(\text{dimethyl-benzoyl})}$), 1.59 (s, 3H, $CH_{3(\text{acylpyz})}$), 7.0-8.0 (m, Ar-H). **^{13}C-NMR δ-ppm (100 MHz, $CDCl_3$):** 14.07 (acylpyz-CH_3), 21.21 (dimethyl-benzoyl-CH_3), 98.67, 117.77, 119.94, 124.88, 127.55, 128.92, 129.81, 130.58, 132.91, 134.48, 134.88, 139.43, 139.98, 149.81, 154.71 (C=N), 160.96 (C-O), 163.81 (C=O).

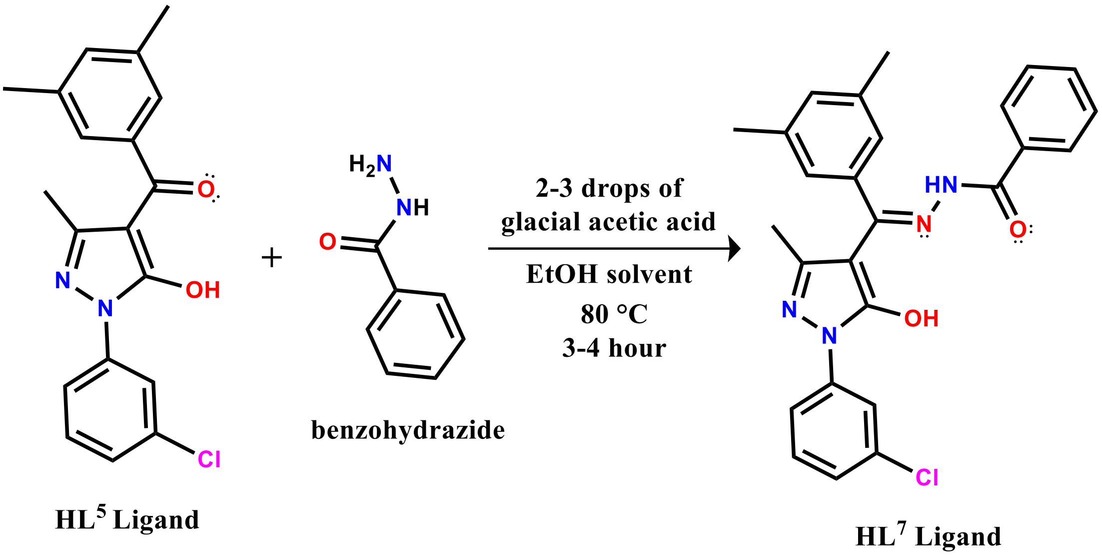

Figure 2a.6 Synthetic route for HL^7 ligand.

2a.2.3 X-ray crystallographic examination

X-ray crystallographic analysis was conducted for all ligands employing graphite monochromator and Mo—Kα (λ = 0.71073Å) radiation. The detector and refinement procedures followed protocols outlined in previously published papers from our laboratory [15]. The diffraction data were processed using SHELXT software [16], while calculations were performed using the SHELXL-2018/3 crystallographic software package [17].

2a.2.4 Physical measurements and characterization techniques

FTIR spectra were acquired using a Bruker alpha FTIR spectrophotometer with 4 scans. ^{1}H and ^{13}C NMR spectra of all ligands were obtained using a Bruker AV 400 MHz instrument, $CDCl_3$/DMSO-d_6 as solvents and TMS as an internal reference. Electronic spectra with the 200-800 nm range were measured with a Perkin Elmer Lambda 35 UV-VIS spectrophotometer. Molar conductivity of 1×10^{-3} M solutions of the ligands in DMSO solvent was measured using a model EQ664A digital direct reading deluxe digital conductivity meter.

2a.2.5 Computational study

DFT calculations and geometry optimizations were conducted using Gauss View 6.0 software at the B3LYP level with a 6-31G basis set for ligands HL^4, HL^5, and HL^7. It is noted that calculations from different basic sets yield comparable results. The Gaussian 16 program was employed for further calculations, including examining the molecular structure, energy gap ($\Delta E_{HOMO\text{-}LUMO}$), frontier orbitals, Mulliken charge, vibrational analysis, and other relevant parameters.

2a.3 Results and Discussion

2a.3.1 FTIR spectral analysis of ligands

FTIR studies offer valuable insights into the coordination sites of the ligand. A comparative examination of the FTIR spectra reveals common bands among ligands. Thus, only significant bands are discussed, whether shifted or newly appearing. Crucial insights into ligand formation can be gleaned from the FTIR spectra, particularly by analysing their C=O, C=N, C-C, and N-N vibrations. The stretching vibrations (υ) of the dimethyl-benzoyl (C=O) are detected for ligand HL^4 at 1621 cm^{-1}, for ligand HL^5 at 1621 cm^{-1}, and for ligand HL^6 at 1622 cm^{-1}, respectively. Ligand HL^7 have an intense band at 1640 cm^{-1} corresponding to stretching vibrations (υ) of the benzoic hydrazide (C=O) group. Similarly, the stretching vibrations (υ) of the acyl (C=O) are detected for ligands HL^4, HL^5, HL^6, and HL^7 at 1605, 1589, 1607, and 1595 cm^{-1}, respectively. Additionally, the vibrational frequencies $\upsilon_{C=N\ cyclic}$, $\upsilon_{N\text{-}N}$ and $\upsilon_{C\text{-}C\ aromatic}$ vibrations are also noteworthy, as listed in Table 2a.1. The FTIR spectra of all the ligands mentioned above are illustrated in Figures 2a.7-2a.10.

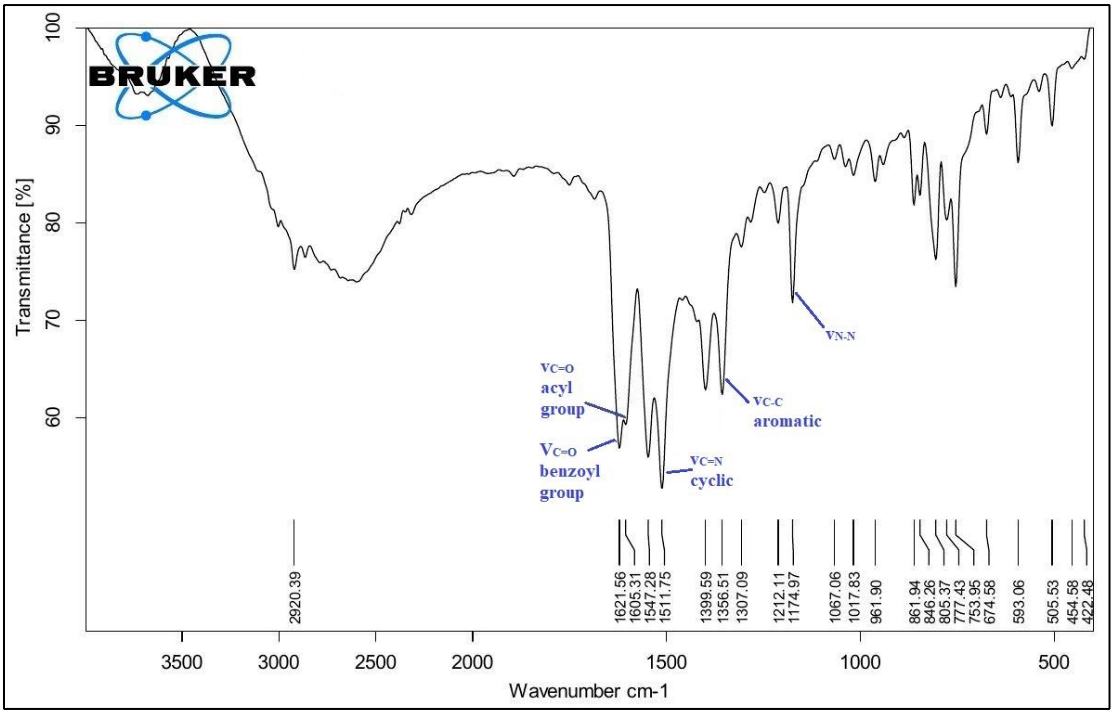

Figure 2a.7 FTIR spectrum of HL^4 ligand.

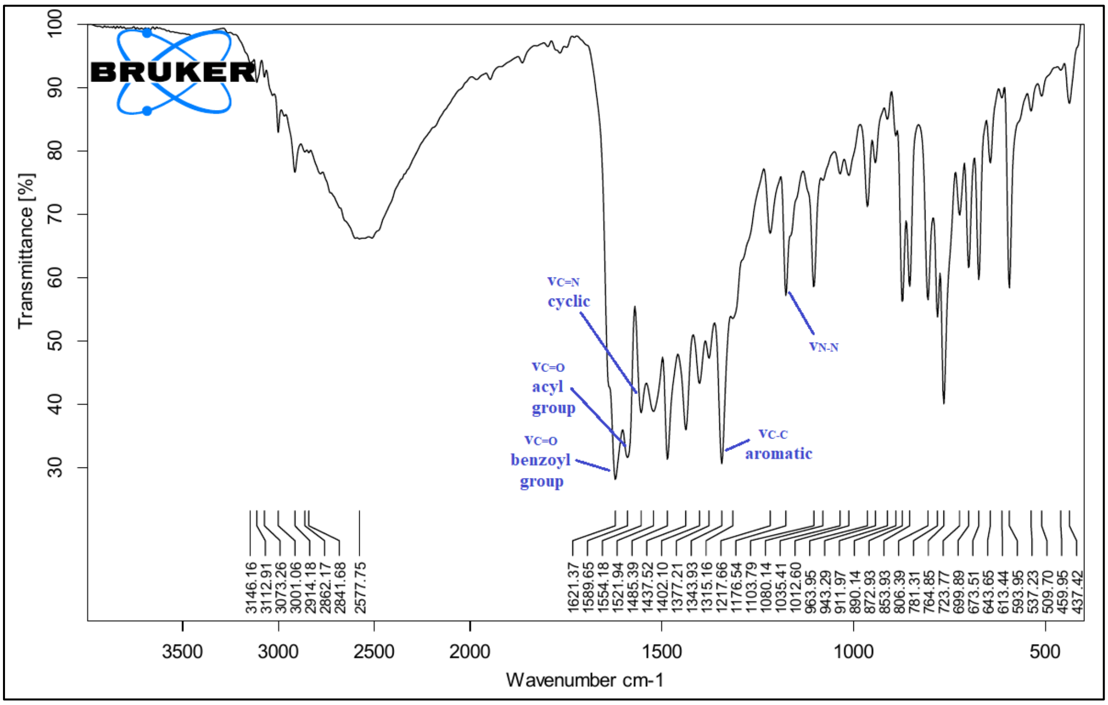

Figure 2a.8 FTIR spectrum of HL^5 ligand.

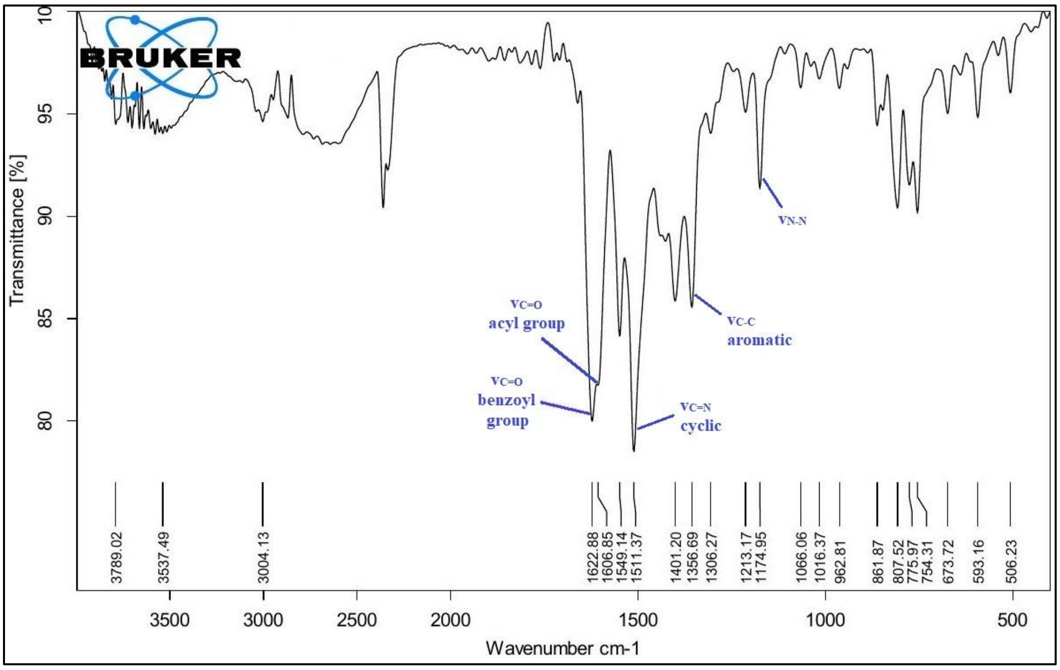

Figure 2a.9 FTIR spectrum of HL^6 ligand.

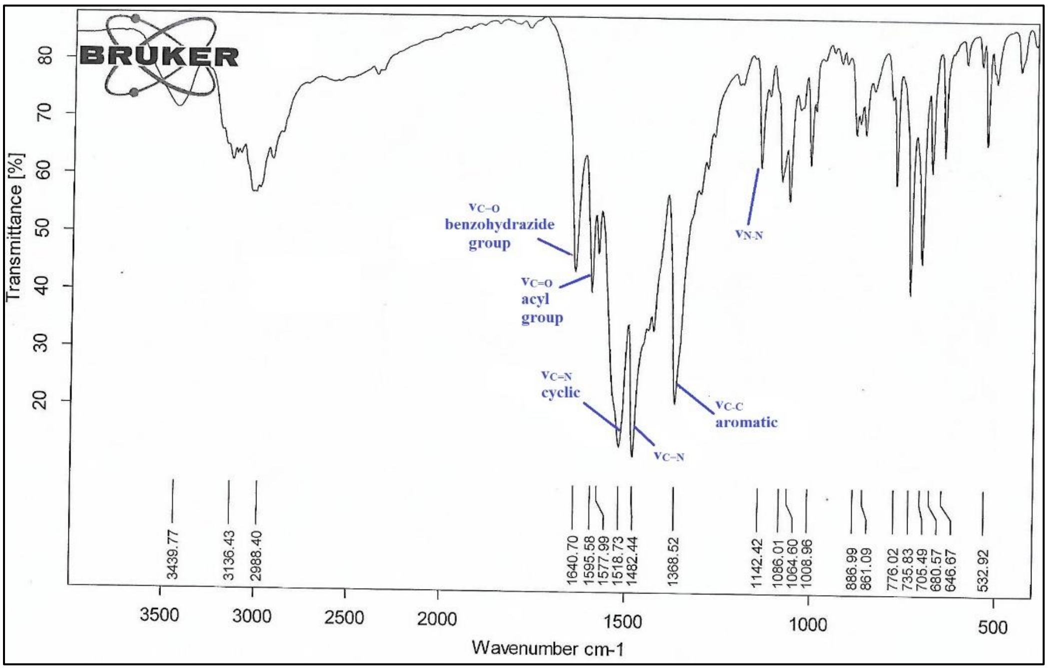

Figure 2a.10 FTIR spectrum of HL^7 ligand.

Table 2a.1 Relative FTIR data values for HL^4, HL^5, HL^6, and HL^7 ligands.

Code	$\upsilon_{C=O}$ benzoyl group	$\upsilon_{C=O}$ benzoic hydrazide	$\upsilon_{C=O}$ acyl group	Cyclic $\upsilon_{C=N}$	υ_{C-C} aromatic	υ_{N-N}	C-H in plane deformation
HL^4	1621	-	1605	1511	1307	1175	1067
HL^5	1621	-	1589	1554	1344	1176	1080
HL^6	1622	-	1607	1511	1356	1175	1066
HL^7	-	1640	1595	1518	1368	1142	1064

2a.3.2 ^{1}H-NMR and ^{13}C-NMR spectroscopic study

The ^{1}H-NMR and ^{13}C-NMR spectra of HL^{4}, HL^{5}, HL^{6}, and HL^{7} ligands were recorded in $CDCl_3$ solvent. In the ^{1}H-NMR spectra of the HL^{4} ligand, a singlet corresponding to the pyrazolone CH_3 group, another singlet for the benzoyl CH_3 group, and multiplets for the aromatic rings were observed at chemical shifts of δ 2.135 ppm, 2.419 ppm, and 7.0-8.0 ppm, respectively. In the ^{13}C-NMR spectra of the HL^{4} ligand, a sharp singlet representing the C=O group appeared at 192.18 ppm. Similarly, in the case of ligand HL^{5}, a singlet at δ 2.127 ppm corresponding to the 6H of the dimethyl-benzoyl CH_3 group, a singlet at δ 2.421 ppm for the 3H of the pyrazolone CH_3 group, and peaks assigned to aromatic protons confirm ligand formation. The ^{13}C-NMR spectrum of HL^{5} confirms the presence of the C=O group (at δ 190.83), pyrazolone CH_3 (at δ 16), dimethyl-benzoyl CH_3 (at δ 21.24), and an enolic form of the ligand due to C-OH (at δ 162.81), as depicted in Figure 2a.14. For ligand HL^{6}, the methyl protons of the 3,5-dimethyl-benzoyl, p-tolyl, and pyrazolone groups exhibit distinct singlet peaks at 2.126, 2.391, and 2.415 ppm, respectively, in the ^{1}H-NMR spectrum. The remaining aromatic protons are observed in the 7.0–7.8 ppm range. The ^{13}C-NMR spectrum and the assignment of peaks for each carbon provide further elucidation of the ligand structure. Notable peaks in the ^{13}C-NMR spectrum include 14.9 ppm for the CH_3 of acylpyrazolone, 21.23 ppm for the CH_3 of the dimethyl-benzoyl group, 21 ppm for the CH_3 of the p-tolyl group, and 190.44 ppm for the C=O group. In the case of ligand HL^{7}, the methyl protons of the 3,5-dimethyl-benzoyl and pyrazolone groups show distinct singlet peaks at δ 2.388 and 1.596 ppm, respectively, in the ^{1}H-NMR spectrum. A singlet for N-H is also observed at δ 15.509 in the ^{1}H-NMR spectrum. The presence of peaks at δ 154.71 ppm for C=N and δ 163.81 ppm for C=O in the ^{13}C-NMR spectrum confirms the binding of benzoic hydrazide with the HL^{5} ligand, indicating the formation of ligand HL^{7}. Figures 2a.11, 2a.13, 2a.15 and 2a.17 depict the ^{1}H-NMR spectra, while Figures 2a.12, 2a.14, 2a.16 and 2a.18 illustrate the ^{13}C-NMR spectra of ligands HL^{4}, HL^{5}, HL^{6}, and HL^{7}, respectively.

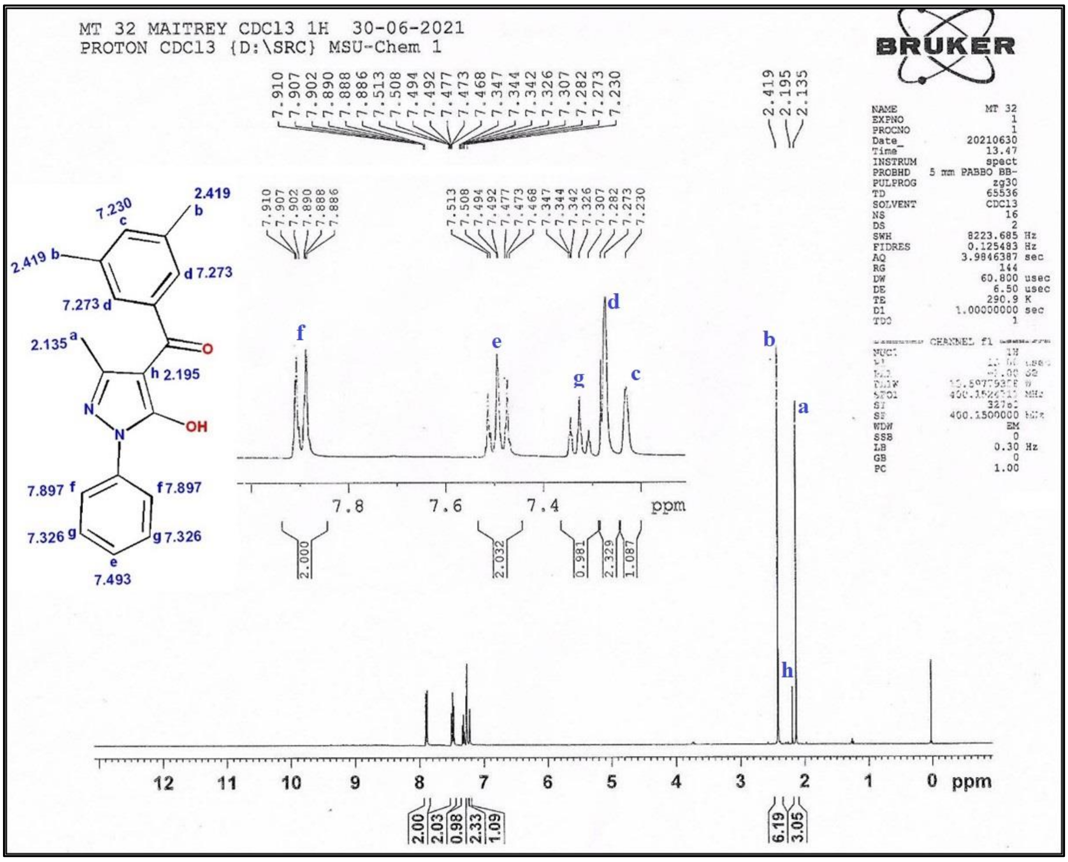

Figure 2a.11 ^{1}H-NMR spectrum of HL^4 ligand.

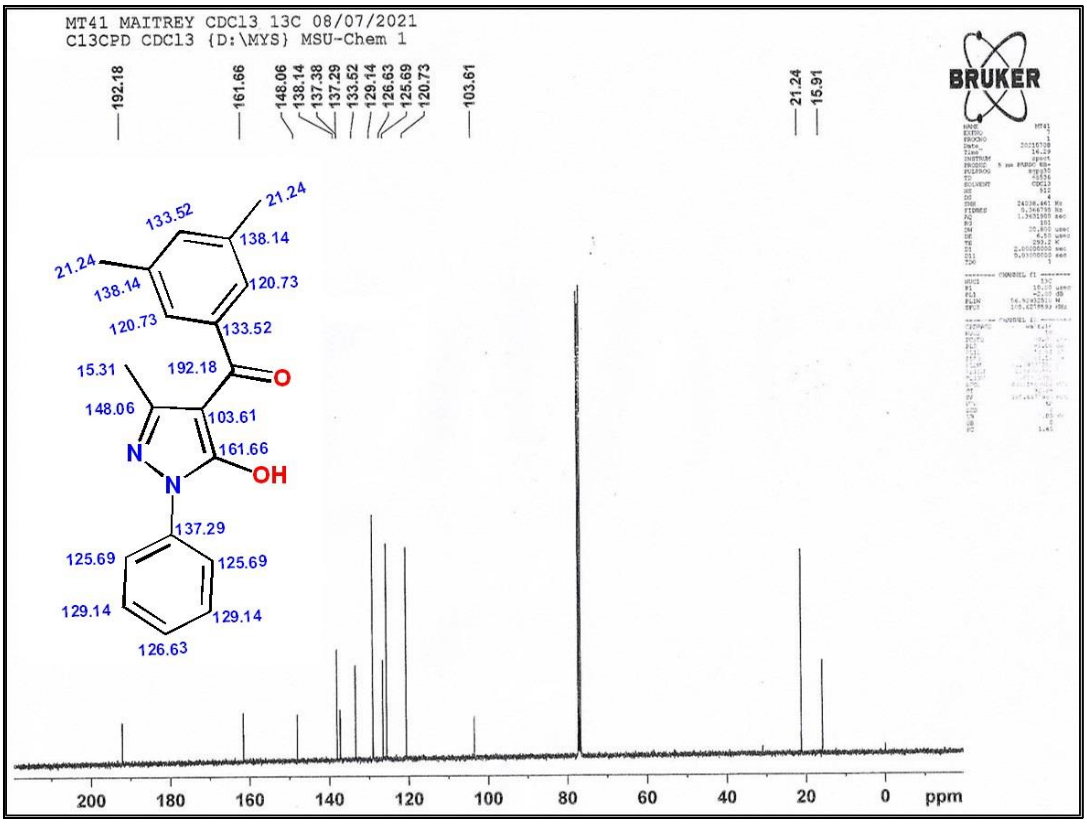

Figure 2a.12 ^{13}C-NMR spectrum of HL^4 ligand.

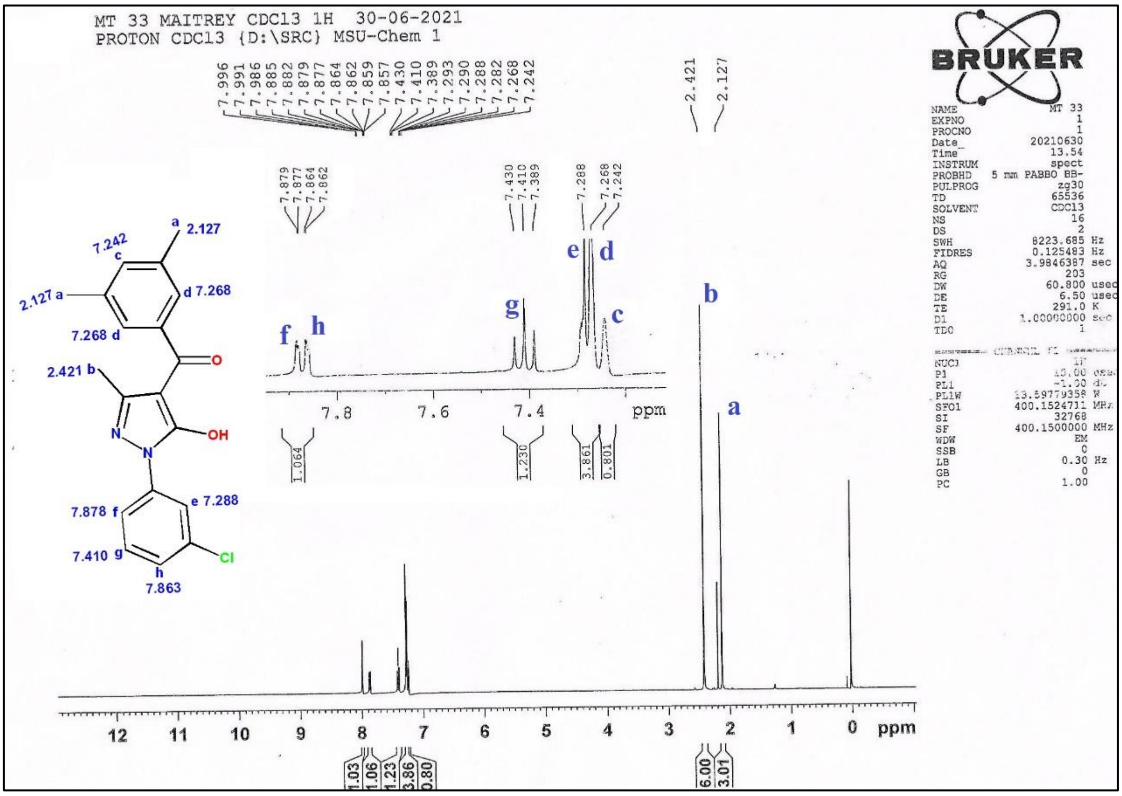

Figure 2a.13 ^{1}H-NMR spectrum of HL^5 ligand.

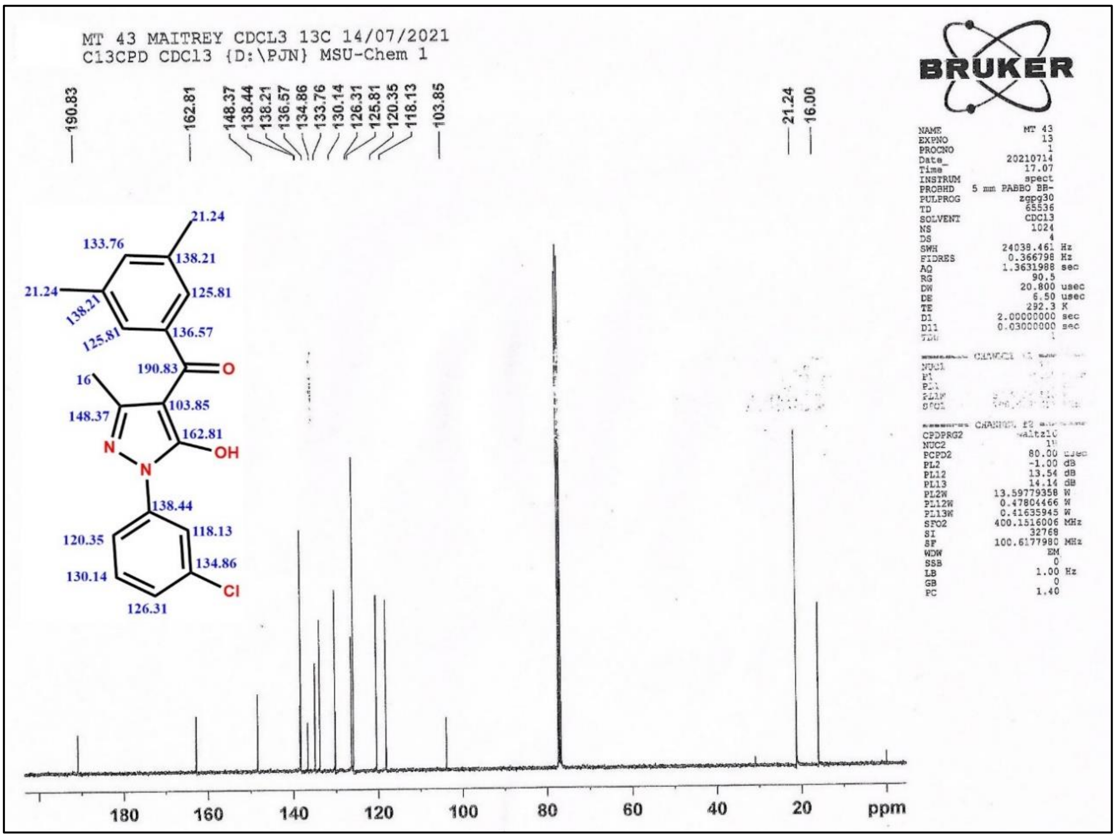

Figure 2a.14 ^{13}C-NMR spectrum of HL^5 ligand.

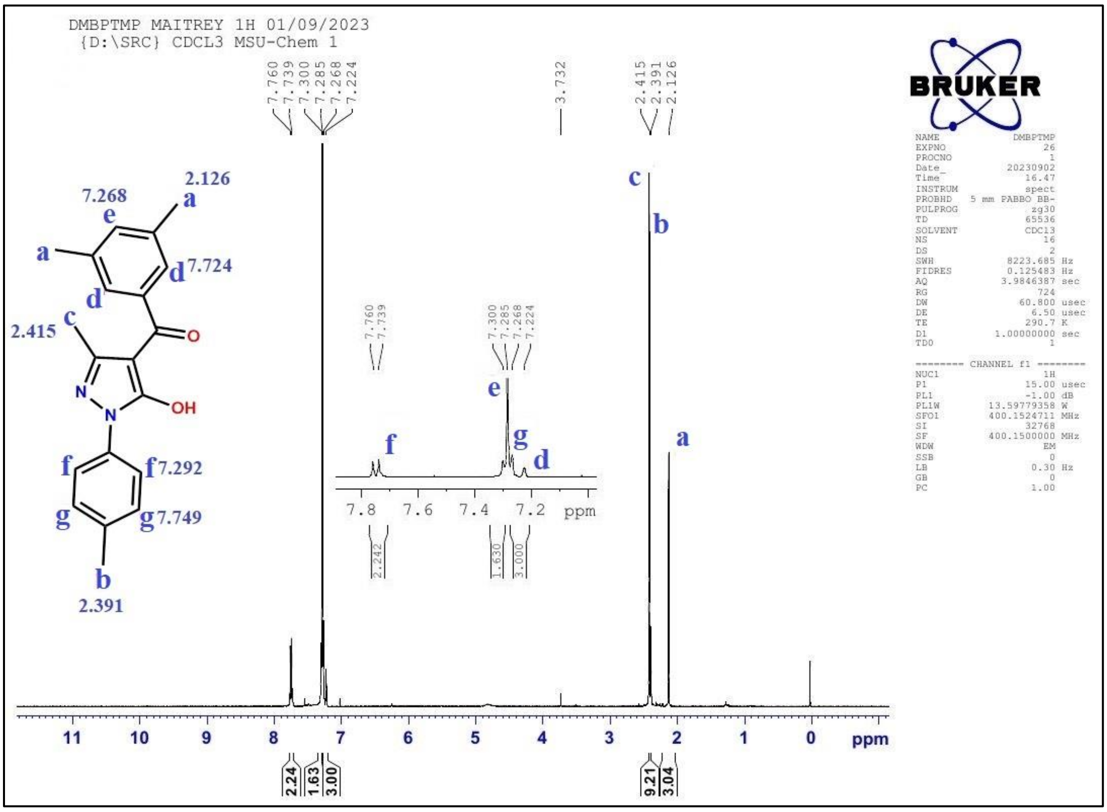

Figure 2a.15 ^{1}H-NMR spectrum of HL^{6} ligand.

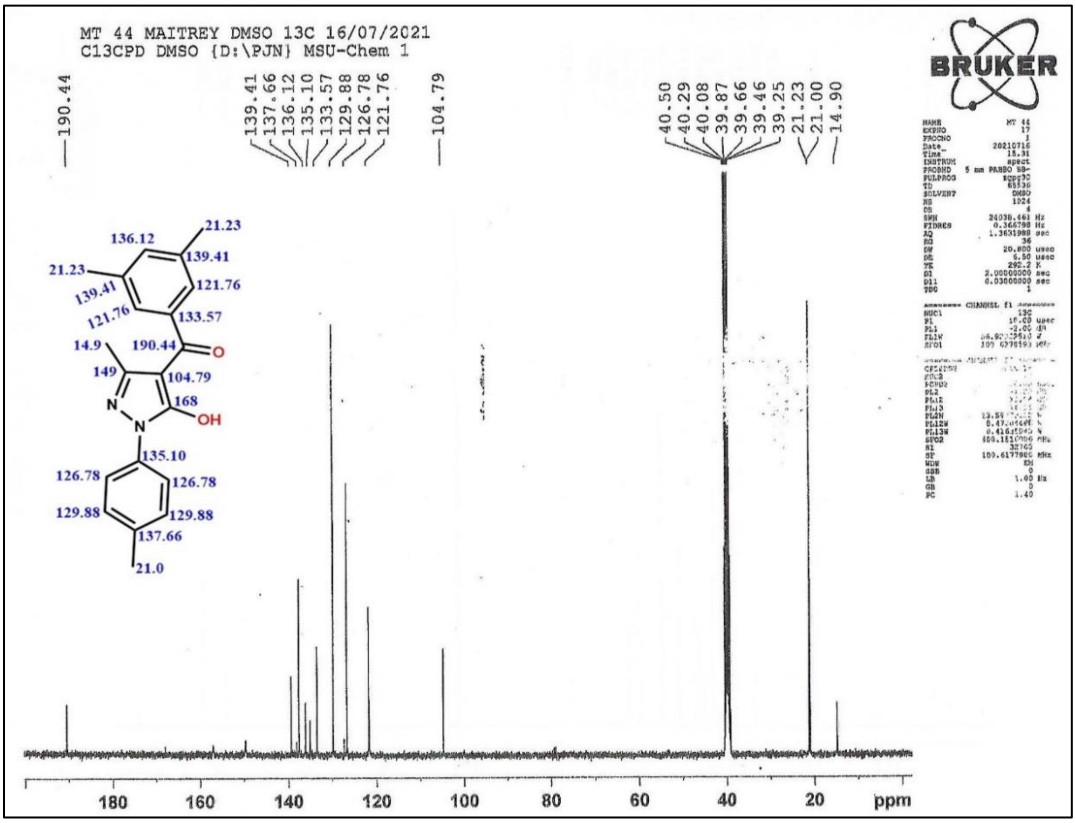

Figure 2a.16 ^{13}C-NMR spectrum of HL^{6} ligand.

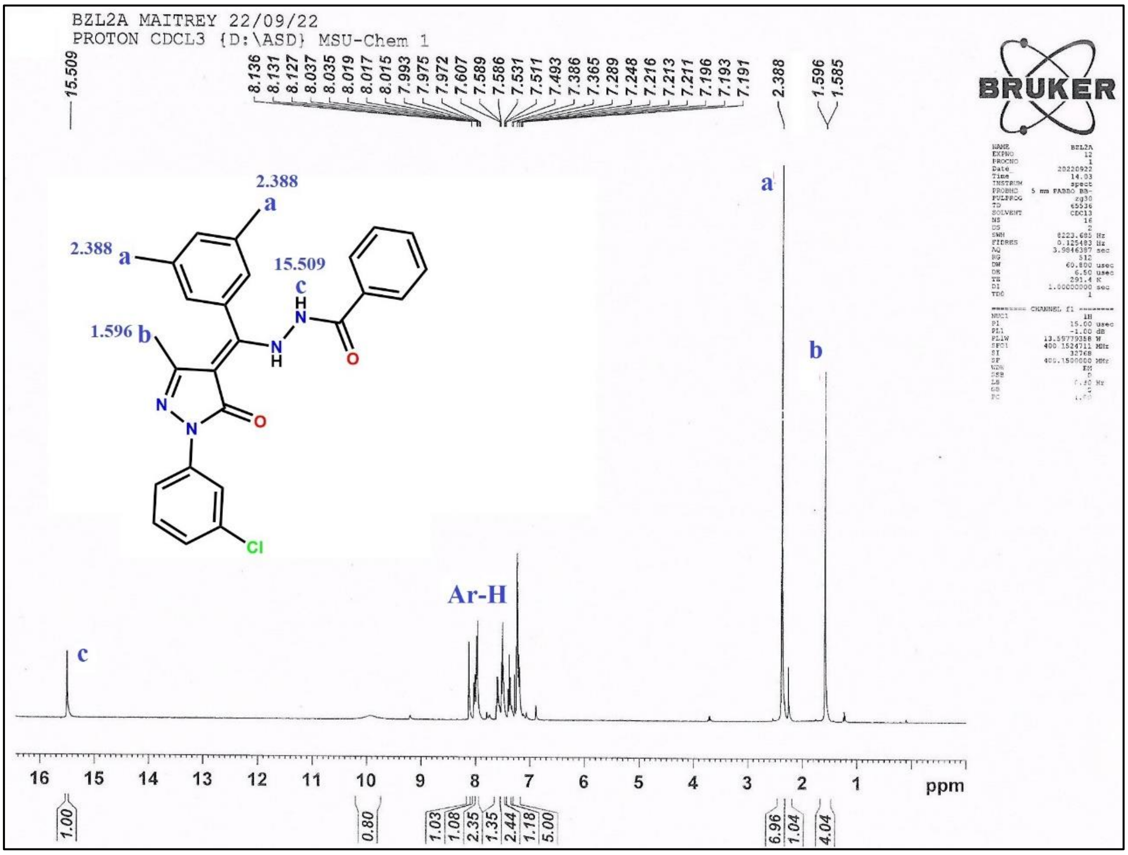

Figure 2a.17 ^{1}H-NMR spectrum of HL^{7} ligand.

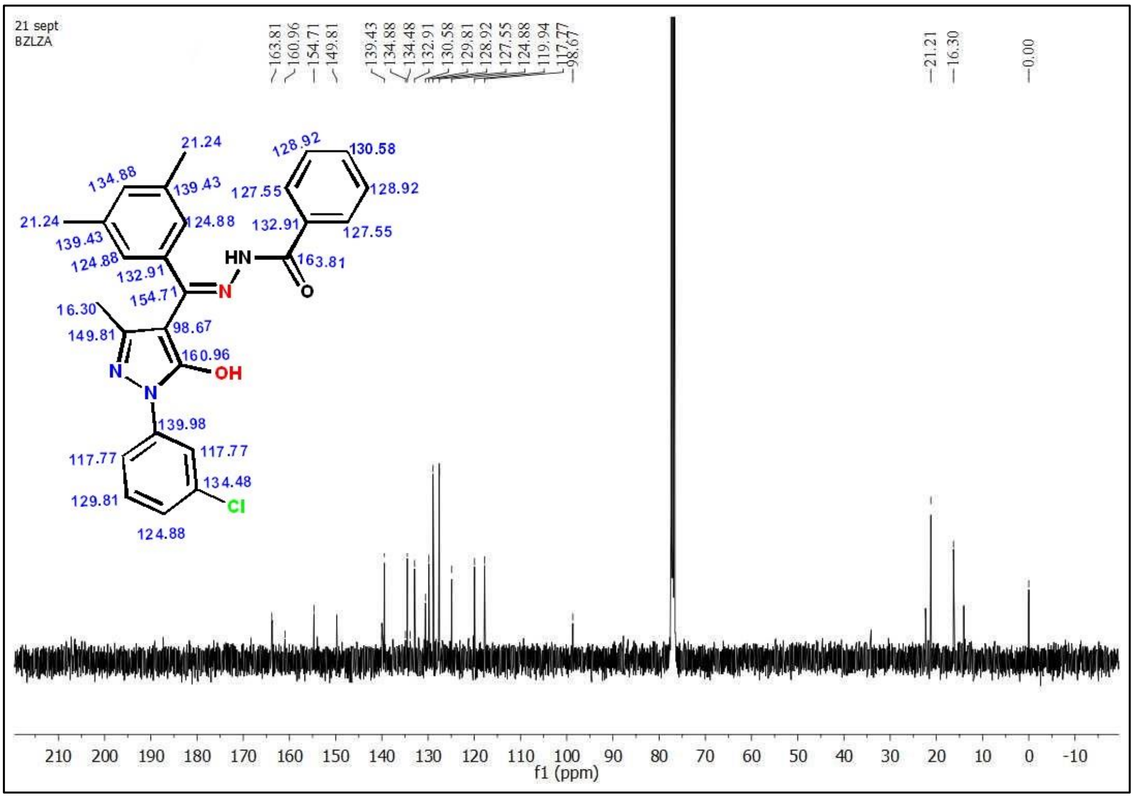

Figure 2a.18 ^{13}C-NMR spectrum of HL^{7} ligand.

2a.3.3 Single crystal X-ray diffraction analysis

Three-dimensional X-ray data and results presented are the of various data aggregation trials. All structural data with refinement parameters for comparison of the HL^4, HL^5, and HL^7 ligands are provided in Table 2a.2.

(i) Crystal Structure of HL^4 ligand

Figure 2a.19 represents a 2D view of a single crystal of HL^4 ligand with atom numbering. The HL^4 ligand transforms into a monoclinic system with a $P\ 2_1/n$ space group, and the crystal was obtained in an enolic tautomeric form. The data of significant bond lengths and bond angles for the HL^4 ligand is provided in Table 2a.3. The ligand has characteristic C=O bond lengths of 1.2999(16) Å for C7-O1 of pyrazolone and 1.2774(16) Å for C11-O2 of 3,5-dimethyl benzoyl group, which are near to bond length of C=O double bond [18,19]. The C7-C8 (1.4181(19) Å) and C8-C9 (1.4402(18) Å) are quite equal to C-C aromatic single bonds. Moreover, the C9-N2 (1.3124(18) Å) bond is also near to the typical C=N bond [11]. There is a presence of an intramolecular hydrogen bond with a 1.78 Å distance between the O-atom of the C=O group of 3,5-dimethyl benzoyl and the H-atom of the OH group pyrazolone, as given in Figure 2a.20. Corresponding H-bonding parameters with symmetry transformations used are provided in Table 2a.4.

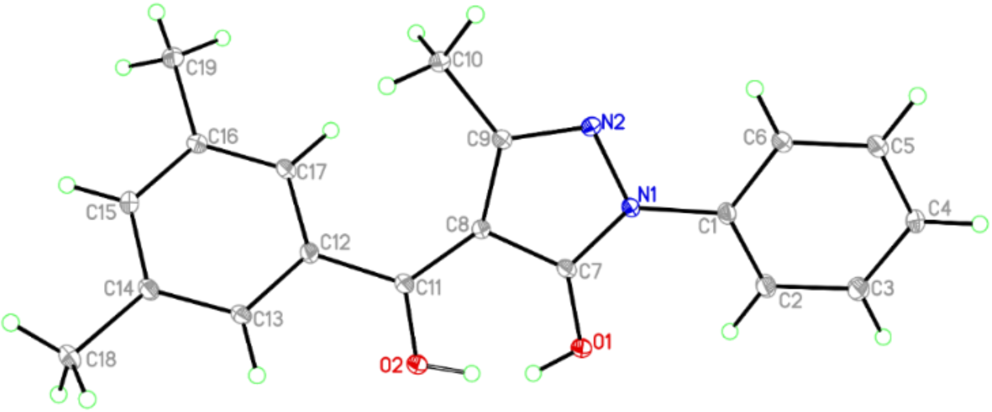

Figure 2a.19 Molecular crystal structure of HL^4 ligand.

Table 2a.2 Structural data of HL^4, HL^5, and HL^7 ligands with refinement parameters.

Code	HL^4 ligand	HL^5 ligand	HL^7 ligand
CCDC number	2171450	2348080	2220753
Empirical formula	$C_{19}H_{18}N_2O_2$	$C_{19}H_{17}ClN_2O_2$	$C_{26}H_{23}ClN_4O_2$
Formula weight	306.35	340.79	458.93
Temperature	105(2) K	100(2) K	100(2) K
Wavelength	0.71073 Å	1.54184 Å	0.71073 Å
Crystal system	Monoclinic	Triclinic	Triclinic
Space group	$P2_1/n$	$P-1$	$P-1$
Unit cell dimensions	a = 11.2993(10) Å, b = 7.2306(4) Å, c = 18.4036(15) Å, α= 90°, β= 91.766(3)°, γ=90°	a = 4.8773(2) Å, b = 12.7284(5) Å, c = 13.2400(3) Å, α= 87.164(3)°, β= 88.856(2)°, γ=81.987(3)°	a = 8.9924(12) Å, b = 11.4798(15) Å, c = 11.8388(13) Å, α= 82.813(4)°, β= 68.566(4)°, γ=84.654(5)°
Volume	1502.9(2) Å^3	812.85(5) Å^3	1127.2(2) Å^3
Z	4	2	2
Density (calculated)	1.354 Mg/m^3	1.392 Mg/m^3	1.352 Mg/m^3
Absorption coefficient	0.089 mm^{-1}	2.193 mm^{-1}	0.201 mm^{-1}
F(000)	648	356	480
Theta range for data collection	2.214 to 33.117°.	3.342 to 78.440°	2.44 to 28.29°
Index ranges	-17<=h<=17, -11<=k<=11, -28<=l<=28	-5<=h<=4, -16<=k<=16, -16<=l<=16	-11<=h<=12, -15<=k<=15, -15<=l<=15
Reflection collected	30890	8554	32558
Independent reflections	5718 [*R(int)* = 0.1095]	3272 [R*(int)* = 0.0412]	5619 [*R(int)* = 0.0743]
Completeness to theta = 25.242°	99.4 %	99.3%	99.9%
Absorption correction	None	Semi-empirical from equivalents	None
Refinement method	Full-matrix least-squares on F^2	Full-matrix least-squares on F^2	Full-matrix least-squares on F^2
Data / restraints / parameters	5718 / 0 / 214	3272 / 0 / 224	5619 / 0 / 309
Goodness-of-fit on F_2	1.033	1.081	1.019
Final R indices [I>2sigma(I)]	R_1 = 0.0625, wR_2 = 0.1499	R_1 = 0.0656, wR_2 = 0.1769	R_1 = 0.0441, wR_2 = 0.1073
R indices (all data)	R_1 = 0.1030, wR_2 = 0.1704	R_1 = 0.0713, wR_2 = 0.1864	R_1 = 0.0569, wR_2 = 0.1155
Largest diff. peak and hole	0.659 and -0.362 e.Å^{-3}	0.628 and -0.410 e.Å^{-3}	0.424 and -0.321 e.Å^{-3}

Table 2a.3 Bond parameters in HL^4 ligand.

Atoms	Bond lengths	Atoms	Bond lengths	Atoms	Bond angles	Atoms	Bond angles
O(1)-C(7)	1.2999(16)	C(5)-C(6)	1.383(2)	C(7)-O(1)-H(1O)	109.5	N(2)-C(9)-C(8)	111.21(12)
O(1)-H(1O)	0.8400	C(7)-C(8)	1.4181(19)	C(11)-O(2)-H(2O)	109.5	N(2)-C(9)-C(10)	117.88(12)
O(2)-C(11)	1.2774(16)	C(8)-C(11)	1.4241(18)	C(7)-N(1)-N(2)	110.41(11)	C(8)-C(9)-C(10)	130.87(12)
O(2)-H(2O)	0.8400	C(8)-C(9)	1.4402(18)	C(7)-N(1)-C(1)	130.43(12)	O(2)-C(11)-C(8)	118.16(12)
N(1)-C(7)	1.3513(17)	C(9)-C(10)	1.4920(19)	N(2)-N(1)-C(1)	119.14(11)	O(2)-C(11)-C(12)	116.75(11)
N(1)-N(2)	1.3963(16)	C(11)-C(12)	1.4816(19)	C(9)-N(2)-N(1)	106.84(11)	C(1)-C(2)-C(3)	119.21(13)
N(1)-C(1)	1.4216(17)	C(12)-C(17)	1.3940(19)	C(2)-C(1)-C(6)	120.07(13)	C(4)-C(3)-C(2)	121.37(14)
N(2)-C(9)	1.3124(18)	C(12)-C(13)	1.4013(18)	C(2)-C(1)-N(1)	121.29(12)	C(3)-C(4)-C(5)	118.85(14)
C(1)-C(2)	1.3872(19)	C(13)-C(14)	1.388(2)	C(6)-C(1)-N(1)	118.64(12)	C(6)-C(5)-C(4)	120.76(13)
C(1)-C(6)	1.3952(19)	C(14)-C(15)	1.396(2)	O(1)-C(7)-N(1)	125.52(12)	C(5)-C(6)-C(1)	119.74(13)
C(2)-C(3)	1.388(2)	C(14)-C(18)	1.5080(19)	O(1)-C(7)-C(8)	126.67(12)	C(7)-C(8)-C(9)	103.71(11)
C(3)-C(4)	1.384(2)	C(15)-C(16)	1.3960(19)	N(1)-C(7)-C(8)	107.81(11)	C(11)-C(8)-C(9)	138.30(13)
C(4)-C(5)	1.388(2)	C(16)-C(17)	1.388(2)	C(7)-C(8)-C(11)	117.72(12)	C(8)-C(11)-C(12)	125.09(12)

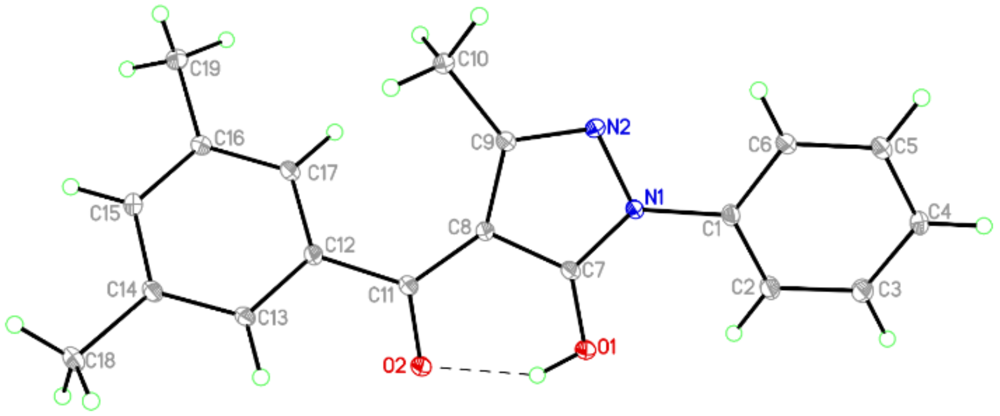

Figure 2a.20 Intramolecular hydrogen bonding in HL^4 ligand drawn at 50 % probability level.

Table 2a.4 Hydrogen bond parameters of HL^4 ligand.

D-H...A	d(D-H)	d(H...A)	d(D...A)	<(DHA)
O(1)-H(1O^a)...O(2)	0.84	1.78	2.4948(14)	142.3

Symmetry transformations used to generate equivalent atoms: #1 -x+3/2, y+1/2, -z+3/2

(ii) Crystal Structure of HL^5 ligand

Figure 2a.21 represents a 2D view of a single crystal of HL^5 ligand with atom numbering. The HL^5 ligand transforms into a triclinic system with a *P −1* space group, and the crystal was obtained in an enolic tautomeric form. The data of significant bond lengths and bond angles for HL^5 ligand is provided in Table 2a.5. The ligand has characteristic C=O bond lengths of 1.249(2) Å for C1-O1 of pyrazolone and 1.324(2)

Å for C11-O2 of 3,5-dimethyl benzoyl group, which are near to bond length of C=O double bond [18,19]. Compared to the HL^4 ligand, a shorter bond length is observed for the pyrazolone C=O bond, while a longer bond length is noted for the benzoyl C=O bond in HL^5. An intramolecular hydrogen bonding at 1.88 Å between the O atom of the pyrazolone ring and the H atom of the OH group of the 3,5-dimethyl-benzoyl ring is observed here as well (See Figure 2a.21). Corresponding H-bonding parameters with symmetry transformations used are provided in Table 2a.6.

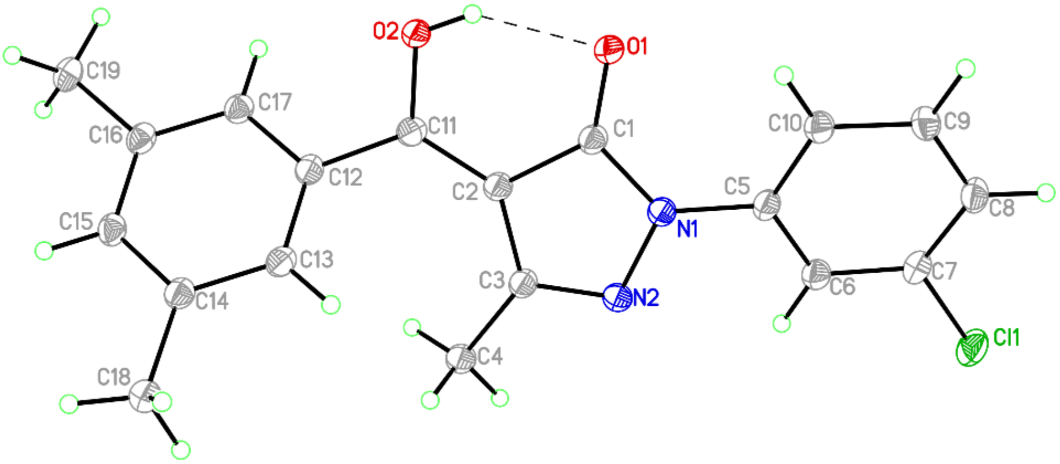

Figure 2a.21 Molecular crystal structure of HL^5 ligand drawn at 50 % probability level.

Table 2a.5 Bond parameters in HL^5 ligand.

Atoms	Bond lengths	Atoms	Bond lengths	Atoms	Bond angles	Atoms	Bond angles
Cl(1)-C(7)	1.746(2)	C(6)-C(7)	1.384(3)	C(1)-N(1)-N(2)	111.95(15)	C(10)-C(5)-C(6)	120.88(18)
O(1)-C(1)	1.249(2)	C(7)-C(8)	1.382(3)	C(1)-N(1)-C(5)	129.00(16)	C(10)-C(5)-N(1)	120.82(17)
O(2)-C(11)	1.324(2)	C(8)-C(9)	1.389(3)	N(2)-N(1)-C(5)	118.60(15)	C(6)-C(5)-N(1)	118.30(17)
O(2)-H(2O)	0.80(3)	C(9)-C(10)	1.397(3)	C(3)-N(2)-N(1)	106.85(15)	C(7)-C(6)-C(5)	118.26(18)
N(1)-C(1)	1.367(2)	C(11)-C(12)	1.472(3)	O(1)-C(1)-N(1)	127.34(18)	C(8)-C(7)-C(6)	122.68(19)
N(1)-N(2)	1.409(2)	C(12)-C(13)	1.391(3)	O(1)-C(1)-C(2)	127.61(17)	C(8)-C(7)-Cl(1)	119.34(16)
N(1)-C(5)	1.412(2)	C(12)-C(17)	1.406(3)	N(1)-C(1)-C(2)	105.04(15)	C(6)-C(7)-Cl(1)	117.97(16)
N(2)-C(3)	1.310(3)	C(13)-C(14)	1.396(3)	C(11)-C(2)-C(3)	135.92(17)	C(7)-C(8)-C(9)	117.95(18)
C(1)-C(2)	1.452(2)	C(14)-C(15)	1.391(3)	C(11)-C(2)-C(1)	119.00(16)	O(2)-C(11)-C(2)	119.69(17)
C(2)-C(11)	1.382(3)	C(14)-C(18)	1.508(3)	C(3)-C(2)-C(1)	104.95(16)	O(2)-C(11)-C(12)	113.44(16)
C(2)-C(3)	1.448(2)	C(15)-C(16)	1.396(3)	N(2)-C(3)-C(2)	111.04(16)	C(2)-C(11)-C(12)	126.80(17)
C(5)-C(10)	1.394(3)	C(16)-C(17)	1.391(3)	N(2)-C(3)-C(4)	118.60(17)	C(13)-C(12)-C(17)	120.36(17)
C(5)-C(6)	1.396(3)	C(16)-C(19)	1.511(3)	C(2)-C(3)-C(4)	130.25(17)	C(13)-C(12)-C(11)	120.20(17)

Table 2a.6 Hydrogen bond parameters of HL^5 ligand.

D-H...A	d(D-H)	d(H...A)	d(D...A)	<(DHA)
O(1)-H(1O^a)...O(2)	0.84	1.78	2.4948(14)	142.3

Symmetry transformations used to generate equivalent atoms: #1 -x+3/2, y+1/2, -z+3/2

(iii) Crystal Structure of HL^7 ligand

The colourless plate-type crystals of ligand HL^7 crystallized in the keto form, featuring a triclinic system and $P-1$ space group, as shown in Figure 2a.22 and detailed in Table 2a.2. The data of significant bond lengths and bond angles for HL^5 ligand is provided in Table 2a.7. The ligand has characteristic C=O bond lengths of 1.2586(17) Å for C1-O1 of pyrazolone and 1.2359(17) Å for C20-O2 of benzo hydrazone group. The 2D view of Figure 2a.22 illustrates the presence of intramolecular hydrogen bonding between the H atom of the N4 atom and the O1 atom. Further evidence of intermolecular N(3)-H(3N)···O(2)#1 and intramolecular C(6)-H(6A)···O(1) hydrogen bonding is provided in Table 2a.8.

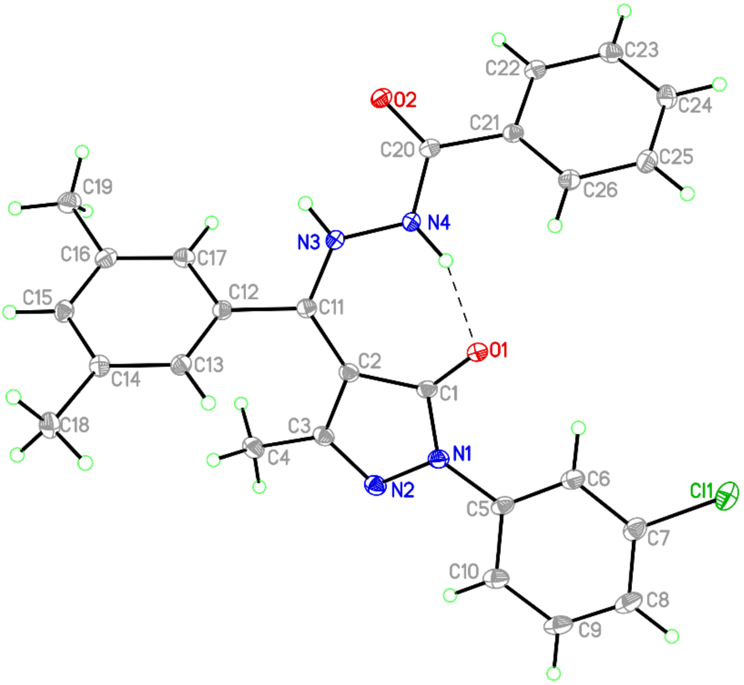

Figure 2a.22 Molecular crystal structure of HL^7 ligand drawn at 50 % probability level.

Table 2a.7 Bond parameters in HL^7 ligand.

Atoms	Bond lengths	Atoms	Bond lengths	Atoms	Bond angles	Atoms	Bond angles
Cl(1)-C(7)	1.7434(18)	N(3)-N(4)	1.3790(16)	C(1)-N(1)-N(2)	112.46(11)	O(1)-C(1)-N(1)	124.32(13)
O(1)-C(1)	1.2586(17)	N(3)-H(3N)	0.88(2)	C(3)-N(2)-N(1)	106.20(11)	O(1)-C(1)-C(2)	130.82(13)
O(2)-C(20)	1.2359(17)	N(4)-C(20)	1.3458(18)	C(11)-N(3)-N(4)	123.65(12)	N(1)-C(1)-C(2)	104.76(12)
N(1)-C(1)	1.3745(18)	N(4)-H(4N)	0.92(2)	C(11)-N(3)-H(3N)	119.8(13)	C(11)-C(2)-C(1)	127.54(13)
N(1)-N(2)	1.3985(17)	C(1)-C(2)	1.440(2)	N(4)-N(3)-H(3N)	116.4(13)	C(11)-C(2)-C(3)	127.47(13)
N(1)-C(5)	1.4126(18)	C(2)-C(11)	1.4081(19)	C(20)-N(4)-N(3)	118.23(12)	N(3)-C(11)-C(2)	125.50(13)
N(2)-C(3)	1.3076(19)	C(2)-C(3)	1.4456(19)	C(20)-N(4)-H(4N)	124.9(14)	N(3)-C(11)-C(12)	112.88(12)
N(3)-C(11)	1.3250(18)	C(11)-C(12)	1.4803(19)	N(3)-N(4)-H(4N)	116.0(14)	O(2)-C(20)-N(4)	122.18(13)
C(3)-C(4)	1.494(2)	N(4)-H(4N)	0.92(2)	O(2)-C(20)-C(21)	123.18(12)	N(4)-C(20)-C(21)	114.63(12)

Table 2a.8 Hydrogen bond parameters of HL^7 ligand.

D-H...A	d(D-H)	d(H...A)	d(D...A)	<(DHA)
N(3)-H(3N)...O(2)#1	0.88(2)	1.99(2)	2.8408(16)	162.4(18)
N(4)-H(4N)...O(1)	0.92(2)	1.71(2)	2.5783(15)	158(2)
C(6)-H(6A)...O(1)	0.95	2.23	2.8581(17)	122.7

Symmetry transformations used to generate equivalent atoms: #1 -x,-y+1,-z+2

2a.3.4 DFT computational analysis

The synthetic ligands HL^4, HL^5, and HL^7 underwent DFT computational analysis to explore and correlate their chemical and physical characteristics. This analysis examined the theoretically optimized geometry (see Figure 2a.23), frontier orbitals, bond parameters, and vibrations [15,20–22]. The structures of HL^4, HL^5, and HL^7 ligands were optimized, yielding electronic energy values of −27.063, −39.57, and −49.90 keV, respectively. The more negative electronic energy of the HL^7 ligand implies its greater stability.

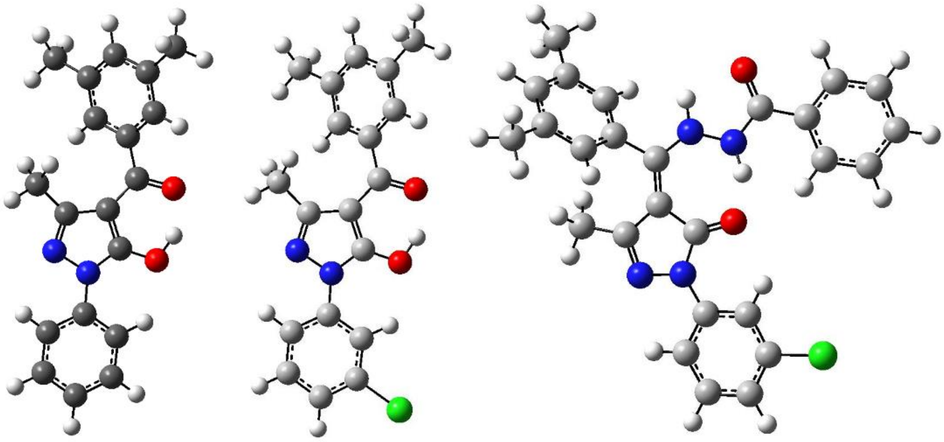
HL^4 ligand HL^5 ligand HL^7 ligand

Figure 2a.23 DFT optimized geometries for HL^4, HL^5 and HL^7 ligands.

Figure 2a.24 illustrates the regions covered by HOMOs and LUMOs for all ligands. It displays the energies of the HOMO, HOMO−1, and HOMO−2 with energies of −6.17, −6.48, −6.73 eV for HL^4, −6.46, −6.66, −6.83 eV for HL^5, and −5.76, −6.15, −6.66 eV for HL^7, respectively. Also, LUMO, LUMO+1, and LUMO+2, with the energy of −1.83, −0.55, −0.16 eV for HL^4 and −1.98, −0.87, −0.39 eV for HL^5, and −2.16, −1.198, −0.64 eV for HL^7, respectively. The values of $\Delta E_{HOMO-LUMO}$, $\Delta E_{HOMO-1-LUMO-1}$, and $\Delta E_{HOMO-2-LUMO-2}$ are 4.439, 5.933, 6.577 eV for HL^4, 4.48, 5.79, 6.44 eV for HL^5, and 3.6, 4.952, 6.02 eV for HL^7, respectively, which can be used to describe chemical stability (as depicted in Figure 2a.25). The diamagnetic behaviour of the ligands is elucidated by the presence of paired electrons in all HOMOs. The ΔE values are higher for bidentate acylpyrazolone ligands (HL^4 and HL^5) compared to their Schiff base ligand (HL^7). Global parameters provided in Table 2a.9 offer a comprehensive understanding of the characteristics of the complexes.

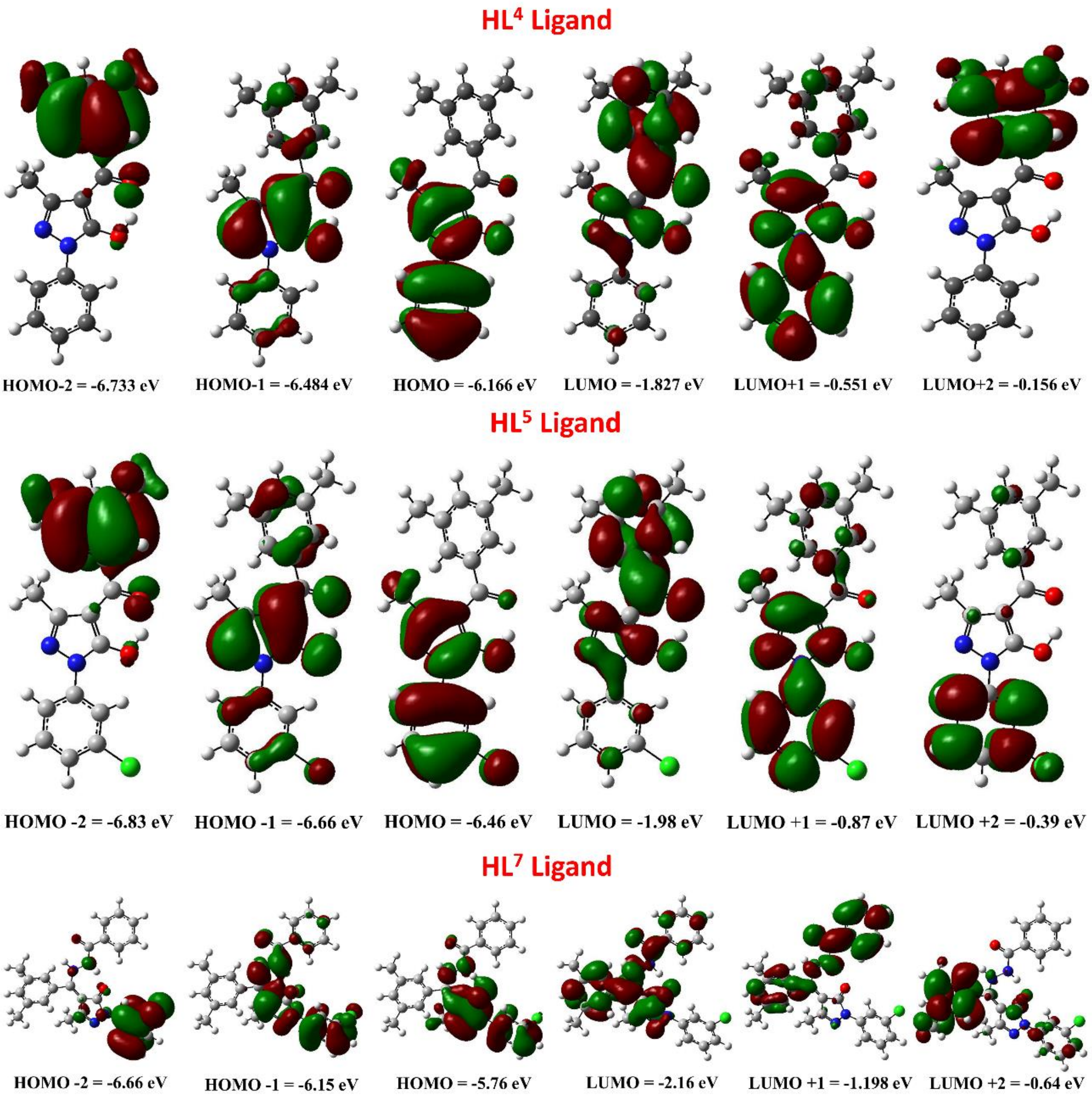

Figure 2a.24 HOMO-LUMO orbitals for HL^4, HL^5 and HL^7 ligands.

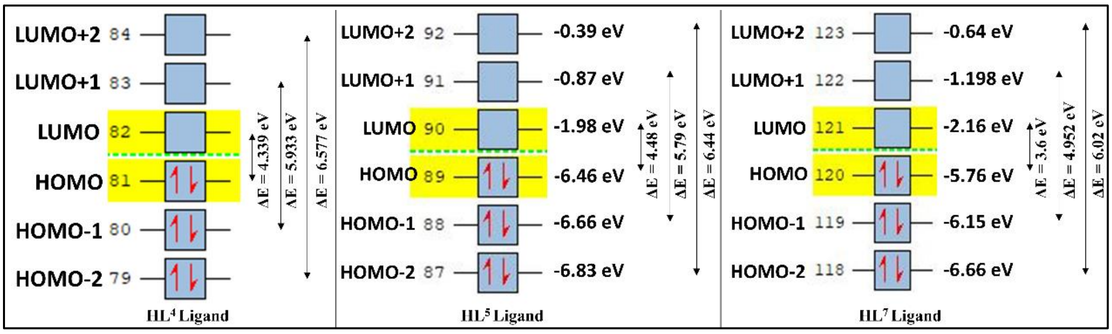

Figure 2a.25 HOMO-LUMO energy values for HL^4, HL^5 and HL^7 ligands.

Table 2a.9 Global parameters for HL^4, HL^5 and HL^7 ligands.

Parameters	**Mathematical Formula**	**HL^4 Ligand**	**HL^5 Ligand**	**HL^7 Ligand**
E_{LUMO}	E_{LUMO}	−6.166	−1.98	−2.16
E_{HOMO}	E_{HOMO}	−1.827	−6.46	−5.76
ΔE	$\Delta E = E_{LUMO} - E_{HOMO}$	4.339	4.48	3.6
Electron affinity (EA)	$EA = -E_{LUMO}$	6.166	1.98	2.16
Ionization potential (IP)	$IP = -E_{HOMO}$	−3.9965	6.46	5.76
Chemical Potential (μ)	$\mu = \frac{1}{2}(E_{Homo} + E_{Lumo})$	1.827	−4.22	−3.96
Global Hardness (η)	$\eta = -\frac{1}{2}(E_{Homo} - E_{Lumo})$	3.9965	2.24	1.8
Softness (S)	$S = 1/2\eta$	2.1695	0.223	0.278
Electronegativity (EN)	$EN = -\frac{1}{2}(E_{Homo} + E_{Lumo})$	0.230	4.22	3.96
Electrophilicity index (ω)	$\omega = \mu^2/2\eta$	3.674	3.97	4.36

The points outlined in the section on FTIR spectroscopic analysis hold paramount significance when the theoretical values closely align with those observed in the experimental spectra. A robust correlation and early indication of discrepancies between asymmetric and symmetric vibrations are evident when comparing theoretical and experimental vibrations. Table 2a.10 presents the essential theoretical vibrations alongside actual FTIR spectrum values, while Figures 2a.26-2a.28 showcase the DFT-optimized IR spectra.

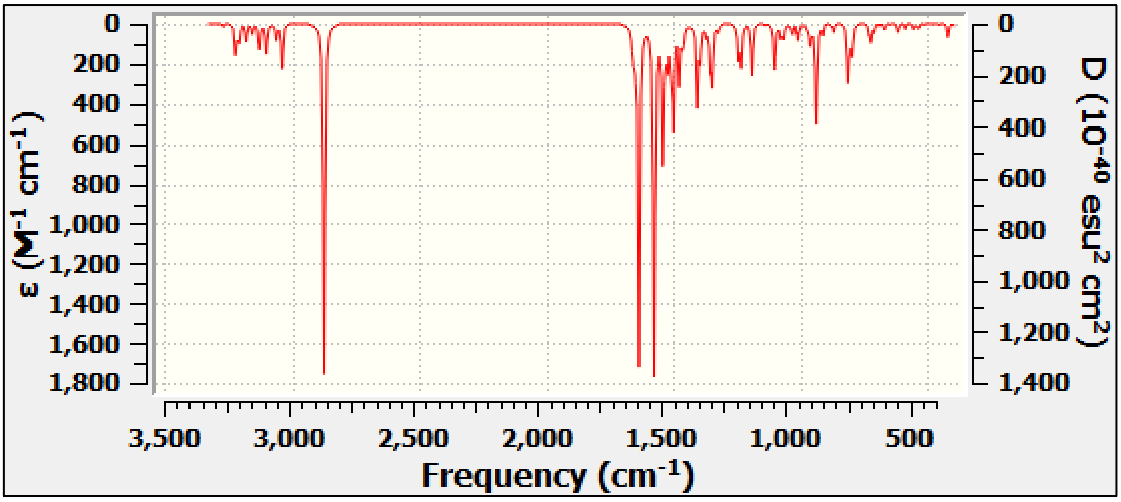

Figure 2a.26 FTIR spectra of HL^4 ligand through computational analysis.

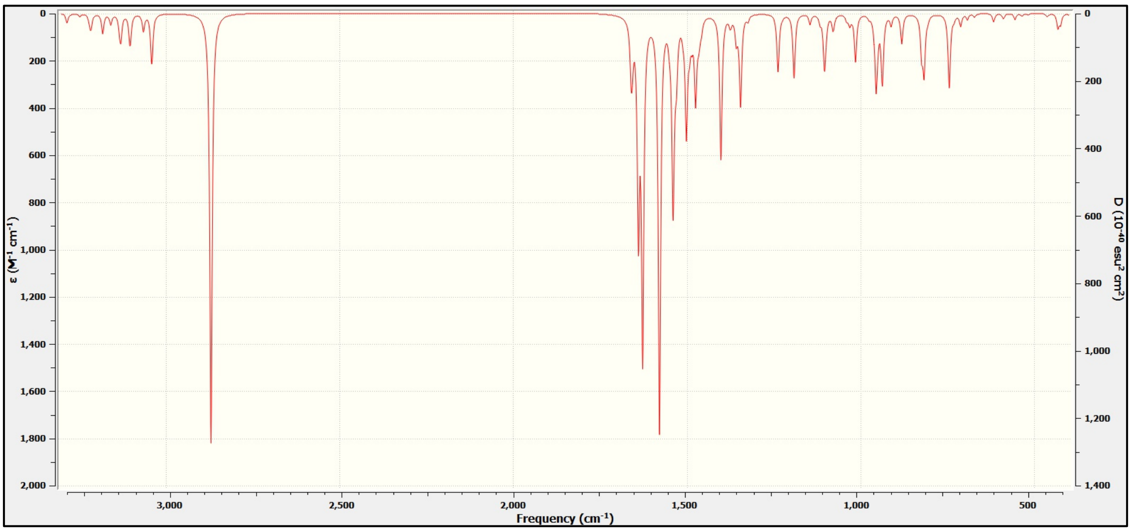

Figure 2a.27 FTIR spectra of HL^5 ligand through computational analysis.

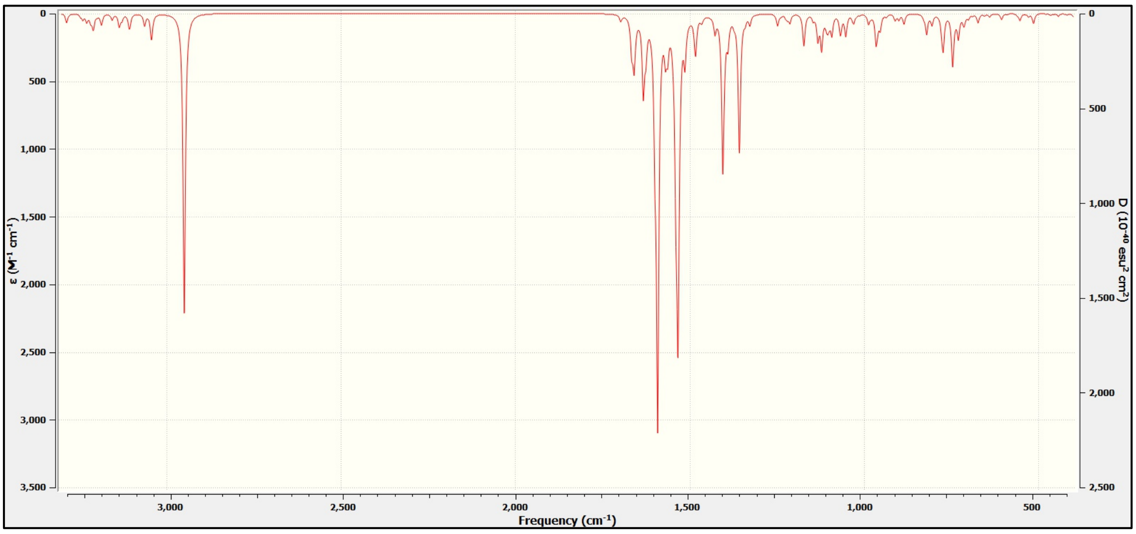

Figure 2a.28 FTIR spectra of HL^7 ligand through computational analysis.

Table 2a.10 DFT optimized vibrational frequency comparison with experimental values for HL^4, HL^5 and HL^7 Ligands.

Vibrations (in cm^{-1})	**HL^4 ligand**		**HL^5 ligand**		**HL^7 Ligand**	
	Experimental	Theoretical	Experimental	Theoretical	Experimental	Theoretical
$\nu_{(C=O)}{}^{A}$	1621	-	1621	1639	1595	1697
$\nu_{(C=O)}{}^{B}$	1605	1595	1589	1627	1595	1591
$\nu_{(C=O)}{}^{C}$	-	-	-	-	1640	1665
$\nu_{(C=N)}$	1511	1527	1485	1502	1482	1513
cyclic $\nu_{(C=N)}$	1576	1579	1554	1578	1518	1568

^{A}dimethyl-benzoyl, ^{B}acyl-pyz, ^{C}BZ-group

2a.3.5 Hirshfeld surface area analysis

Hirshfeld Surface (HS) analysis was a novel approach to uncover intermolecular interactions within the crystal lattice. As an initial step of the HS analysis, energy calculations were performed for a 3.8 Å cluster surrounding the selected HS of ligands HL^4, HL^5, and HL^7 to ascertain precise energy parameters and crystal strength. The interaction energy data were computed using the rapid [HF/3-21G] model of Crystal Explorer 17.5 software [23,24]. Figures 2a.29 depict the computed fragments for a 3.8 Å cluster around the selected HS fragment of HL^4, HL^5, and HL^7 ligands, each represented by different coloured fragments, respectively.

The interaction energies (in kJ mol^{-1}) of ligands HL^4, HL^5, and HL^7 with neighbouring molecules are detailed in Tables 2a.11-2a.13, respectively. Molecules sharing similar colours represent pairs of molecules, with the number of molecules in each pair denoted by N. Symop denotes the rotational operators between the pair and the centre molecule, while R signifies the distance (in Å) between the centroids. The interaction energies (in kJ mol^{-1}) of a selected molecule with neighbouring molecules are presented with four essential components: the electrostatic component (E_{ele}), polarization component (E_{pol}), dispersion component (E_{dis}), and repulsion component (E_{rep}). Lattice energy calculation provides insight into the bond strength within the ligands, and it was calculated using the following formula.

$$E_{Lat.}^{\frac{HF}{321}-G} = 0.5\,(N \times Eto)$$

The energy framework diagrams, illustrating Coulomb energy, Dispersion energy, Total energy, and Total energy (annotated) for ligands HL^4, HL^5, and HL^7, with a tube size of 80 and a 5 kJ mol^{-1} cut-off (Threshold) energy, are presented in Figures

2a.30-2a.32, respectively. The diagrams feature cylinder-like tubes connecting nearby molecules, visually representing their interactions. Red, green, and blue cylinders represent Coulomb, Dispersion, and Total energy. These energy framework diagrams visually illustrate the anisotropy of the molecular and interatomic interaction topology. The cylinders are connected between the centroids of molecules.

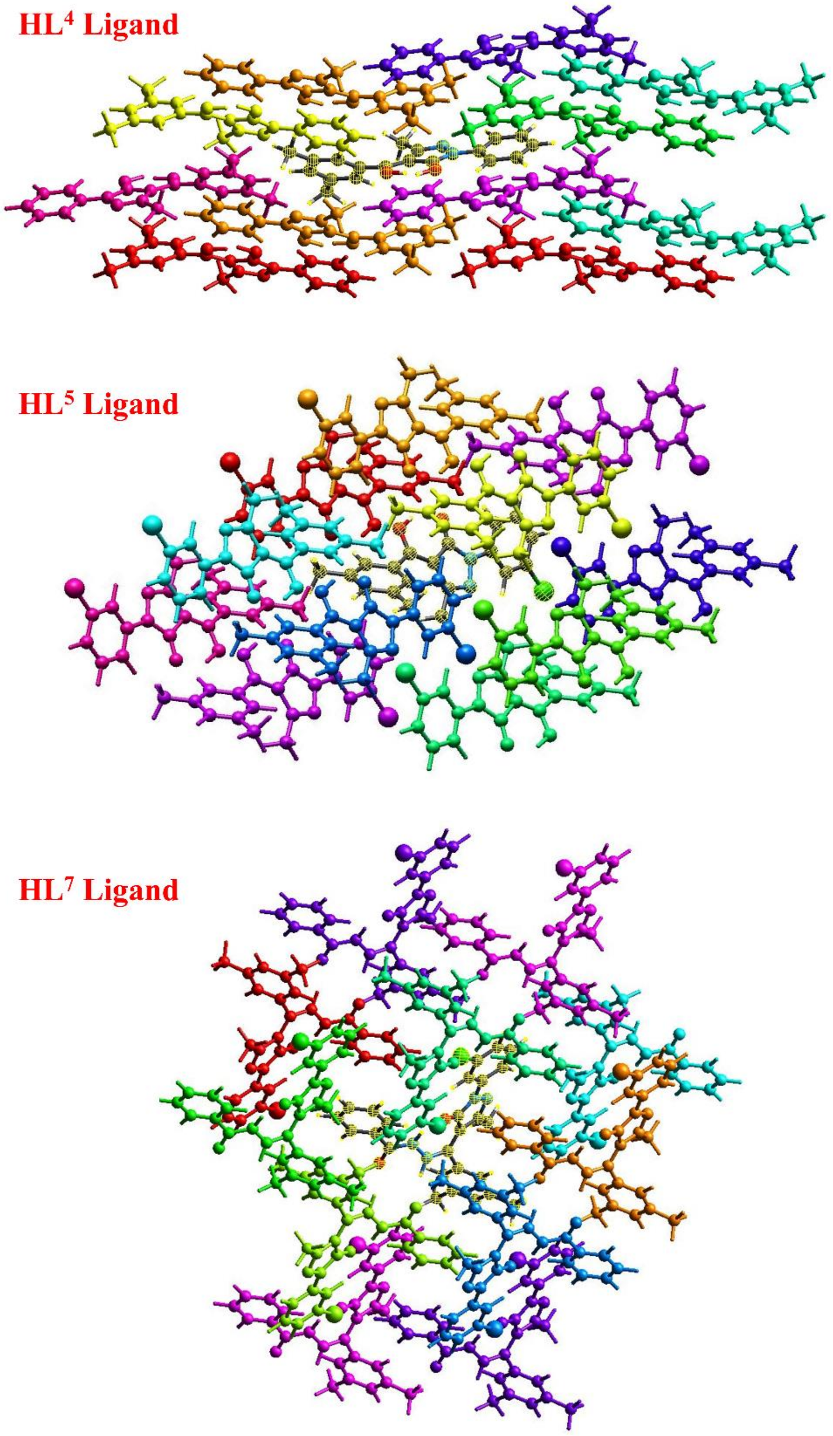

Figure 2a.29 The calculated fragments for a 3.8 Å cluster around the selected HS fragment of HL^4, HL^5, and HL^7 ligands.

Table 2a.11 The interaction energies (in kJ mol^{-1}) of HL^4 Ligand molecule with neighbouring molecules.

	N	Symop	R	Electron density	E_{ele}	E_{pol}	E_{dis}	E_{rep}	E_{total}	Lattice energy
🟥	2	x+1/2, -y+1/2, z+1/2	12.14	HF/3-21G	-0.6	-0.2	-7.4	2.2	-5.7	-5.7
🟧	2	-x+1/2, y+1/2, -z+1/2	5.52	HF/3-21G	-18.9	-6.4	-97	45.6	-73.8	-73.8
🟨	2	x+1/2, -y+1/2, z+1/2	10.83	HF/3-21G	-3	-1	-19.4	9.8	-13.2	-13.2
🟩	1	-x, -y, -z	6.97	HF/3-21G	-5.4	-3.6	-45.3	22.3	-30.6	-15.3
🟩	2	x+1/2, -y+1/2, z+1/2	11.12	HF/3-21G	-3.6	-1.3	-24	12	-16.4	-16.4
🟦	2	-x+1/2, y+1/2, -z+1/2	14.86	HF/3-21G	-0.9	-0.5	-7.7	2.2	-6.4	-6.4
🟦	2	-x+1/2, y+1/2, -z+1/2	11.69	HF/3-21G	0	0	-1.8	0	-1.7	-1.7
🟦	1	-x, -y, -z	14.26	HF/3-21G	-0.4	-0.4	-15.7	8.4	-8	-4
🟪	1	-x, -y, -z	8.80	HF/3-21G	-1.3	-0.5	-15.4	5	-11.4	-5.7
🟪	1	-x, -y, -z	8.74	HF/3-21G	0.1	-6.3	-27.3	16.5	-15.3	-7.65
🟪	1	-x, -y, -z	14.77	HF/3-21G	0	0	-2.1	0.1	-1.8	-0.9

Table 2a.12 The interaction energies (in kJ mol^{-1}) of HL^5 Ligand molecule with neighbouring molecules.

	N	Symop	R	Electron Density	E_{ele}	E_{pol}	E_{dis}	E_{rep}	E_{tot}	Lattice energy
🟥	1	-x, -y, -z	7.08	HF/3-21G	-20.4	-4.7	-36.0	19.8	-40.2	-20.1
🟧	1	-x, -y, -z	7.21	HF/3-21G	-18.8	-4.7	-23.5	14.0	-32.1	-16.05
🟨	2	x, y, z	4.88	HF/3-21G	-10.7	-4.5	-92.6	43.9	-61.7	-61.7
🟩	1	-x, -y, -z	7.24	HF/3-21G	-15.7	-4.7	-33.9	20.6	-32.9	-16.45
🟩	1	-x, -y, -z	6.92	HF/3-21G	-20.5	-3.2	-37.3	28.4	-33.5	-16.75
🟦	1	-x, -y, -z	14.26	HF/3-21G	-5.2	-1.5	-23.3	12.7	-17.0	-8.5
🟦	2	x, y, z	12.98	HF/3-21G	-3.8	-0.8	-9.4	3.7	-9.9	-9.9
🟦	1	-x, -y, -z	15.88	HF/3-21G	0.6	-0.5	-4.6	1.2	-2.9	-1.45
🟪	2	x, y, z	14.92	HF/3-21G	-0.3	-0.7	-8.1	3.6	-5.1	-5.1
🟥	1	-x, -y, -z	16.71	HF/3-21G	3.1	-0.9	-10.6	4.4	-3.4	-1.7

Table 2a.13 The interaction energies (in kJ mol^{-1}) of HL^7 Ligand molecule with neighbouring molecules.

	N	Symop	R	Electron Density	E_{ele}	E_{pol}	E_{dis}	E_{rep}	E_{tot}	Lattice energy
🟥	1	-x, -y, -z	12.91	HF/3-21G	-2.4	-2.1	-18.7	9.3	-13.2	-6.6
🟧	2	x, y, z	8.99	HF/3-21G	-12.8	-6.1	-40.4	22.5	-35.2	-35.2
🟨	1	-x, -y, -z	4.37	HF/3-21G	-27.1	-10.2	-137.9	63.3	-107.2	-53.6
🟩	1	-x, -y, -z	8.62	HF/3-21G	-83.9	-24.4	-84.8	95.7	-100.1	-50.05
🟩	2	x, y, z	13.91	HF/3-21G	-0.6	-0.2	-3.5	0.0	-3.9	-3.9
🟩	1	-x, -y, -z	10.16	HF/3-21G	-5.1	-3.1	-30.9	14.9	-23.0	-11.5
🟦	1	-x, -y, -z	9.91	HF/3-21G	-1.9	-2.2	-38.6	20.4	-21.6	-10.8
🟦	1	-x, -y, -z	8.34	HF/3-21G	-9.0	-4.9	-45.4	18.3	-38.5	-19.25
🟦	1	-x, -y, -z	14.66	HF/3-21G	-1.0	-1.9	-30.3	20.6	-12.8	-6.4
🟪	2	x, y, z	15.43	HF/3-21G	-5.8	-0.9	-6.1	2.3	-10.1	-10.1
🟪	2	x, y, z	16.13	HF/3-21G	0.2	-0.4	-5.7	2.1	-3.4	-3.4
🟥	1	-x, -y, -z	15.46	HF/3-21G	-0.1	-0.3	-2.0	0.0	-2.1	-1.05

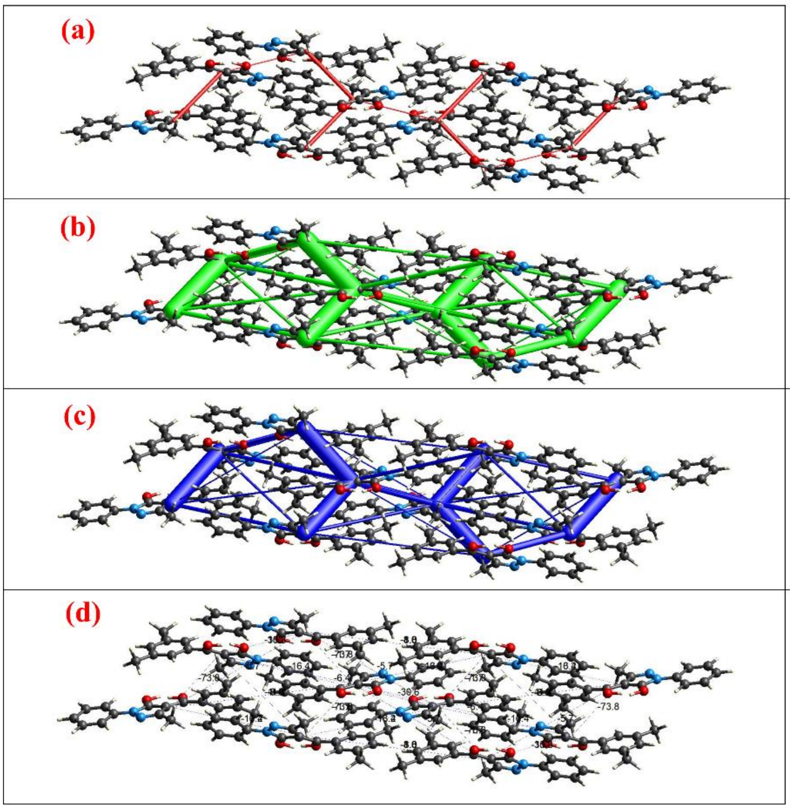

Figure 2a.30 Energy frameworks based on *(a)* Coulomb, *(b)* Dispersion, *(c)* Total, and *(d)* Total energy (annotated) in ligand HL^4.

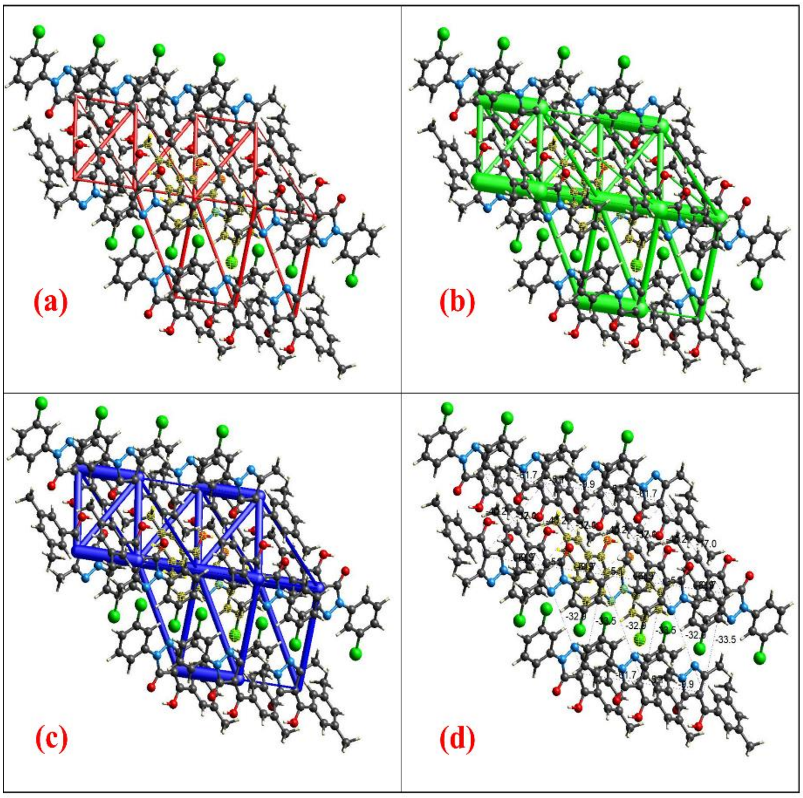

Figure 2a.31 Energy frameworks based on *(a)* Coulomb, *(b)* Dispersion, *(c)* Total, and *(d)* Total energy (annotated) in ligand HL^5.

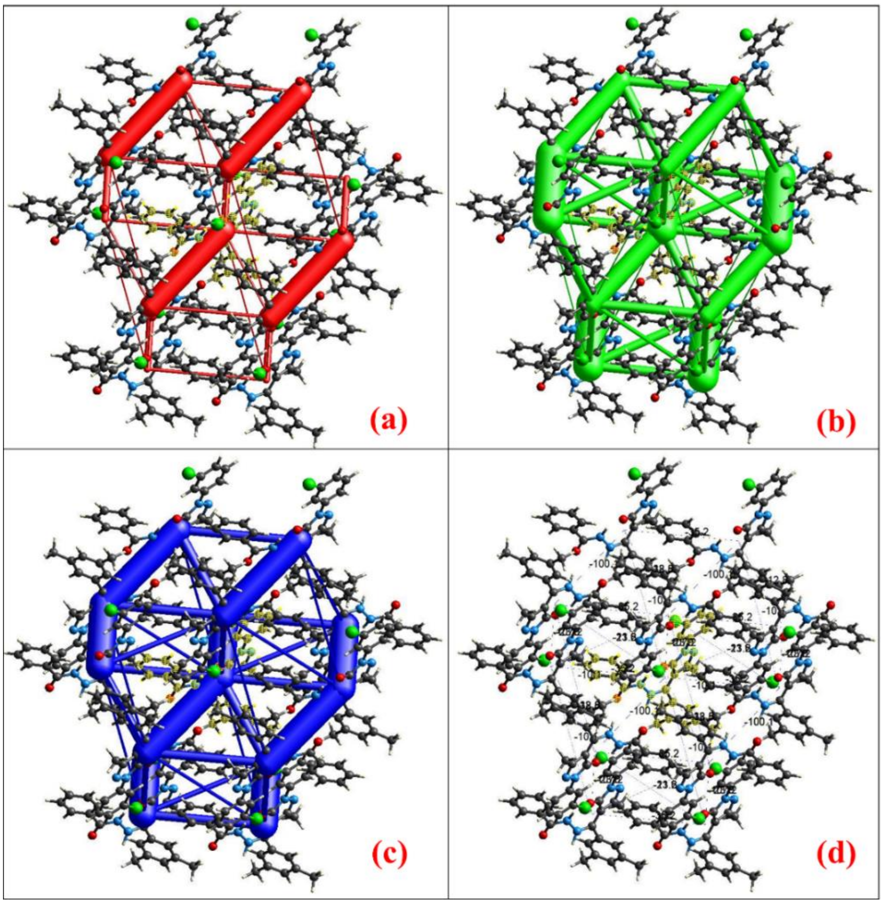

Figure 2a.32 Energy frameworks based on *(a)* Coulomb, *(b)* Dispersion, *(c)* Total, and *(d)* Total energy (annotated) in ligand HL^7.

2D FP (fingerprint) plots were generated using Crystal Explorer 17.5 software to visualize donor-acceptor interaction sites in ligands, mapping over d_{norm}, shape index, curvedness, fragment patch, etc [23]. Figure 2a.33 illustrates the molecular Hirshfeld Surface (HS) for ligand HL^4. Similar molecular HS for ligands HL^5 and HL^7 are displayed in Figures 2a.34 and 2a.35, respectively. The presence of bold and bright red spots in the d_{norm} plot of HS indicates intra- or intermolecular hydrogen bonding interactions within the molecule. Additionally, weaker red marks from closer proximity to neighbouring molecules or shorter interactions between halogen bonds are evident on the d_{norm} surface [25,26]. As a function of di and de from the pointed nuclei with interior and exterior to the HS, respectively, the shortest distances provide surface points that collectively contribute to the d_{norm} area. Curvedness is determined by the HS's rms (root mean square) curvature, where flat surfaces and sharp surfaces correspond to low and high curvedness, respectively. The colour patches on the fragment patch indicate their proximity to adjacent molecules. Such colour patches with their corresponding area (in Å^2) are also depicted in Figures 2a.33-2a.35.

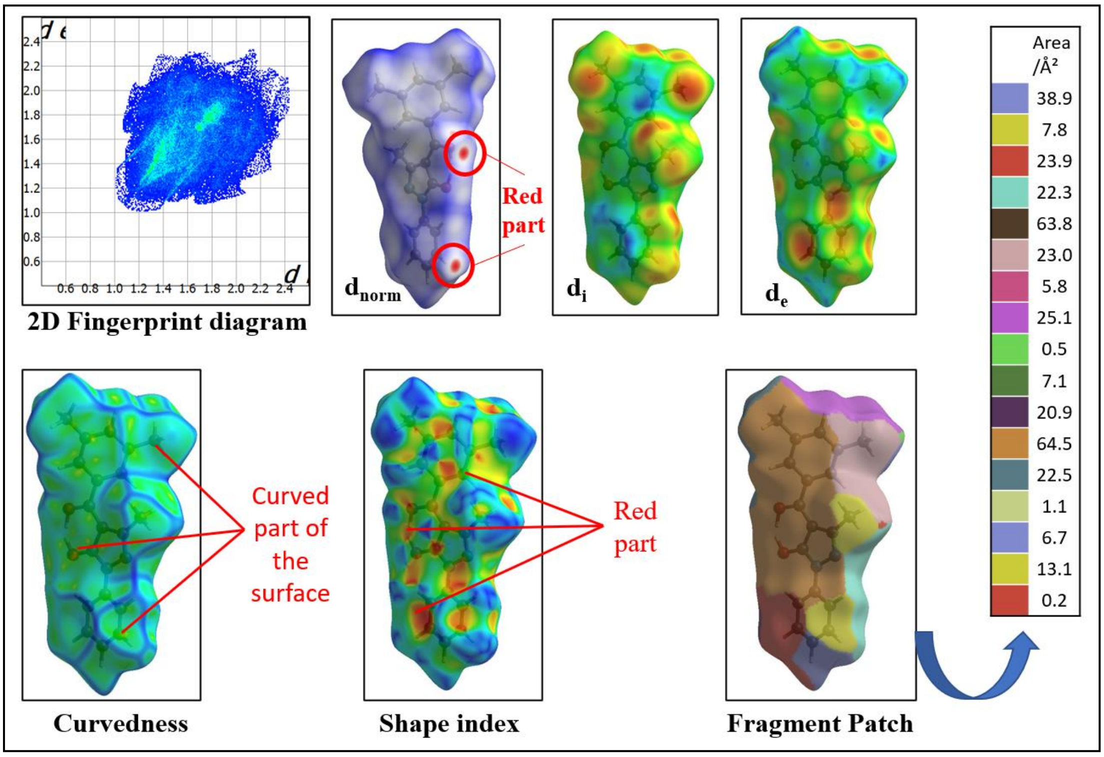

Figure 2a.33 The molecular HS (full FP diagram, d_{norm}, d_i, d_e, Curvedness, Shape index, and fragment patch) for HL^4 ligand.

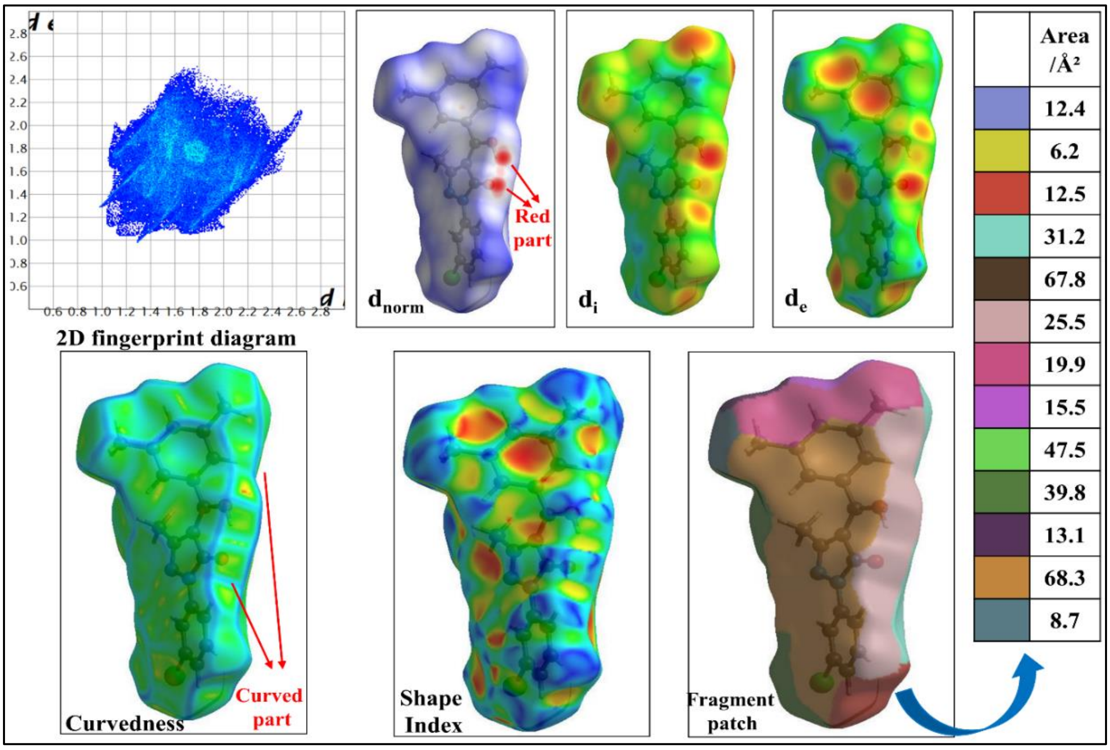

Figure 2a.34 The molecular HS (full FP diagram, d_{norm}, d_i, d_e, Curvedness, Shape index, and fragment patch) for HL^5 ligand.

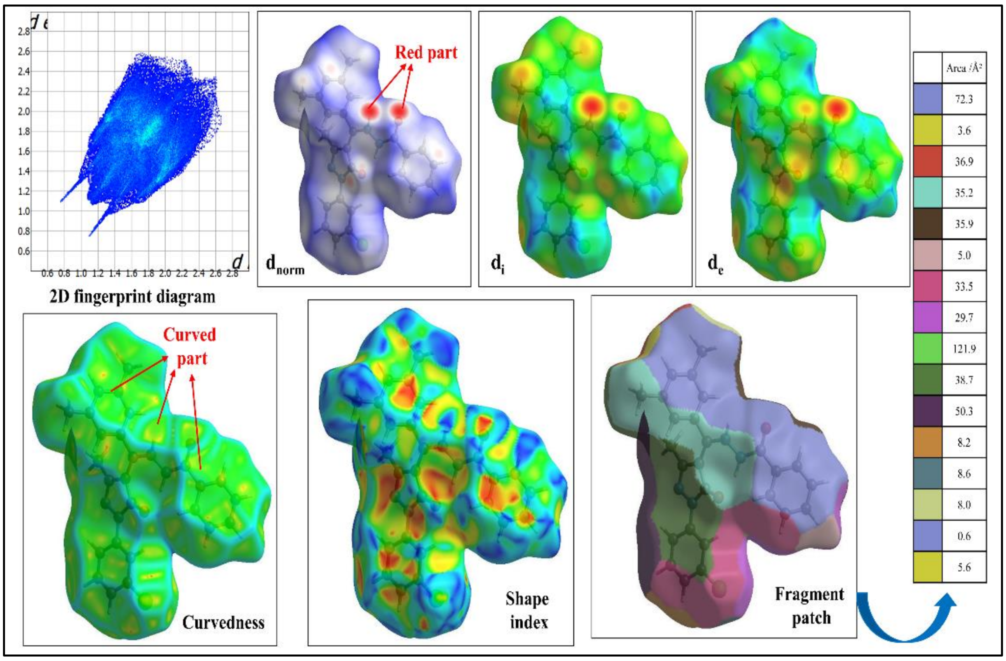

Figure 2a.35 The molecular HS (full FP diagram, d_{norm}, d_i, d_e, Curvedness, Shape index, and fragment patch) for HL^7 ligand.

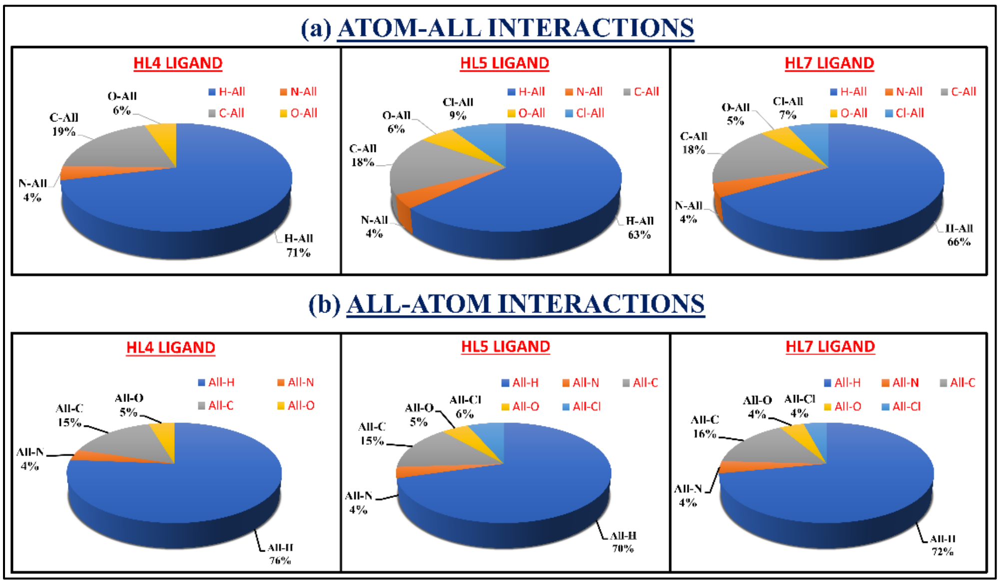

Figure 2a.36 Graphical presentation of percentage interactions in HL^4, HL^5 and HL^7 ligands.

Percentage data for atom-all and all-atom interactions provide an idea about the packing probability in ligands. H-atoms have shown significant interactions for all ligands. The comparative percentage interactions corresponding to C-All, Cl-All, N-All, O-All, All-C, All-Cl, All-N, and All-O for HL^4, HL^5 and HL^7 are given in the bar chart in Figure 2a.36. Two-dimensional fingerprint plots representing all such interactions are depicted in Figures 2a.37-2a.39.

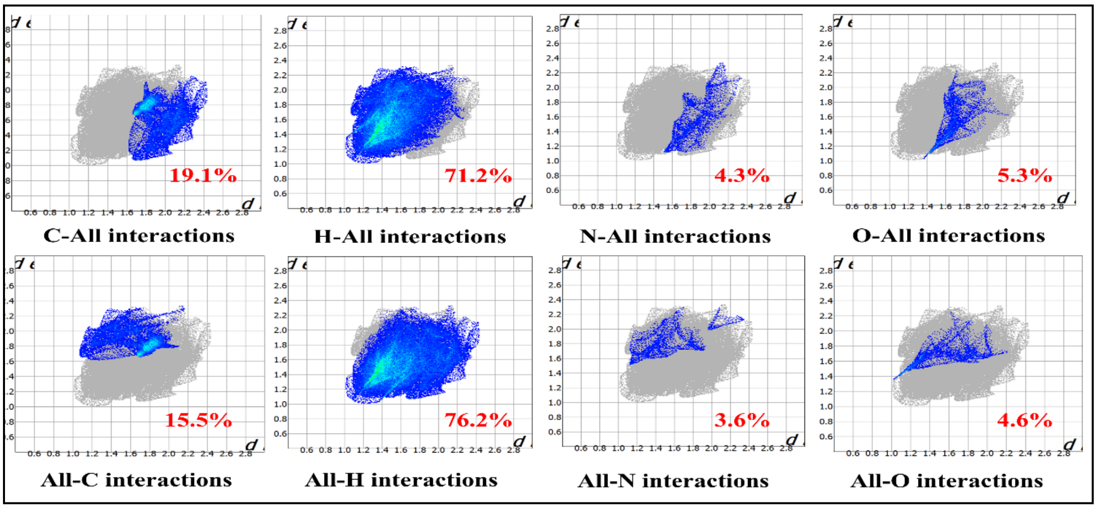

C-All interactions H-All interactions N-All interactions O-All interactions

All-C interactions All-H interactions All-N interactions All-O interactions

Figure 2a.37 2D Fingerprint map for HL^4 ligand.

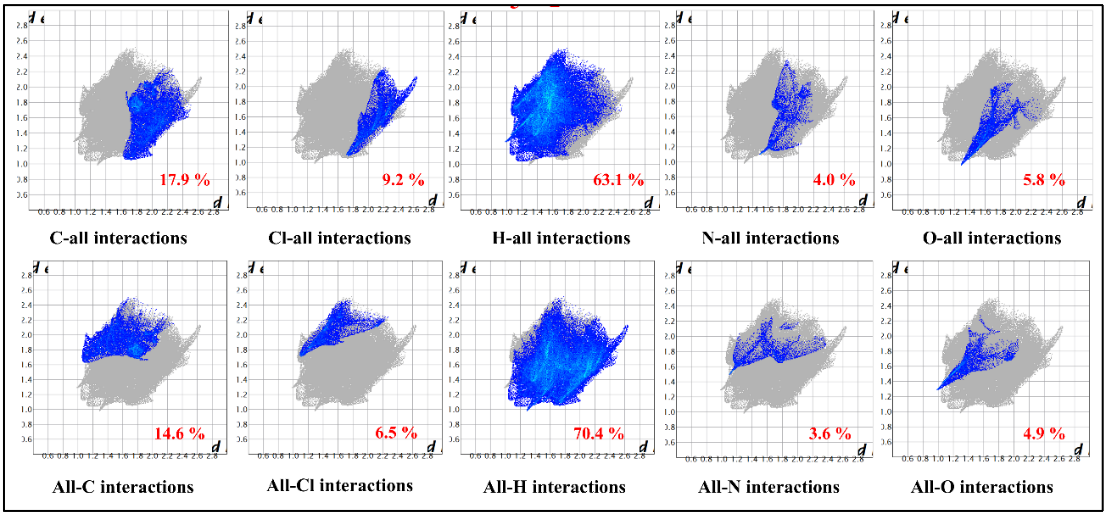

C-all interactions Cl-all interactions H-all interactions N-all interactions O-all interactions

All-C interactions All-Cl interactions All-H interactions All-N interactions All-O interactions

Figure 2a.38 2D Fingerprint map for HL^5 ligand.

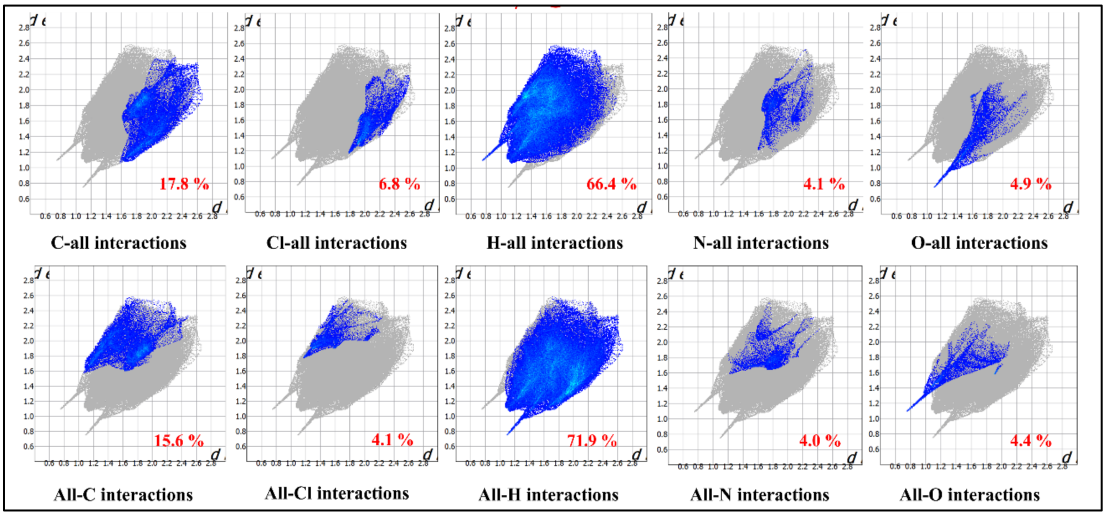

C-all interactions Cl-all interactions H-all interactions N-all interactions O-all interactions

All-C interactions All-Cl interactions All-H interactions All-N interactions All-O interactions

Figure 2a.39 2D Fingerprint map for HL^7 ligand.

2a.4 Conclusions

Three bidentate (HL^4, HL^5, and HL^6) and one tridentate (HL^7) acylpyrazolone ligands were synthesized and thoroughly characterized using various techniques such as FT-IR, ^{1}H-NMR, ^{13}C-NMR, single-crystal X-ray diffraction, Mass Spectrometry, DFT calculations, etc. These characterization methods were employed to investigate their structure, geometry, composition, surface interactions, and lattice energy. Structural elucidations primarily relied on FT-IR, Mass Spectrometry, ^{1}H-NMR, ^{13}C-NMR, and single-crystal X-ray diffraction data. DFT calculations were conducted to establish a strong correlation and comparison with experimental values, aiding in identifying global index parameters to understand these systems' physical and chemical properties. Theoretical investigations included analyzing HOMO-LUMO energy gaps and theoretical vibrations. Additionally, Hirshfeld surface analysis was carried out to assess crystal strength through interaction energies and energy frameworks, detailing intermolecular non-covalent surface interactions with fingerprint plot analyses for all ligands.

References

[1] S. Fustero, M. Sánchez-Roselló, P. Barrio, A. Simón-Fuentes, From 2000 to Mid-2010: A Fruitful Decade for the Synthesis of Pyrazoles, Chem Rev 111 (2011) 6984–7034. https://doi.org/10.1021/cr2000459.

[2] F. Marchetti, C. Pettinari, R. Pettinari, Acylpyrazolone ligands: Synthesis, structures, metal coordination chemistry and applications, Coord Chem Rev 249 (2005) 2909–2945. https://doi.org/10.1016/j.ccr.2005.03.013.

[3] Jensen, B. Skytte, The Synthesis of 1-Phenyl-3-methyl-4-acyl-pyrazolones-5, Acta Chem Scand 13 (1959) 1668–1670. https://doi.org/10.3891/acta.chem.scand.13-1668.

[4] F. Marchetti, R. Pettinari, C. Pettinari, Recent advances in acylpyrazolone metal complexes and their potential applications, Coord Chem Rev 303 (2015) 1–31. https://doi.org/10.1016/j.ccr.2015.05.003.

[5] F. Marchetti, C. Pettinari, C. Di Nicola, A. Tombesi, R. Pettinari, Coordination chemistry of pyrazolone-based ligands and applications of their metal complexes, Coord Chem Rev 401 (2019) 213069. https://doi.org/10.1016/j.ccr.2019.213069.

[6] H. Chai, G. Liu, L. Liu, D. Jia, Synthesis and spectroscopic study on photochromism of a new thiosemicarbazone compound containing pyrazolone, Spectrochim Acta A Mol Biomol Spectrosc 61 (2005) 2590–2594. https://doi.org/10.1016/j.saa.2004.09.027.

[7] J. Guo, H. Yuan, D. Jia, M. Guo, Y. Li, Synthesis and improved photochromic properties of pyrazolones in the solid state by incorporation of halogen, Spectrochim Acta A Mol Biomol Spectrosc 171 (2017) 149–154. https://doi.org/10.1016/j.saa.2016.07.052.

[8] G. Wang, J. Qin, C.-R. Li, Z. Yang, A highly selective fluorescent probe for Al^{3+} based on quinoline derivative, Spectrochim Acta A Mol Biomol Spectrosc 150 (2015) 21–25. https://doi.org/10.1016/j.saa.2015.05.041.

[9] H. Liu, J. Guo, D. Jia, M. Guo, F. Le, L. Liu, D. Wu, F. Li, Modulation of a solid-state reversible fluorescent photoswitching based on a controllable photochromic pyrazolones, J Solid State Chem 216 (2014) 73–78. https://doi.org/10.1016/j.jssc.2014.04.020.

[10] C. Deng, S. Abdurehman, L. Liu, D. Wu, D. Jia, R. Zhou, Synthesis, photoisomerization properties and thermal bleaching kinetics of pyrazolones containing 3-cyanobenzal, Spectrochim Acta A Mol Biomol Spectrosc 148 (2015) 318–323. https://doi.org/10.1016/j.saa.2015.04.001.

[11] I. Shaikh, R.N. Jadeja, R. Patel, V. Mevada, V.K. Gupta, 4-Acylhydrazone-5-Pyrazolones and their Zinc(II) Metal Complexes: Synthesis, Characterization, Crystal Feature and Antimalarial Activity, J Mol Struct 1232 (2021) 130051. https://doi.org/10.1016/j.molstruc.2021.130051.

[12] I. Shaikh, M. Travadi, R.N. Jadeja, R.J. Butcher, J.H. Pandya, Crystal feature and spectral characterization of Zn(II) complexes containing Schiff base of Acylpyrazolone ligand with antimalarial action, J Indian Chem Soc 99 (2022) 100428. https://doi.org/10.1016/j.jics.2022.100428.

[13] Vogel, I. Arthur, Vogel's textbook of macro and semimicro qualitative inorganic analysis., 6th ed., Longman Scientific & Technical, Wiley, Harlow, Essex, England: New York, 1987. https://doi.org/https://nla.gov.au/nla.cat-vn122464.

[14] I. Shaikh, R.N. Jadeja, R. Patel, Three mixed ligand mononuclear Zn(II) complexes of 4-acyl pyrazolones: Synthesis, characterization, crystal study and anti-malarial activity, Polyhedron 183 (2020) 114528. https://doi.org/10.1016/j.poly.2020.114528.

[15] A.K. Patel, R.N. Jadeja, H. Roy, R.N. Patel, S.K. Patel, R.J. Butcher, Pseudo-tetrahedral copper(II) complex derived from N'-[(2E,3Z)-4-hydroxy-4-phenylbut-3-en-2-ylidene]acetohydrazide: Synthesis, molecular structure, quantum chemical investigations, antioxidant and antiproliferative properties, J Mol Struct 1185 (2019) 341–350. https://doi.org/10.1016/j.molstruc.2019.03.004.

[16] G.M. Sheldrick, SHELXT – Integrated space-group and crystal-structure determination, Acta Crystallogr Section A 71 (2015) 3–8. https://doi.org/10.1107/S2053273314026370.

[17] G.M. Sheldrick, Crystal structure refinement with SHELXL, Acta Crystallogr Section C 71 (2015) 3–8. https://doi.org/10.1107/S2053229614024218.

[18] K. Nakum, R.N. Jadeja, Synthesis, characterization, and electrochemical study of a mononuclear Cu(II) complex with a 4-acyl pyrazolone ligand, Z Naturforsch B 73 (2018) 713–718. https://doi.org/doi:10.1515/znb-2018-0117.

[19] B. Kumar, K.J. Nakum, R.N. Jadeja, R. Kant, V.K. Gupta, Crystal structure of [1-(3-chlorophenyl)-5-hydroxy-3-methyl-1 H-pyrazol-4-yl](p-tolyl)methanone, Acta Crystallogr Section E 71 (2015) o280–o281. https://doi.org/10.1107/S2056989015006258.

[20] D. Shoba, S. Periandy, M. Karabacak, S. Ramalingam, Vibrational spectroscopy (FT-IR and FT-Raman) investigation, and hybrid computational (HF and DFT) analysis on the structure of 2,3-naphthalenediol, Spectrochim Acta A Mol Biomol Spectrosc 83 (2011) 540–552. https://doi.org/10.1016/j.saa.2011.09.002.

[21] R.N. Patel, S.K. Patel, D. Kumhar, N. Patel, A.K. Patel, R.N. Jadeja, N. Patel, R.J. Butcher, M. Cortijo, S. Herrero, Two new copper(II) binuclear complexes with 2-[(E)-(pyridine-2yl-hydrazono)methyl]phenol: Molecular structures, quantum chemical calculations, cryomagnetic properties and catalytic activity, Polyhedron 188 (2020) 114687. https://doi.org/10.1016/j.poly.2020.114687.

[22] Y. Singh, R.N. Patel, S.K. Patel, A.K. Patel, N. Patel, R. Singh, R.J. Butcher, J.P. Jasinski, A. Gutierrez, Experimental and quantum computational study of two new bridged copper(II) coordination complexes as possible models for antioxidant superoxide dismutase: Molecular structures, X-band electron paramagnetic spectra and cryogenic magnetic properties, Polyhedron 171 (2019) 155–171. https://doi.org/10.1016/j.poly.2019.07.015.

[23] P.R. Spackman, M.J. Turner, J.J. McKinnon, S.K. Wolff, D.J. Grimwood, D. Jayatilaka, M.A. Spackman, CrystalExplorer: a program for Hirshfeld surface analysis, visualization and quantitative analysis of molecular crystals, J Appl Crystallogr 54 (2021) 1006–1011. https://doi.org/10.1107/S1600576721002910.

[24] C.F. Mackenzie, P.R. Spackman, D. Jayatilaka, M.A. Spackman, CrystalExplorer model energies and energy frameworks: extension to metal coordination compounds, organic salts, solvates and open-shell systems, IUCrJ 4 (2017) 575–587. https://doi.org/10.1107/S205225251700848X.

[25] M.K. Patel, U.H. Patel, S.A. Gandhi, V.M. Barot, J. Jayswal, Solvent effect on neutral Co (II) complexes of paeonol derivative –qualitative and quantitative studies from energy frame work and Hirshfeld surface analysis, J Mol Struct 1196 (2019) 119–131. https://doi.org/10.1016/j.molstruc.2019.06.050.

[26] A.P. Novikov, M.A. Volkov, A.V. Safonov, M.S. Grigoriev, Synthesis, Crystal Structure, and Hirshfeld Surface Analysis of Hexachloroplatinate and Tetraclorouranylate of 3-Carboxypyridinium—Halogen Bonds and π-Interactions vs. Hydrogen Bonds, Crystals (Basel) 12 (2022). https://doi.org/10.3390/cryst12020271.

CHAPTER 2

Part (b): Synthesis, Covalency Sequence, and Crystal Features of Pentagonal Uranyl Acylpyrazolone Complexes along with DFT Calculation and Hirshfeld Analysis.

2b.1 Introduction

The significance of actinides in nuclear weapons, defence operations, and energy production has increased in recent decades [1–3]. Within the nuclear fuel cycle and weapon development, understanding the speciation of uranium and plutonium is essential for their migration pathways [4]. Uranium and thorium are particularly important within the actinide series due to their durable characteristics, studied through complex construction. In coordination chemistry, solvent extraction plays a crucial role in separating actinide series [5,6]. Additionally, the ion exchange method is widely used and effective in the separation process due to actinides' diverse ionic and covalent properties [7].

Despite the availability of numerous sophisticated separation techniques, comprehensive studies on every aspect of actinides are challenging, hazardous, and expensive. In such circumstances, it becomes meaningful to investigate a readily available element that can represent some elements. Although uranium chemistry differs from other actinides, the isotope ^{238}U is a cheap and easily accessible alternative, albeit not representative of minor actinides like americium and curium. Redox variability plays a crucial role in separations and corrosion science due to the ability of uranium to exist in various oxidation states [8]. Moreover, the straightforward synthesis method and rapid crystallization of uranium complexes have prioritized their study within the actinide series to understand their properties through the most feasible methods. In terms of efficacy, uranium finds diverse applications, including chemotoxicity and radiotoxicity studies [9], redox flow batteries [10], NMR shift reagents [11], and enhanced catalytic activity [9,12–14]. The broad range of functions exhibited by uranium complexes is attributed primarily to their binding capacity and the array of oxidation states they can assume. Numerous uranium complexes with oxidation states ranging from +3 to +6 have been investigated, with hexavalent uranyl (UO_2^{2+}) complexes often displaying the highest stability. According to the HSAB theory, the hard acid UO_2^{2+} forms stable complexes with ligands featuring hard base donor atoms [15]. The reduction of uranyl ions to $U^{(V)}O_2^{+}$ and $U^{(IV)}$ is typically achieved through anaerobic bacterial reduction or synthetic methods for redox research studies [16,17].

Over the past few decades, research has led to the discovery of uranyl acylpyrazolone complexes, which have proven stable and offer a wide range of potential applications. The original and fundamental concept of utilizing the covalent bond between metal and ligand in these complexes has been invaluable in understanding their properties. This study focuses on synthesizing uranyl complexes with acyl pyrazolone ligands with the objectives mentioned above. The key points of the chapter include (i) synthesizing four UO_2^{2+} complexes derived from bidentate acylpyrazolone ligands, (ii) employing comprehensive characterization techniques to provide detailed bonding information, (iii) examining the nature and binding capacity of acylpyrazolones, and (iv) analyzing and comparing the covalent bond strengths using data obtained from characterization analyses.

2b.2 Experimental section

2b.2.1 Materials and Methods

HL^1, HL^2, and HL^3 ligands were synthesized and analyzed employing the methodologies outlined in our laboratory's publications [18,19]. The procedures and characterization of HL^4 ligand were conducted following the instructions provided in Chapter 2a. Uranyl nitrate procured from SULAB Chemicals in Gujarat was introduced into the solution. The uranium concentration was determined using gravimetric techniques, expressed as U_3O_8 [20]. AR-grade solvents for recrystallization were purchased from CDH Chemicals, a Central Drug House (P) Ltd division.

2b.2.2 Synthesis of uranium complexes

The uranium complexes 1, 2, 3 and 4 were synthesized using the procedure outlined in Figure 2b.1 using HL^1, HL^2, HL^3, and HL^4 ligands, respectively.

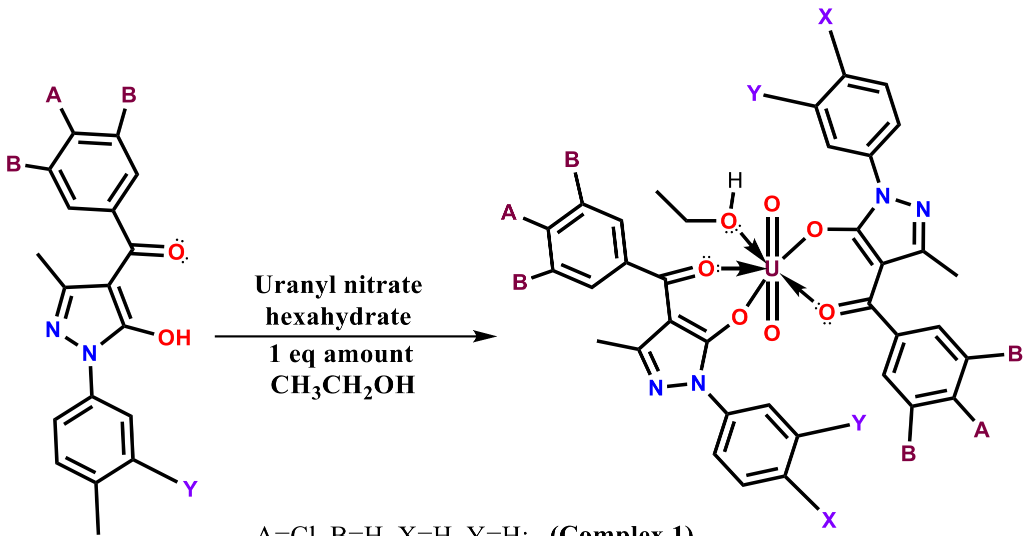

A=Cl, B=H, X=H, Y=H; **(Complex 1)**
A=Cl, B=H, X=H, Y=Cl; **(Complex 2)**
A=Cl, B=H, X=CH_3, Y=H; **(Complex 3)**
A=H, B=CH_3, X=H, Y=H; **(Complex 4)**

U-complex

Figure 2b.1 Synthetic route for uranyl complexes.

Synthesis of Complex 1

Complex 1 was prepared using HL^1 ligand (2 mmol, 0.625 g) and uranyl nitrate hexahydrate (1 mmol, 0.500 g). Then, it was recrystallized in DMSO with a slow evaporation technique at room temperature (~32 °C), in which a DMSO molecule replaced ethanol. Yield (%): 82.68% (complex obtained: 0.772 g), M.P.: ~190 °C, Molecular formula: $C_{36}H_{30}Cl_2N_4O_7U$, Formula wt: 938.2 g mol^{-1}, % Metal (achieve): U, 24.56 (25.33) %. **FTIR (KBr, cm^{-1}):** 1577 (C=O, p-chlorobenzoyl), 1557 (C=O, pyrazolone), 1472 (cyclic C=N), 920 (U=O, asym.), 833 (U=O, sym.). **^{1}H-NMR δ-ppm (400MHz, DMSO-d$_6$):** 4.310 (m, 2H, $OCH_{2(CH3CH2OH)}$), 7.0-8.5 (m, Ar-H_{L1}), 2.085 (s, 3H, Pyz-CH_3), 1.982 (s, 3H, Pyz-CH_3), 1.055 (t, 3H, $CH_{3(CH3CH2OH)}$).

Synthesis of Complex 2

Using HL^2 ligand (2 mmol, 0.695 g) in the complex mentioned above 1 preparation, complex 2 was synthesized similarly. However, a single crystal of pale-yellow colour and prism shape was produced by recrystallising in DMF. Yield (%): 86% (complex obtained: 0.864 g), M.P.: ~162 °C, Molecular formula: $C_{36}H_{28}Cl_4N_4O_7U$, Formula wt: 1008.47 g mol^{-1}, % Metal (achieve): U, 23.56 (23.60) %. **FTIR (KBr, cm^{-1}):** 1591 (C=O, p-chlorobenzoyl), 1557 (C=O, pyrazolone), 1471 (cyclic C=N), 863 (U=O, asym.), 778 (U=O, sym.). **^{1}H-NMR δ-ppm (400MHz, DMSO-d$_6$):** 4.410 (m, 2H, $OCH_{2(CH3CH2OH)}$), 7.0-8.5 (m, Ar-H_{L2}), 1.993 (s, 3H, Pyz-CH_3), 1.958 (s, 3H, Pyz-CH_3), 1.054 (t, 3H, $CH_{3(CH3CH2OH)}$).

Synthesis of Complex 3

Using the HL^3 ligand, complex 3 was synthesised in a manner like that described before. A pale yellow, prism-shaped single crystal was produced by recrystallising the compound in DMSO. Yield (%): 84% (complex obtained: 0.809 g), M.P.: ~165 °C, Molecular formula: $C_{38}H_{34}Cl_2N_4O_7U$, Formula wt: 967.64 g mol^{-1}, % Metal (achieve): U, 24.12 (24.60) %. **FTIR (KBr, cm^{-1}):** 1591 (C=O, p-chlorobenzoyl), 1558 (C=O, pyrazolone), 1436 (ring C=N), 912 (U=O, asym.), 823 (U=O, sym.). **^{1}H-NMR δ-ppm (400MHz, DMSO-d_6):** 4.418 (m, 2H, $OCH_{2(CH3CH2OH)}$), 7.5-8.5 (m, Ar-H_{L3}), 2.503 (s, 3H, p-tolyl CH_3) 2.083 (s, 3H, Pyz-CH_3), 1.051 (t, 3H, $CH_{3(CH3CH2OH)}$).

Synthesis of Complex 4

Using the HL^4 ligand, complex 4 was synthesised like that described before. An orange-yellow, plate-type single crystal was produced by recrystallising the compound in DMF. Yield (%): 91.40%, M.P.: >200 °C, Molecular formula: $C_{40}H_{40}N_4O_7U$, Formula wt: 926.81, Metal (achieve): U, 25.68 (25.33) %. **FTIR (KBr, cm^{-1}):** 1618 (C=O, 3,5-dimethyl benzoyl), 1602 (C=O, pyrazolone), 1480 (ring C=N), 925 (U=O, asym.), 808 (U=O, sym.). **^{1}H-NMR δ-ppm (400MHz, $CDCl_3$):** 4.322 (q, 2H, $OCH_{2(EtOH)}$, J=3.6 Hz), 5.378 (s, 1H, $OH_{(EtOH)}$), 7.0-9.0 (m, Ar-H_{L4}), 2.743 (s, 3H, Pyz-CH_3), 2.898 (s, 3H, Pyz-CH_3), 1.047 (t, 3H, $CH_{3(EtOH)}$, J=1.6 Hz), 2.519 (s, 6H, $CH_{3(benzoyl)}$), 2.468 (s, 6H, $CH_{3(benzoyl)}$).

2b.2.3 X-ray crystallographic examination

X-ray crystallographic analysis was conducted on all four uranyl complexes using Mo-K_α (λ = 0.71073 Å) radiation and graphite monochromator. The detection and refinement procedures were performed based on the methods outlined in previously published papers from our laboratory [21]. The diffraction data were solved using the SHELXT software [22], while computation was done using the crystallographic software SHELXL-2018/3 [23].

2b.2.4 Physical measurements and characterization techniques

Analogous methodologies, models, instruments, or instruments were employed to analyze the data of the synthesized compounds, utilizing techniques such as FTIR, ^{1}H-NMR, CV-DPV, and TG-DTA, following procedures outlined in previously published articles from our laboratory [19,21]. Electrochemical analysis of the complexes in DMSO containing 0.1 M TBAP as the supporting electrolyte was conducted via CV and DPV employing a three-electrode system under de-aerated conditions and a BAS 100 electrochemical analyzer. A glassy-carbon electrode and platinum wire were the working and counter electrodes. The reversibility of the electrochemical process was evaluated following standard procedures, and all potentials were recorded against an Ag/AgCl reference electrode. Nitric acid decomposition of the complexes facilitated volumetric and gravimetric measurement of uranium content, expressed as U_3O_8.

2b.2.5 Computational study

Geometry optimizations and DFT computations were performed on all four complexes employing the B3LYP method [24–27] and executed using the GAUSSIAN 16 software [27,28]. Input file processing was conducted using Gaussview 6.0 [29,30]. The SDD basis set was used for all components in the three complexes. With this method, calculations were performed to analyze molecular structure, vibrational properties, and other relevant factors.

2b.3 Results and Discussion

The uranyl acylpyrazolone complexes exhibit exceptional stability at ambient temperatures, with uranyl forming covalent bonds with the ligands. Furthermore, the subsequent section elucidates the sequence of covalent bonding along with crystal formations.

2b.3.1 FTIR spectral analysis

The FTIR band of $\upsilon_{O\text{-}H}$ indicates evidence of the binding of one CH_3CH_2OH molecule, typically observed near 3400 cm^{-1}. This observation arises from all four complexes synthesized using 100% ethanol as the solvent. Significant changes in the FTIR spectra of ligands upon complexation can be discerned by comparing them with their corresponding complexes [19]. As demonstrated in Table 2b.1, the $\upsilon_{C=O}$ stretching frequency of the acylpyrazolone and benzoyl groups notably decreases during complexation. For instance, the $\upsilon_{C=O}$ stretching of acylpyrazolone reduces from 1590 cm^{-1} for HL^1 to 1557 cm^{-1} for complex 1, from 1590 cm^{-1} for HL^2 to 1557 cm^{-1} for complex 2, from 1601 cm^{-1} for HL^3 to 1558 cm^{-1} for complex 3, and from 1605 cm^{-1} for HL^4 to 1602 cm^{-1} for complex 4. A similar reduction is observed in the benzoyl carbonyl frequency (see Table 2b.1). This reduction is attributed to the shift of the O-atom charge toward the metal ions during complexation, weakening the C=O bond. For the four complexes as mentioned above, the uranyl asymmetric stretching frequencies are observed at 920 cm^{-1}, 863 cm^{-1}, 912 cm^{-1}, and 925 cm^{-1}, respectively, while corresponding symmetric stretching bands are observed at 833 cm^{-1}, 778 cm^{-1}, 823 cm^{-1}, and 808 cm^{-1}. In the four complexes considered, both asymmetric and symmetric vibrations exhibit a frequency order of complex 4 > 1 > 3 > 2, indicating a similar order of bond strength for uranyl. The reverse order of the relative effect on the U—O bond strength of the pentagonal plane created by these uranyl bonds is responsible for the covalency order 2 > 3 > 1 > 4 for the complexes. Thus, asymmetric and symmetric uranyl stretching frequencies are crucial for identifying the covalency order in uranyl complexes [31,32]. Figures 2b.2-2b.5 depict the FTIR spectra of complexes 1-4, respectively.

Table 2b.1 The FTIR values for uranyl complexes (in cm^{-1}).

Code	$\upsilon_{C=O}$ benzoyl group	$\upsilon_{C=O}$ acyl group	Cyclic $\upsilon_{C=N}$	C-H in plane deformation	$\upsilon_{as\,(U=O)}$	$\upsilon_{s\,(U=O)}$
HL¹	1620	1590	1484	1085	-	-
Complex 1	1577	1557	1472	1013	920	833
HL²	1624	1590	1484	1080	-	-
Complex 2	1591	1557	1471	1089	863	778
HL³	1694	1601	1446	1071	-	-
Complex 3	1591	1558	1436	1089	912	823
HL⁴	1621	1605	1511	1067	-	-
Complex 4	1618	1602	1480	1062	925	808

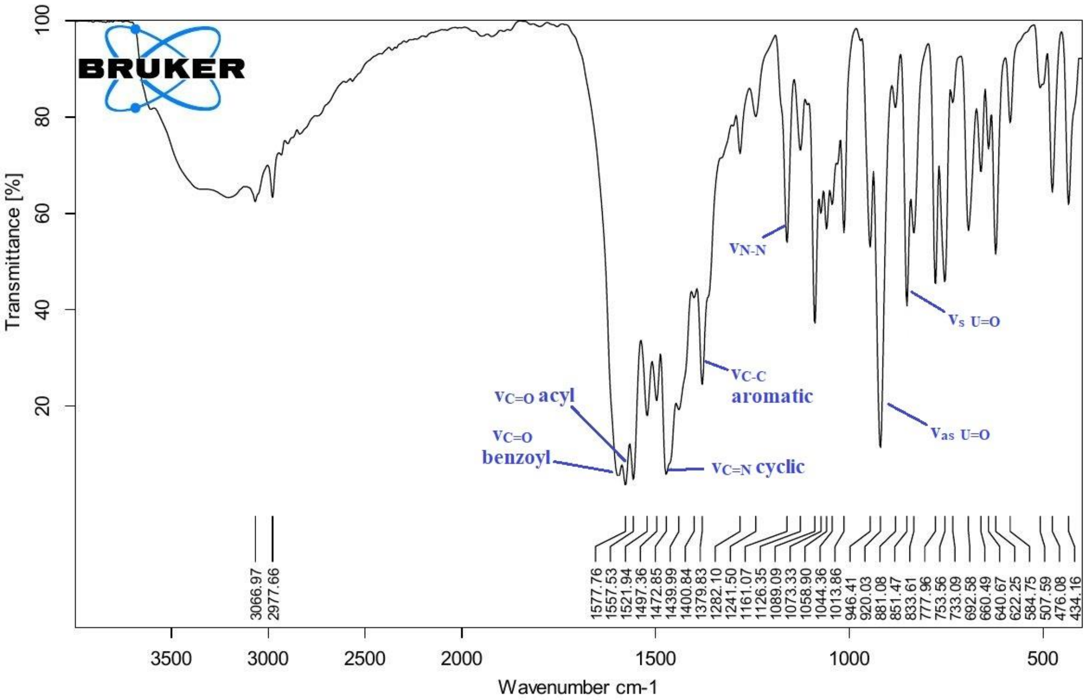

Figure 2b.2 FTIR spectrum for complex 1.

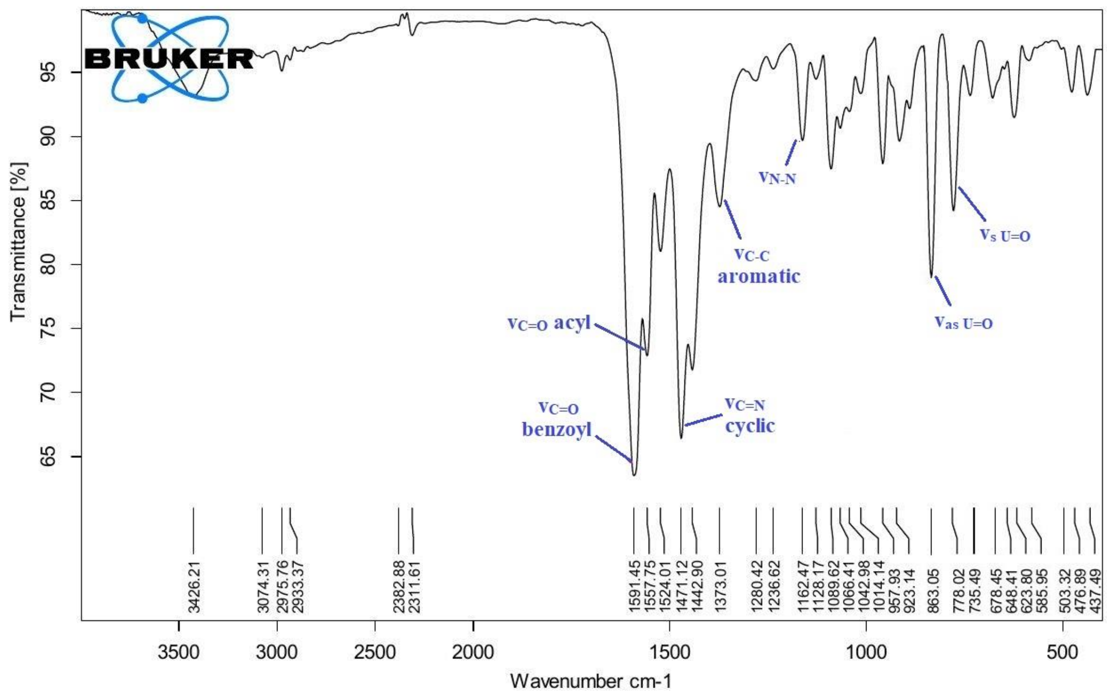

Figure 2b.3 FTIR spectrum for complex 2.

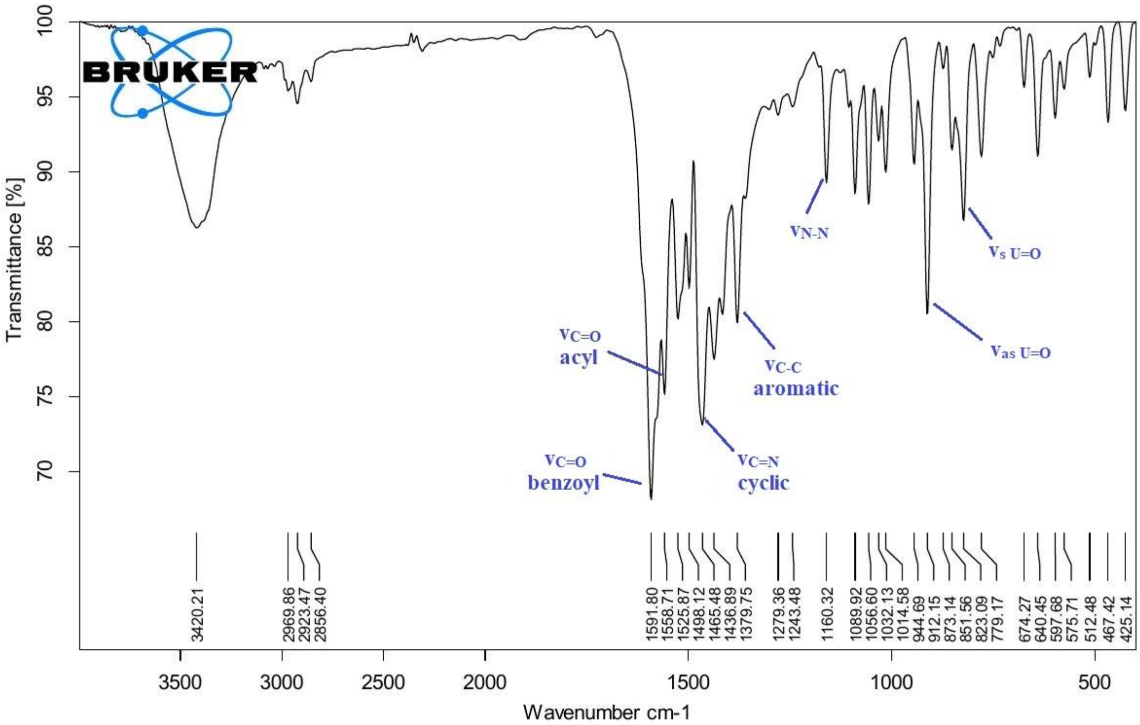

Figure 2b.4 FTIR spectrum for complex 3.

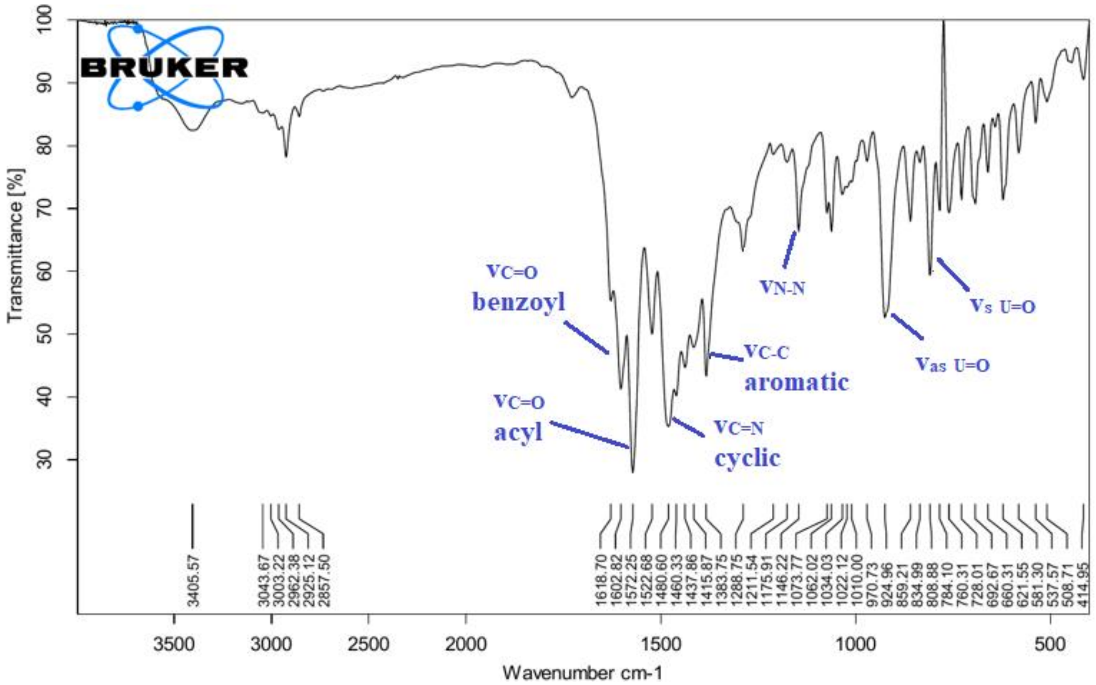

Figure 2b.5 FTIR spectrum for complex 4.

2b.3.2 ^{1}H-NMR spectroscopic study

The ^{1}H-NMR spectra of all representative uranyl complexes were verified in DMSO-d_6, where the phenyl and methyl protons' spectra display sharp lines due to the slower relaxation time of uranyl ions compared to other ions [33]. Across all complexes, a multiplet for the OCH_2 group and a triplet for CH_3 were observed within the range of δ4.0-4.5 ppm and δ1.05-1.06 ppm, respectively. The combination of these peaks confirms the binding of an ethanolic group with the uranyl ion on its fifth coordination site. In complex 3, an additional singlet peak of the CH_3 of p-tolyl was observed at δ2.503 ppm, while complex 4 exhibited a singlet peak of the CH_3 of the 3,5-dimethyl benzoyl group at δ2.419 ppm. Furthermore, multiple multiplets corresponding to aromatic protons were observed in the 6.8–8.6 ppm range in all complexes. The pyrazolone CH_3 appeared as two distinct lines in the complexes, displaying sharp singlets in the free ligands, indicating the arrangement of two ligands in an antisymmetric and dissimilar manner, as previously described [33,34]. Additional information is provided in Figures 2b.6-2b.9, which include PMR spectra for each complex.

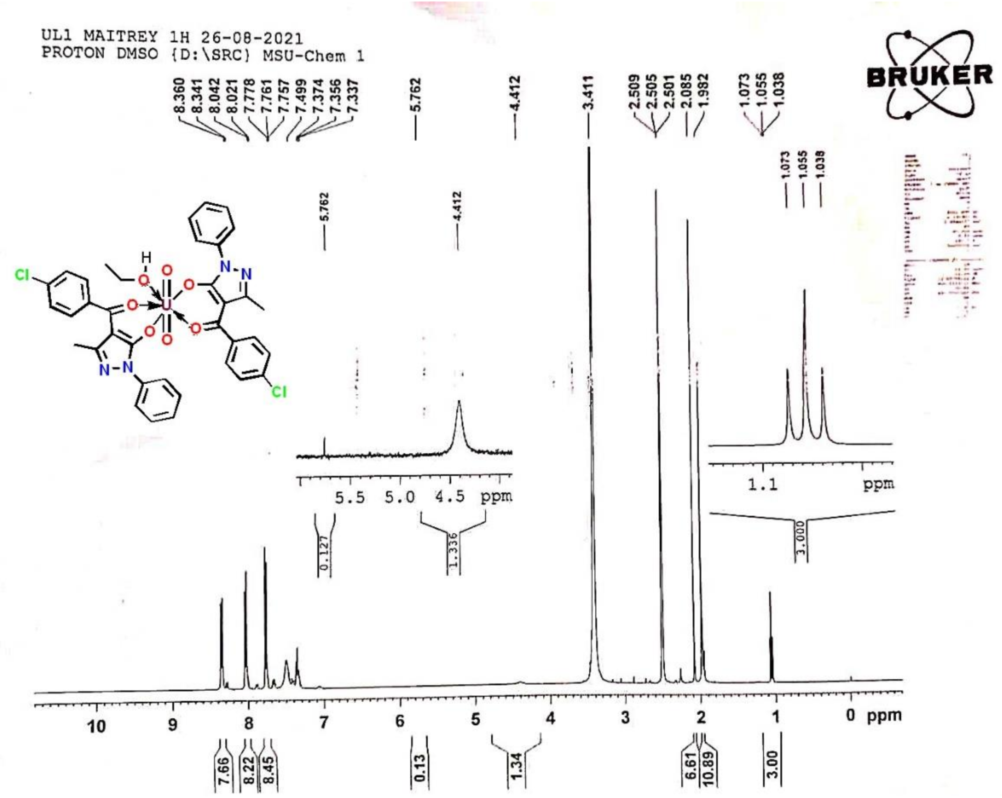

Figure 2b.6 ^{1}H-NMR spectrum of complex 1.

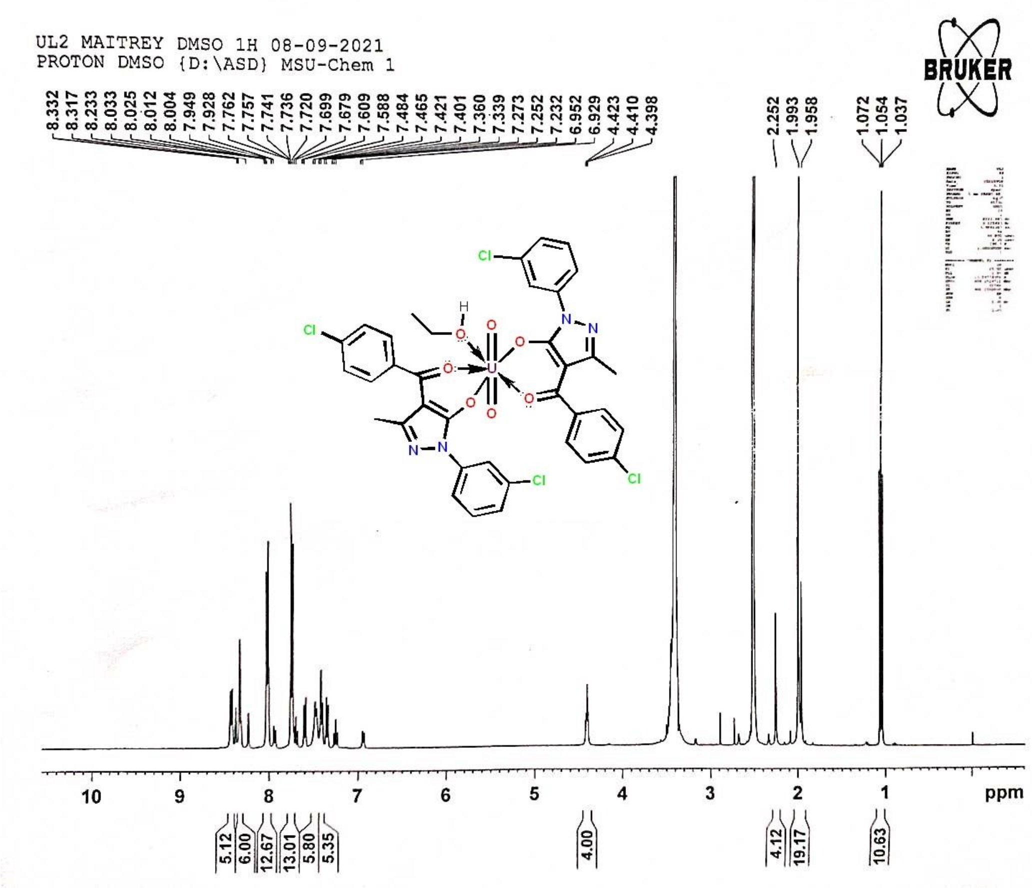

Figure 2b.7 ^{1}H-NMR spectrum of complex 2.

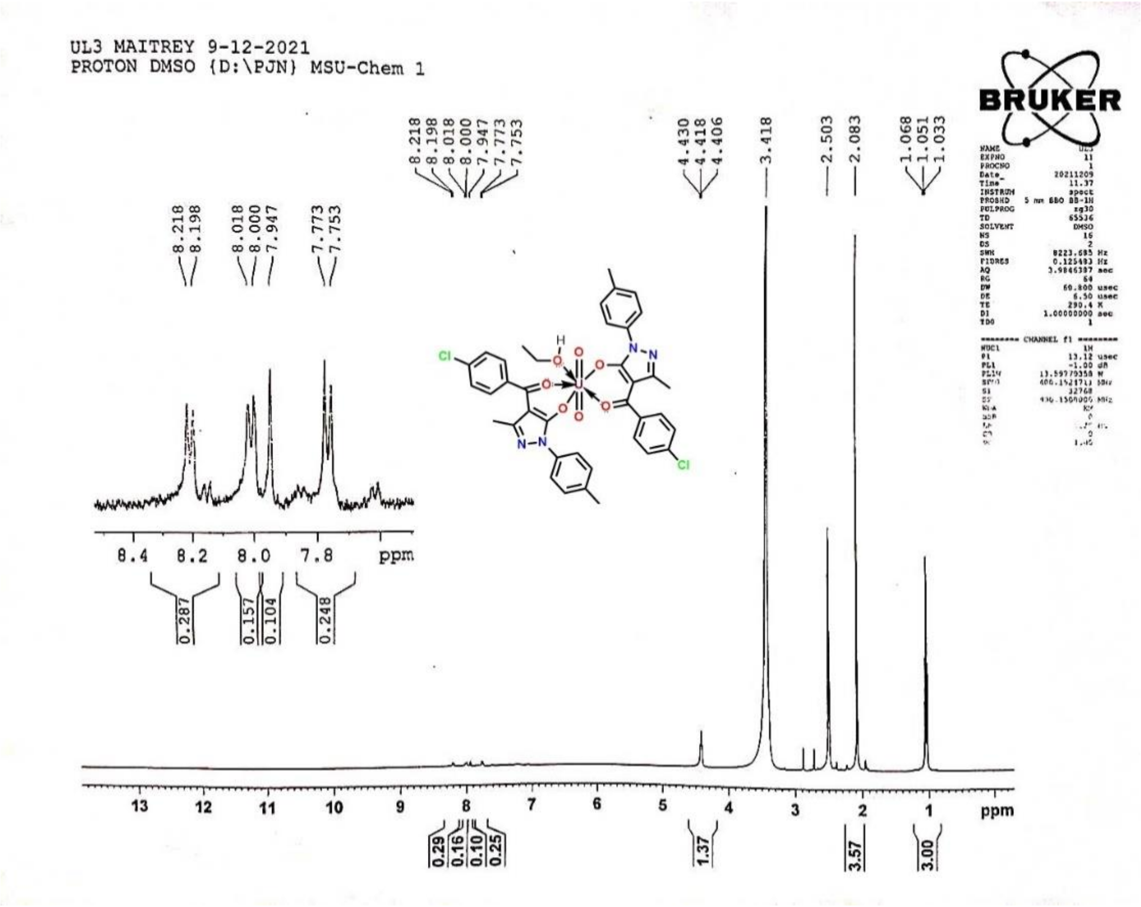

Figure 2b.8 ^{1}H-NMR spectrum of complex 3.

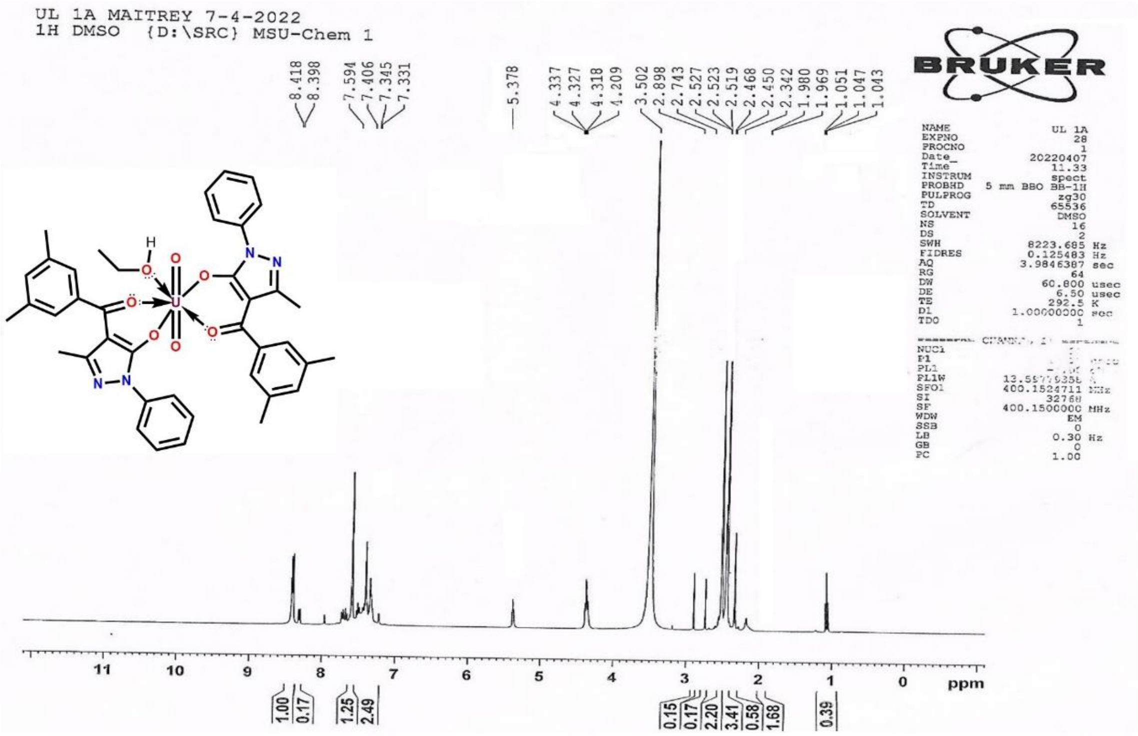

Figure 2b.9 ^{1}H-NMR spectrum of complex 4.

2b.3.3 Thermogravimetric analysis

Thermogravimetric analysis (TGA) data reveals a three-step breakdown process. In the first step, the ethanol moiety is eliminated from the fifth coordination site in complex 1, followed by solvent loss up to 150 °C. A significant shift of 68.8 g/min at 129.6 °C is observed in the derivative thermogravimetric (DTG) curve. The second step involves the removal of the L^1 ligand within the temperature range of 300 to 700 °C. A sharp peak in the differential thermal analysis (DTA) curve indicates the onset of this second step, with a substantial change of 218.8 g/min recorded at 407.8 °C (refer to the DTG curve). The final phase involves converting the metal component into uranium oxide (U_3O_8). Thermogravimetric curves for all four complexes are provided in Figures 2b.10-2b.13. TGA curves of complexes 2, 3, and 4 exhibit a similar pattern, with their maximum decomposition occurring during the second step in the DTG curve within the temperature range of 400-500 °C.

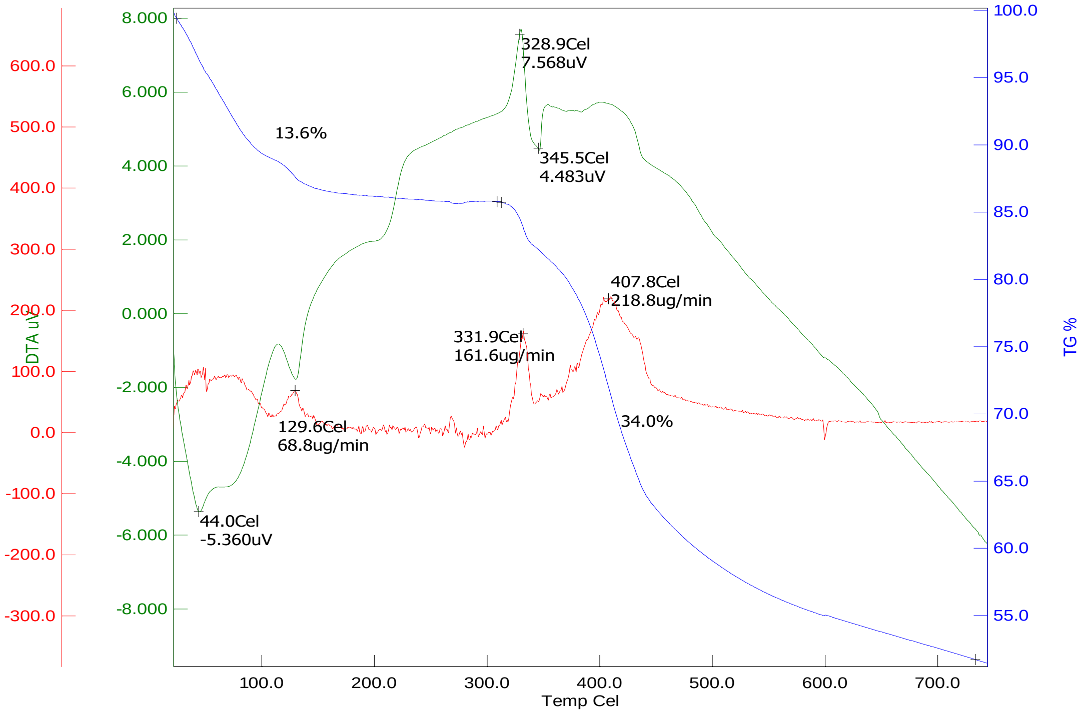

Figure 2b.10 Thermogravimetric curve for complex 1.

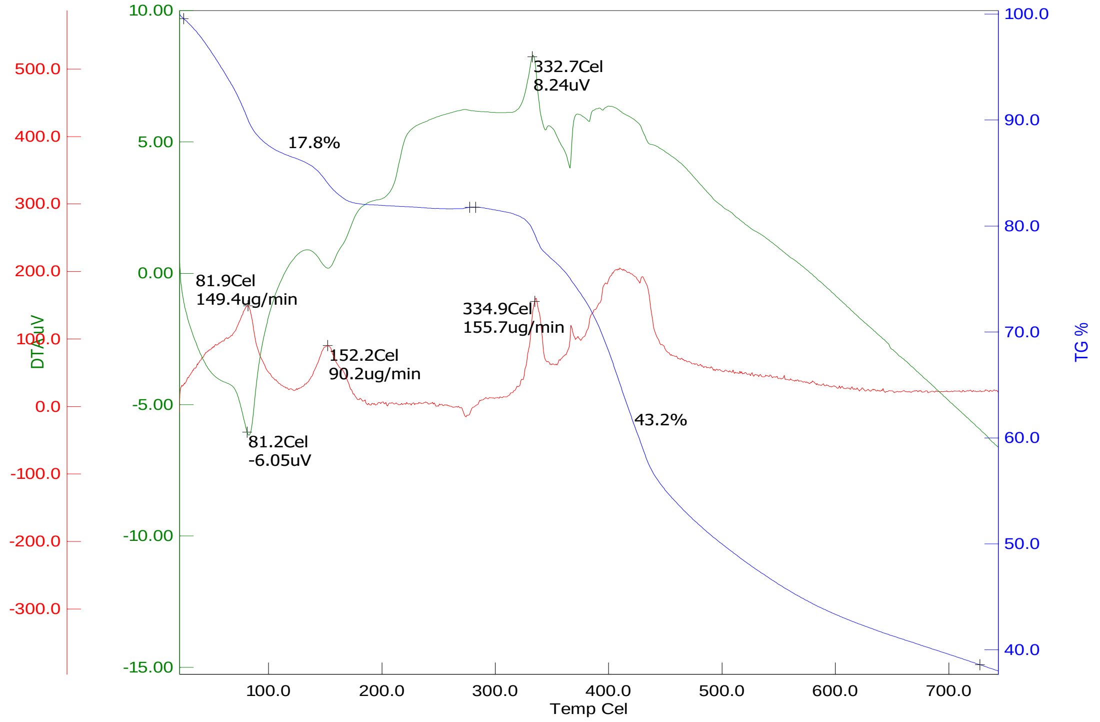

Figure 2b.11 Thermogravimetric curve for complex 2.

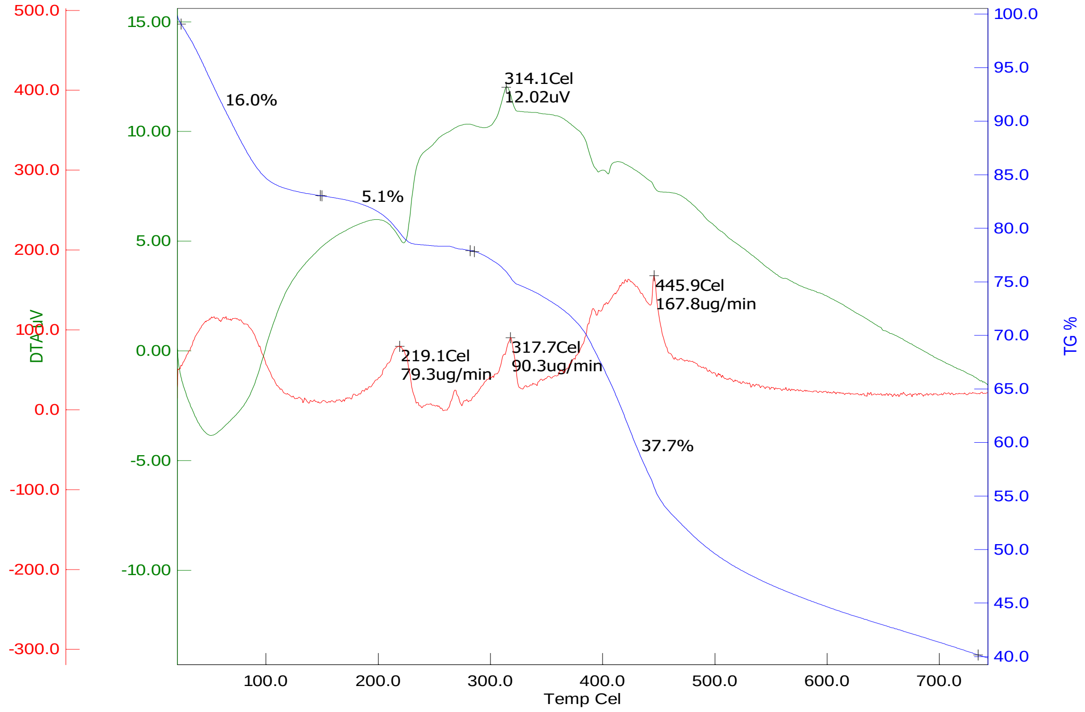

Figure 2b.12 Thermogravimetric curve for complex 3.

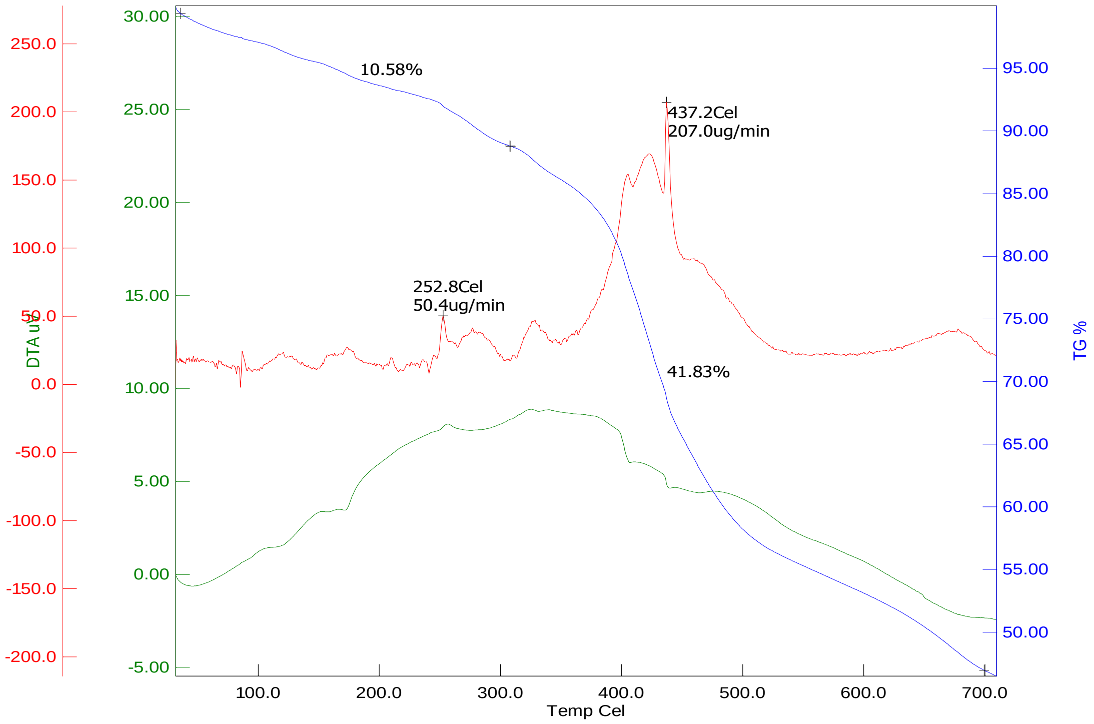

Figure 2b.13 Thermogravimetric curve for complex 4.

2b.3.4 Molar conductivity measurements

The molar conductivity (Λ_M) values for the solution of complexes 1, 2, 3, and 4 in DMF were determined to be 8, 11, 7, and 7 $cm^2\ mol^{-1}\ \Omega^{-1}$, respectively. These relatively low values provide evidence of non-electrolytic behaviour and the absence of charged ions within the coordination sphere [35].

2b.3.5 Single crystal X-ray diffraction analysis

Three-dimensional X-ray data and results presented are the of various data aggregation trials. The 8-coordination environment of uranyl nitrate underwent a unit-cell and geometry transformation to a 7-coordination environment in all four complexes. Subsequently, each complex adopts a monoclinic system with different space groups. The labelled thermal ellipsoid plots for all four complexes are depicted in Figure 2b.14. For comparison, Table 2b.2 presents all structural data along with refinement settings.

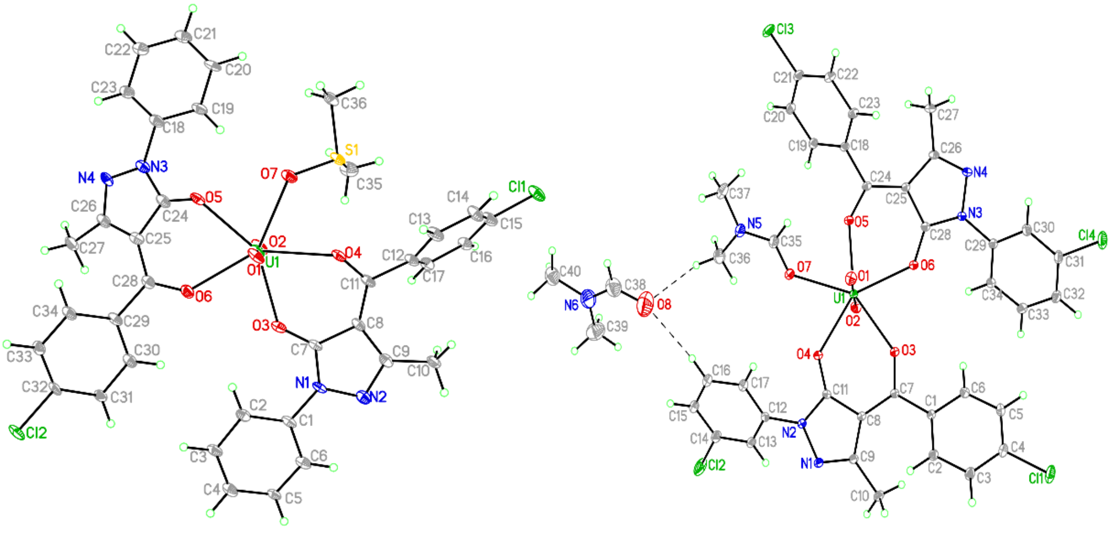

Complex 1

Complex 2

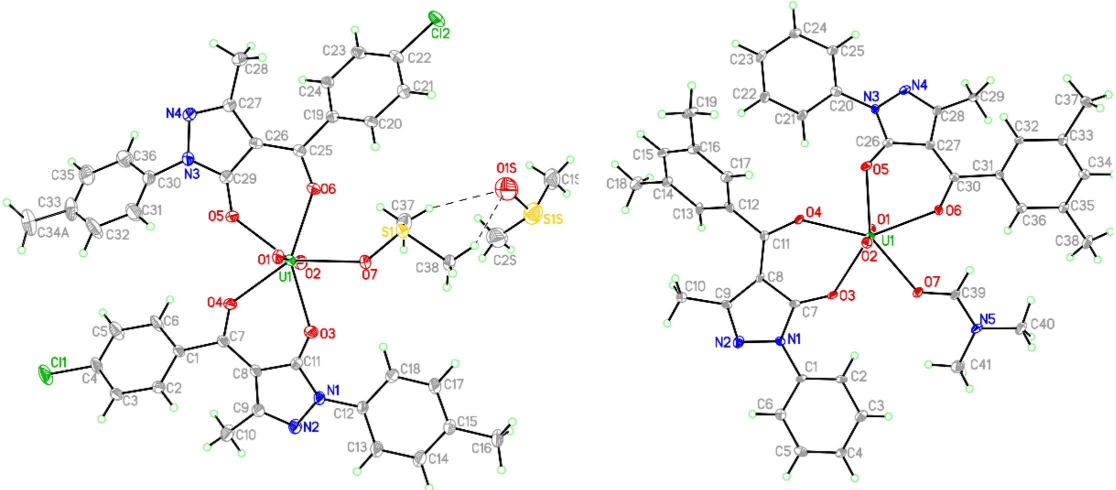

Complex 3

Complex 4

Figure 2b.14 Thermal ellipsoid plots of complexes 1, 2, 3, and 4 with 40% probability.

Table 2b.2 Structural data of complexes 1, 2, 3 and 4 with refinement parameters.

Code	Complex 1	Complex 2	Complex 3	Complex 4
CCDC number	2169240	2169241	2169242	2171275
Empirical formula	$C_{36}H_{30}Cl_2N_4O_7SU$	$C_{40}H_{36}Cl_4N_6O_8U$	$C_{40}H_{40}Cl_2N_4O_8S_2U$	$C_{41}H_{41}N_5O_7U$
Formula weight	971.63	1108.58	1077.81	953.82
Temperature	100(2) K	105(2) K	105(2) K	100(2) K
Wavelength	0.71073 Å	0.71073 Å	0.71073 Å	0.71073 Å
Crystal system	Monoclinic	Monoclinic	Monoclinic	Monoclinic
Space group	$P2_1/n$	$C2/c$	$C2/c$	$P\ 2_1/n$
Unit cell dimensions	a = 8.248(2) Å, b = 15.054(4) Å, c = 28.262(8) Å, α = 90°, β = 95.583(10)°, γ = 90°	a = 34.985(2) Å, b = 8.2450(4) Å, c = 32.1155(18) Å, α = 90°, β = 117.950(2)°, γ = 90°	a = 31.1775(9) Å, b = 17.7230(6) Å, c = 17.1850(5) Å, α = 90°, β = 119.040(2)°, γ = 90°	a = 16.0871(9) Å b = 9.4393(4) Å c = 25.7558(14) Å α= 90° β= 101.045(2)° γ = 90°
Volume	3492.5(16) Å^3	8183.2(8) Å^3	8301.9(5) Å^3	3838.6(3) Å^3
Z	4	8	8	4
Density (calculated)	1.848 Mg/m^3	1.800 Mg/m^3	1.725 Mg/m^3	1.650 Mg/m^3
Absorption coefficient	4.916 mm^{-1}	4.289 mm^{-1}	4.196 mm^{-1}	4.285 mm^{-1}
F(000)	1888	4336	4240	1880
Theta range for data collection	2.516 to 25.297°.	2.337 to 36.401°	2.168 to 28.282°.	2.303 to 28.280°
Index ranges	-	$-58 \leq h \leq 58$, $-13 \leq k \leq 13$, $-53 \leq l \leq 53$	$-41 \leq h \leq 41$, $-23 \leq k \leq 20$, $-22 \leq l \leq 22$	-
Reflection collected	6325	383858	54559	63493
Independent reflections	6325	19866 [*R(int)* = 0.0677]	10307 [*R(int)* = 0.1125]	9473 [R*(int)* = 0.0746]
Completeness to theta = 25.242°	100.0 %	99.7%	100.0 %	99.4%
Refinement method	Full-matrix least-squares on F^2	Full-matrix least-squares on F^2	Full-matrix least-squares on F^2	Full-matrix least-squares on F^2
Data / restraints / parameters	6325 / 450 / 465	19866 / 691 / 586	10307 / 158 / 573	9473 / 0 / 495
Goodness-of-fit on F_2	1.147	1.126	1.046	1.028
Final R indices [I>2sigma(I)]	$R_1 = 0.0755$, $wR_2 = 0.1531$	$R_1 = 0.0281$, $wR_2 = 0.0660$	$R_1 = 0.0450$, $wR_2 = 0.0987$	$R_1 = 0.0700$, $wR_2 = 0.1901$
R indices (all data)	$R_1 = 0.0893$, $wR_2 = 0.1593$	$R_1 = 0.0334$, $wR_2 = 0.0678$	$R_1 = 0.0776$, $wR_2 = 0.1133$	$R_1 = 0.0902$, $wR_2 = 0.2102$
Extinction coefficient	n/a	n/a	n/a	n/a
Largest diff. peak and hole	1.645 and −2.121 e.Å^{-3}	2.446 and −2.137 e.Å^{-3}	2.572 and −1.345 e.Å^{-3}	1.339 and −2.250 e.Å^{-3}

In complex 1, the composite crystal is formed by uranyl linking two anti-parallel L^1 ligands with one DMSO molecule serving as a solvent in the monoclinic $P2_1/n$ group. As depicted in Figure 2b.14, the two O-donors (O3 & O4), two O-donors (O5 & O6), and the O-atom (O7) of the DMSO molecule are all engaged in a distorted pentagonal bipyramidal geometry. The deviation from a regular pentagon's ideal 72° angle indicates distortion, which is attributed to the interaction between the two ligands bending towards the O-atom of the DMSO molecule. Consequently, the resulting bond angles for O(3)-U(1)-O(4), O(7)-U(1)-O(4), O(5)-U(1)-O(7), O(5)-U(1)-O(6), and O(3)-U(1)-O(6) are measured as 71.3°, 70.4°, 72.1°, 71.2°, and 75.1°, respectively (refer to Table 2b.3). Bond lengths were determined to be 1.762(7) Å, 1.756(7) Å, 2.337(8) Å, 2.366(8) Å, 2.393(7) Å, 2.411(8) Å, and 2.416(7) Å for U(1)-O(1), U(1)-O(2), U(1)-O(5), U(1)-O(3), U(1)-O(7), U(1)-O(4), and U(1)-O(6), respectively.

The monoclinic structure of complex 2 crystal was achieved through uranyl bonding between two L^2 ligands in an anti-configuration, with DMF serving as a solvent and a *C2/c* space group. The slight deviation from linearity in the uranyl bonding, with an angle of 179.11° for O(1)-U(1)-O(2), indicates an approaching distorted pentagonal bipyramidal arrangement. This distortion is further confirmed by bond angles measuring 74.20°, 71.82°, 70.06°, 72.54°, and 71.35° for O(6)-U(1)-O(3), O(6)-U(1)-O(5), O(5)-U(1)-O(7), O(4)-U(1)-O(7), and O(4)-U(1)-O(3), respectively. Bond lengths were determined to be 1.7722(15) Å, 1.7746(15) Å, 2.3312(14) Å, 2.3477(14) Å, 2.3666(14) Å, 2.3833(13) Å, and 2.4300(15) Å for the bonds U(1)-O(1), U(1)-O(2), U(1)-O(4), U(1)-O(6), U(1)-O(3), U(1)-O(5), and U(1)-O(7), respectively.

In the monoclinic crystal structure of complex 3, the unit-cell characteristics were consistent with the *C2/c* space group, featuring two L^3 ligands arranged in an anti-configuration, with DMSO serving as the solvent. The bond angle of O(1)-U(1)-O(2) measures 178.62° for the axial uranyl bond. Similar to complexes 1 and 2, the uranium center in complex 3 exhibits a distorted pentagonal bipyramidal geometry, with equatorial bond angles measuring 73.34°, 71.55°, 71.93°, 71.83°, and 71.41° for O(6)-U(1)-O(7), O(5)-U(1)-O(6), O(5)-U(1)-O(4), O(3)-U(1)-O(4), and O(3)-U(1)-O(7), respectively. Bond lengths were determined to be 1.759(4) Å, 1.763(4) Å, 2.347(4) Å, 2.348(4) Å, 2.375(4) Å, 2.385(4) Å, and 2.385(4) Å for U(1)-O(2), U(1)-O(1), U(1)-O(3), U(1)-O(5), U(1)-O(6), U(1)-O(4), and U(1)-O(7), respectively.

The crystal of complex 4 is formed through uranyl bonding with two L^4 ligands arranged in an anti-configuration, with one DMF molecule serving as the solvent, arranged in the monoclinic system with the $P2_1/n$ space group. The first and second L^4 ligands contribute two O-donors each (O3 & O4, O5 & O6), and the DMF molecule contributes an O-atom (O7). This arrangement adopts a distorted pentagonal bipyramidal geometry, as evidenced by certain bond angles and bond lengths outlined in Table 2b.3. The uranyl [O=U=O] binding is not perfectly linear, with the bond angle of O(2)-U(1)-O(1) measured at 178.1(3)°. Another indication of distortion is the variance in the angle between the axial and equatorial O-atoms. The deviation from the ideal bond angle of a pentagon (72°) is attributed to the stronger interaction of the two acylpyrazolones, causing them to bend towards the O-atom of the DMF moiety. Consequently, the resulting bond angles are measured as 71.51(18)°, 73.7(2)°, 72.10(19)°, 70.29(19)°, and 73.11(18)° for O(3)-U(1)-O(4), O(4)-U(1)-O(5), O(5)-U(1)-O(6), O(6)-U(1)-O(7), and O(7)-U(1)-O(3), respectively. Bond lengths for O(1)-U(1), U(1)-O(2), O(3)-U(1), U(1)-O(4), O(5)-U(1), U(1)-O(6), and O(7)-U(1) were determined to be 1.780(6) Å, 1.761(6) Å, 2.373(6) Å, 2.393(6) Å, 2.312(6) Å, 2.415(5) Å, and 2.430(5) Å, respectively.

The covalency order among complexes 1-4 was found to be influenced by several factors, including stretching frequencies, average bond lengths of axial uranyl bonds, average bond lengths on the pentagonal equatorial plane, solvent coordination on the fifth site of a pentagonal plane, and the type of aryl group on the nitrogen of the pyrazolone ring. In contrast to complexes 1 and 3, complex 2 exhibited a longer U(1)-O(7) bond, resulting in a reduction in the alternative U-O overall bond order and an increased covalent nature. A similar decrease in covalency was observed in complexes 1 and 3 for the same reason. Conversely, the methyl groups attached to the benzoyl group had a significant effect on the U(1)-O(7) bond length (2.430(5) Å) in complex 4. As commonly observed in uranyl acylpyrazolone complexes [36,37], the U-O bond lengths for the acyl O-atoms were notably higher than those for the O-atoms on the pyrazolone ring. Additionally, across all four complexes, the axial uranyl U-O bonds exhibited shorter bond lengths compared to the corresponding equatorial U-O bonds due to a double bond character.

Table 2b.3 Bond parameters for complexes 1-4.

complex 1							
Atoms	**Bond lengths**	**Atoms**	**Bond lengths**	**Atoms**	**Bond angles**	**Atoms**	**Bond angles**
U(1)-O(2)	1.756(7)	O(3)-C(7)	1.280(14)	O(2)-U(1)-O(1)	178.8(4)	O(3)-U(1)-O(4)	71.3(3)
U(1)-O(1)	1.762(7)	O(4)-C(11)	1.266(14)	O(2)-U(1)-O(5)	91.8(4)	O(7)-U(1)-O(4)	70.4(3)
U(1)-O(5)	2.337(8)	O(5)-C(24)	1.252(14)	O(1)-U(1)-O(5)	89.3(3)	O(2)-U(1)-O(6)	90.0(3)
U(1)-O(3)	2.366(8)	O(6)-C(28)	1.262(13)	O(2)-U(1)-O(3)	88.0(3)	O(1)-U(1)-O(6)	90.1(3)
U(1)-O(7)	2.393(7)	N(1)-C(7)	1.346(14)	O(1)-U(1)-O(3)	90.9(3)	O(5)-U(1)-O(6)	71.2(3)
U(1)-O(4)	2.411(8)	N(1)-C(1)	1.394(14)	O(5)-U(1)-O(3)	146.4(3)	O(3)-U(1)-O(6)	75.1(3)
U(1)-O(6)	2.416(7)	N(1)-N(2)	1.418(13)	O(2)-U(1)-O(7)	88.0(3)	O(7)-U(1)-O(6)	143.2(3)
Cl(1)-C(15)	1.734(11)	N(2)-C(9)	1.322(14)	O(1)-U(1)-O(7)	92.6(3)	O(4)-U(1)-O(6)	146.4(3)
Cl(2)-C(32)	1.756(11)	N(3)-C(24)	1.357(15)	O(5)-U(1)-O(7)	72.1(3)	C(7)-O(3)-U(1)	132.4(6)
O(3)-C(7)	1.280(14)	N(3)-N(4)	1.405(13)	O(3)-U(1)-O(7)	141.4(3)	C(11)-O(4)-U(1)	136.5(7)
O(4)-C(11)	1.266(14)	N(3)-C(18)	1.450(14)	O(2)-U(1)-O(4)	90.7(3)	C(24)-O(5)-U(1)	126.1(8)
O(5)-C(24)	1.252(14)	N(4)-C(26)	1.294(15)	O(1)-U(1)-O(4)	88.6(3)	C(28)-O(6)-U(1)	135.9(7)
O(6)-C(28)	1.262(13)	S(1)-O(7)	1.533(8)	O(5)-U(1)-O(4)	142.3(2)	O(6)-C(28)-C(25)	121.8(10)
complex 2							
Atoms	**Bond lengths**	**Atoms**	**Bond lengths**	**Atoms**	**Bond angles**	**Atoms**	**Bond angles**
U(1)-O(1)	1.7722(15)	O(5)-C(24)	1.275(2)	O(1)-U(1)-O(2)	179.11(8)	O(6)-U(1)-O(5)	71.82(5)
U(1)-O(2)	1.7746(15)	O(6)-C(28)	1.275(2)	O(1)-U(1)-O(4)	89.82(7)	O(3)-U(1)-O(5)	145.99(5)
U(1)-O(4)	2.3312(14)	N(1)-C(9)	1.315(2)	O(2)-U(1)-O(4)	90.25(6)	O(1)-U(1)-O(7)	88.95(7)
U(1)-O(6)	2.3477(14)	N(1)-N(2)	1.397(2)	O(1)-U(1)-O(6)	89.05(6)	O(2)-U(1)-O(7)	90.24(7)
U(1)-O(3)	2.3666(14)	N(2)-C(11)	1.360(2)	O(2)-U(1)-O(6)	91.38(6)	O(4)-U(1)-O(7)	72.54(5)
U(1)-O(5)	2.3833(13)	N(2)-C(12)	1.414(2)	O(4)-U(1)-O(6)	145.51(5)	O(6)-U(1)-O(7)	141.88(5)
U(1)-O(7)	2.4300(15)	N(3)-C(28)	1.357(2)	O(1)-U(1)-O(3)	90.84(7)	O(3)-U(1)-O(7)	143.89(5)
Cl(1)-C(4)	1.7384(19)	N(3)-N(4)	1.397(2)	O(2)-U(1)-O(3)	90.02(7)	O(5)-U(1)-O(7)	70.06(5)
Cl(2)-C(14)	1.726(2)	N(3)-C(29)	1.415(2)	O(4)-U(1)-O(3)	71.35(5)	C(7)-O(3)-U(1)	140.06(13)
Cl(3)-C(21)	1.7309(18)	N(4)-C(26)	1.316(2)	O(6)-U(1)-O(3)	74.20(5)	C(11)-O(4)-U(1)	128.03(12)
Cl(4)-C(31)	1.736(2)	O(7)-C(35)	1.243(2)	O(1)-U(1)-O(5)	87.23(6)	C(24)-O(5)-U(1)	136.44(12)
O(3)-C(7)	1.272(2)	O(8)-C(38)	1.233(3)	O(2)-U(1)-O(5)	92.17(6)	C(28)-O(6)-U(1)	132.14(12)
O(4)-C(11)	1.277(2)	C(38)-N(6)	1.306(3)	O(4)-U(1)-O(5)	142.53(5)	O(6)-C(28)-C(25)	130.59(17)
complex 3							
Atoms	**Bond lengths**	**Atoms**	**Bond lengths**	**Atoms**	**Bond angles**	**Atoms**	**Bond angles**
U(1)-O(2)	1.759(4)	N(1)-C(11)	1.351(7)	O(2)-U(1)-O(1)	178.62(18)	O(5)-U(1)-O(4)	71.93(13)
U(1)-O(1)	1.763(4)	N(1)-N(2)	1.396(6)	O(2)-U(1)-O(3)	92.16(18)	O(6)-U(1)-O(4)	143.42(14)
U(1)-O(3)	2.347(4)	N(1)-C(12)	1.416(7)	O(1)-U(1)-O(3)	89.15(17)	O(2)-U(1)-O(7)	90.76(18)
U(1)-O(5)	2.348(4)	N(2)-C(9)	1.306(7)	O(2)-U(1)-O(5)	89.85(17)	O(1)-U(1)-O(7)	90.05(16)
U(1)-O(6)	2.375(4)	N(3)-C(29)	1.343(7)	O(1)-U(1)-O(5)	88.85(16)	O(3)-U(1)-O(7)	71.41(13)
U(1)-O(4)	2.385(4)	N(3)-N(4)	1.405(7)	O(3)-U(1)-O(5)	143.66(13)	O(5)-U(1)-O(7)	144.86(13)
U(1)-O(7)	2.385(4)	N(3)-C(30)	1.419(7)	O(2)-U(1)-O(6)	89.00(17)	O(6)-U(1)-O(7)	73.34(13)
Cl(1)-C(4)	1.733(6)	N(4)-C(27)	1.305(7)	O(1)-U(1)-O(6)	90.17(17)	O(4)-U(1)-O(7)	143.21(14)
Cl(2)-C(22)	1.732(6)	S(1S)-O(1S)	1.527(5)	O(3)-U(1)-O(6)	144.74(13)	O(3)-C(11)-N(1)	124.0(5)
O(3)-C(11)	1.276(7)	S(1T)-O(1T)	1.527(5)	O(5)-U(1)-O(6)	71.55(13)	O(3)-C(11)-C(8)	129.3(5)
O(4)-C(7)	1.264(7)	S(1T)-C(1T)	1.746(7)	O(2)-U(1)-O(4)	88.92(19)	O(5)-C(29)-N(3)	123.2(5)
O(5)-C(29)	1.272(7)	S(1)-C(38)	1.767(6)	O(1)-U(1)-O(4)	91.10(18)	O(5)-C(29)-C(26)	130.2(5)
O(6)-C(25)	1.281(7)	S(1S)-C(2S)	1.766(6)	O(3)-U(1)-O(4)	71.83(13)	O(7)-S(1)-C(37)	106.6(3)
complex 4							
Atoms	**Bond lengths**	**Atoms**	**Bond lengths**	**Atoms**	**Bond angles**	**Atoms**	**Bond angles**
U(1)-O(2)	1.761(6)	O(6)-C(30)	1.276(9)	O(2)-U(1)-O(1)	178.1(3)	O(3)-U(1)-O(6)	141.74(18)
U(1)-O(1)	1.780(6)	O(7)-C(39)	1.237(10)	O(2)-U(1)-O(5)	91.4(2)	O(4)-U(1)-O(6)	145.75(19)
U(1)-O(5)	2.312(6)	N(1)-C(7)	1.357(10)	O(1)-U(1)-O(5)	87.1(2)	O(2)-U(1)-O(7)	89.0(2)
U(1)-O(3)	2.373(6)	C(3)-C(4)	1.425(13)	O(2)-U(1)-O(3)	95.0(2)	O(1)-U(1)-O(7)	92.9(2)
U(1)-O(4)	2.393(6)	C(4)-C(5)	1.376(12)	O(1)-U(1)-O(3)	85.6(2)	O(5)-U(1)-O(7)	142.3(2)
U(1)-O(6)	2.415(5)	C(5)-C(6)	1.383(12)	O(5)-U(1)-O(3)	144.25(19)	O(3)-U(1)-O(7)	73.11(18)
U(1)-O(7)	2.430(5)	C(7)-C(8)	1.448(10)	O(2)-U(1)-O(4)	87.5(2)	O(4)-U(1)-O(7)	144.0(2)
O(3)-C(7)	1.278(10)	C(8)-C(11)	1.410(11)	O(1)-U(1)-O(4)	91.1(2)	O(6)-U(1)-O(7)	70.29(19)
O(4)-C(11)	1.279(9)	C(8)-C(9)	1.423(11)	O(5)-U(1)-O(4)	73.7(2)	C(7)-O(3)-U(1)	133.6(5)
O(5)-C(26)	1.276(11)	C(9)-C(10)	1.500(12)	O(3)-U(1)-O(4)	71.51(18)	C(11)-O(4)-U(1)	141.2(5)
C(11)-C(12)	1.483(11)	N(1)-C(1)	1.427(9)	O(2)-U(1)-O(6)	95.1(2)	C(26)-O(5)-U(1)	123.9(5)
C(12)-C(17)	1.400(11)	N(2)-C(9)	1.315(11)	O(1)-U(1)-O(6)	85.4(2)	C(30)-O(6)-U(1)	134.6(5)

2b.3.6 DFT computational analysis

The DFT calculations conclusively support the pentagonal bipyramidal geometry. As frontier orbitals play a pivotal role in determining energy and chemical behaviour, their examination yields initial insights [21,38–40]. The structures were optimised for complexes 1, 2, 3, and 4, yielding electronic energy values of −107, −123.7, −109.1, and −77.946 keV, respectively. Figure 2b.15 illustrates the theoretically idealized geometries of the four complexes.

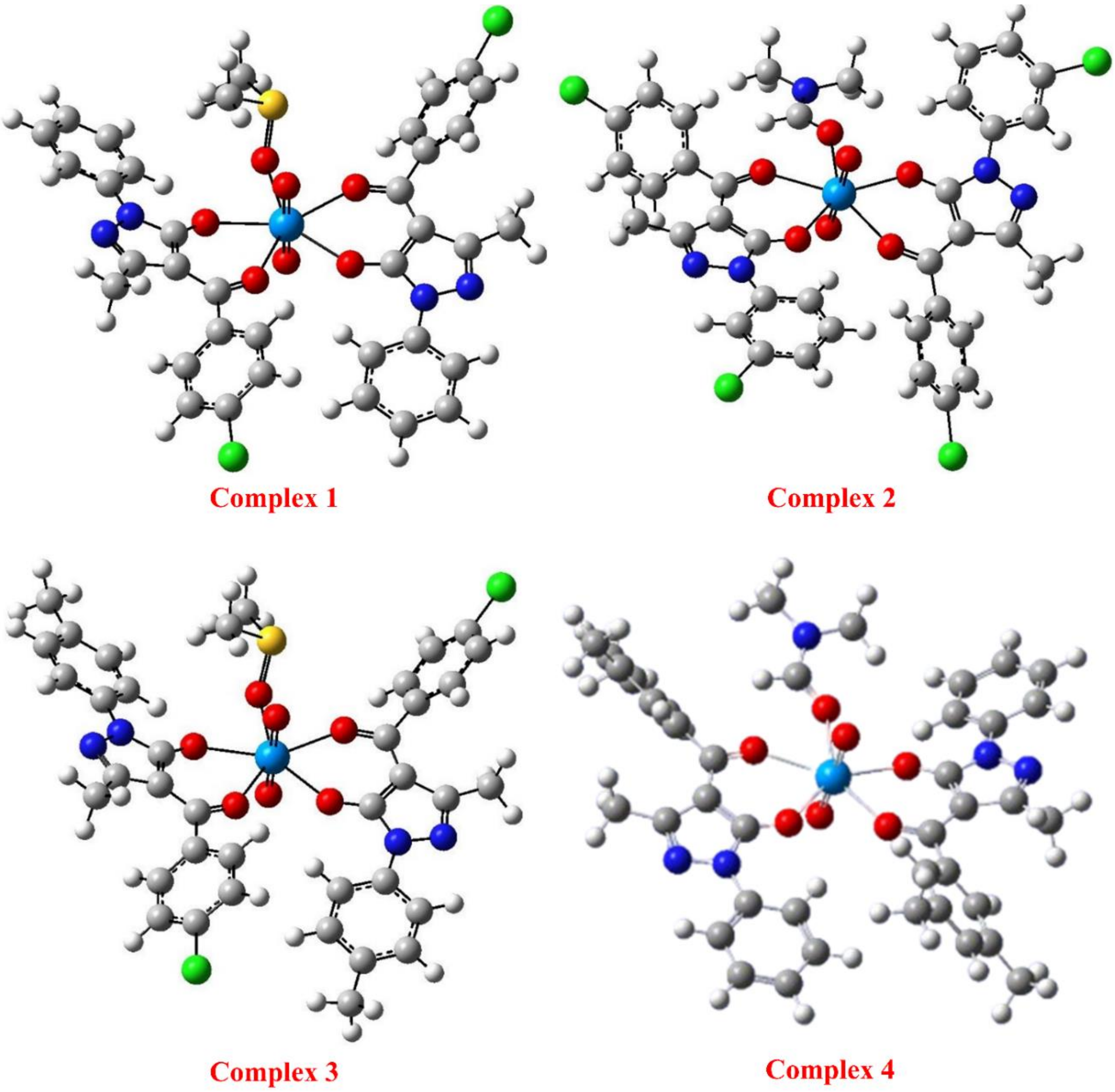

Complex 1

Complex 2

Complex 3

Complex 4

Figure 2b.15 DFT optimized geometries for complexes 1-4.

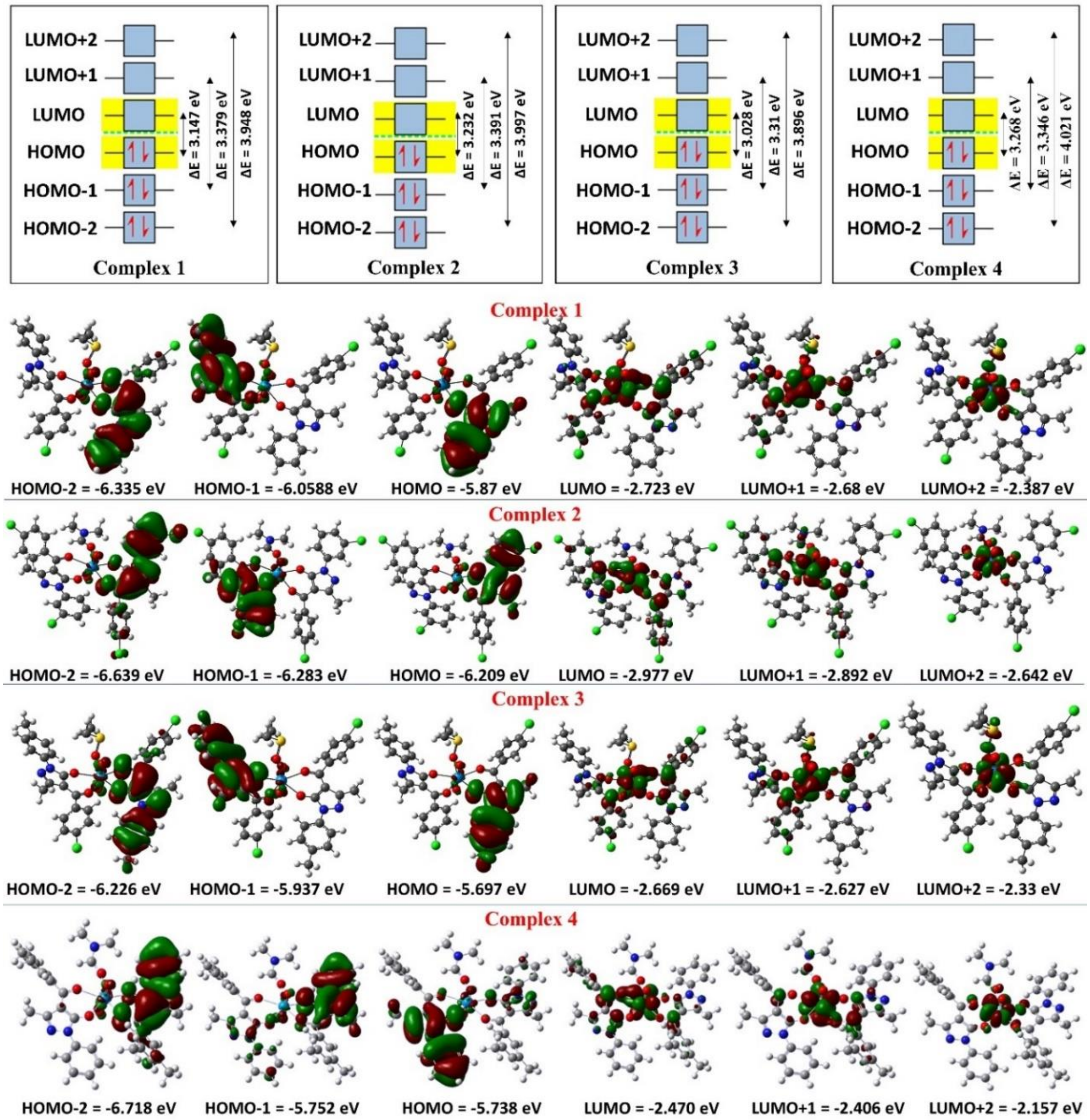

Figure 2b.16 HOMO-LUMO frontier orbitals with an energy diagram for complexes 1-4.

As depicted in Figure 2b.16, the majority of Highest Occupied Molecular Orbitals (HOMOs) are localized around the ligand at levels HOMO−2, HOMO−1, and HOMO, with energy levels of −6.335, −6.0588, and −5.87 eV for complex 1, −6.639, −6.283, and −6.209 eV for complex 2, −6.226, −5.937, and −5.697 eV for complex 3, and −6.178, −5.752, and −5.738 eV for complex 4, respectively. Similarly, the majority of Lowest Unoccupied Molecular Orbitals (LUMOs) are situated in the vicinity of the metal center at the LUMO, LUMO+1, and LUMO+2, with energy levels of −2.723, −2.68, and −2.387 eV for complex 1, −2.977, −2.892, and −2.642 eV for complex 2, −2.669, −2.627, and −2.33 eV for complex 3, and −2.387, −2.68, and −2.723 eV for complex 4, respectively.

The energy differences between HOMO and LUMO ($\Delta E_{HOMO-LUMO}$), HOMO−1 and LUMO+1 ($\Delta E_{HOMO-1-LUMO+1}$), and HOMO−2 and LUMO+2 ($\Delta E_{HOMO-2-LUMO+2}$) are 3.147, 3.379, and 3.948 eV for complex 1, 3.232, 3.391, and 3.997 eV for complex 2, 3.028, 3.31, and 3.896 eV for complex 3, and 4.021, 3.346, and 3.268 eV for complex 4, respectively. These values can be indicative of chemical stability. The diamagnetic properties of the complexes can be explained by the presence of paired electrons in all HOMOs. Furthermore, the higher stability of complex 2 is evident through its higher ΔE values compared to complexes 1 and 3, as the energy required to promote the electron is higher in complex 2. Additionally, the effect of electro-releasing methyl groups attached to the benzoyl ring is observed from the higher $\Delta E_{HOMO-LUMO}$ values of complex 4. Global metrics, as shown in Table 2b.4, offer a comprehensive understanding of the characteristics of the complexes.

Table 2b.4 Global parameters for complexes 1-4 (in eV).

Properties of Complex	**Mathematical Formula**	**Complex 1**	**Complex 2**	**Complex 3**	**Complex 4**
E_{HOMO}	E_{HOMO}	–5.87	–6.209	–5.697	–5.738
E_{LUMO}	E_{LUMO}	–2.723	–2.977	–2.669	–2.470
ΔE	$\Delta E = E_{LUMO} - E_{HOMO}$	3.147	3.232	3.028	3.268
Ionization potential (IP)	$IP = -E_{HOMO}$	5.87	6.209	5.697	5.738
Chemical Potential (μ)	$\mu = ½ (E_{Homo} + E_{Lumo})$	–4.2965	–4.593	–4.183	–4.104
Electron affinity (EA)	$EA = -E_{LUMO}$	2.723	2.977	2.669	2.470
Electronegativity (EN)	$EN = -½ (E_{Homo} + E_{Lumo})$	4.2965	4.593	4.183	4.104
Global Hardness (Ƞ)	$\eta = -½ (E_{Homo} - E_{Lumo})$	1.5735	1.616	1.514	1.634
Softness (S)	$S = 1/2\eta$	0.3177	0.3094	0.3302	0.306
Electrophilicity index (ω)	$\omega = \mu^2/2\eta$	5.8659	6.5271	5.7785	5.154

Theoretical vibrations can be employed to assess the gradient of covalent nature based on frequency values. Essential theoretical vibrations, juxtaposed with actual FTIR spectrum values, are outlined in Table 2b.5. As previously elucidated, the relative impact of uranyl's asymmetric and symmetric vibrations confirms the covalency order, with complex 2 exhibiting a higher covalent character than the other complexes, while complexes 1 and 3 demonstrate relatively similar covalent characteristics. The theoretical FTIR spectra are depicted in Figures 2b.17-2b.20. Table 2b.6 presents crucial theoretical bond parameters that align with the observed values for further analysis.

Table 2b.5 Comparing theoretical and actual vibrational data for complexes 1-4.

Type of Frequency (in cm^{-1} units)	**Complex 1**		**Complex 2**		**Complex 3**		**Complex 4**	
	Theoretical	Practical	Theoretical	Practical	Theoretical	Practical	Theoretical	Practical
$\nu_{s(C=O)}$ benzoyl	1583	1577	1603	1591	1600	1591	1635	1618
$\nu_{(C=O)}$ acyl	1559	1557	1563	1557	1559	1558	1576	1602
Cyclic $\nu_{(C=N)}$	1404	1472	1482	1471	1429	1436	1474	1480
C-H in plane deformation	1097	1013	1096	1089	1094	1089	1082	1062
$\nu_{as(U=O)}$	917	920	884	863	916	912	927	925
$\nu_{s(U=O)}$	841	833	840	778	829	823	847	808

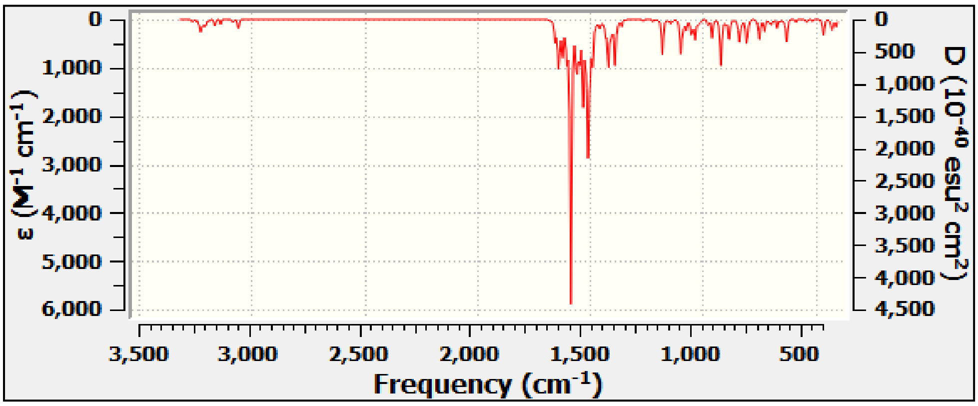

Figure 2b.17 FTIR spectrum of complex 1 through computational analysis.

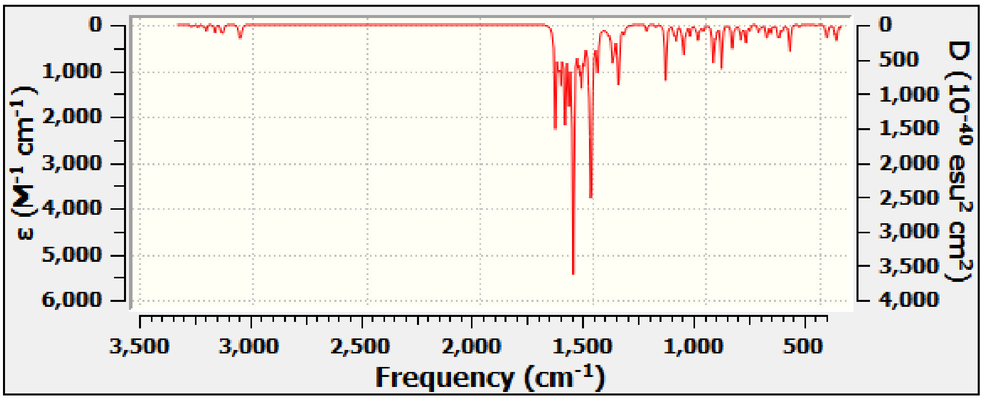

Figure 2b.18 FTIR spectrum of complex 2 through computational analysis.

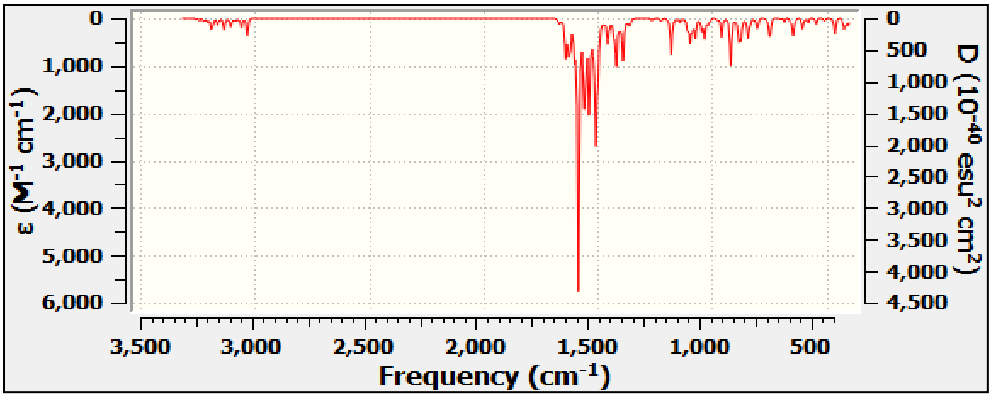

Figure 2b.19 FTIR spectrum of complex 3 through computational analysis.

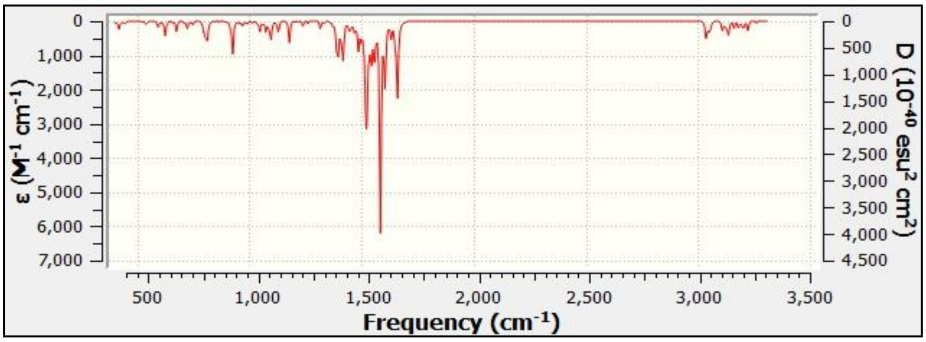

Figure 2b.20 FTIR spectrum of complex 4 through computational analysis.

Table 2b.6 Practical and theoretical bond parameters comparison for complexes 1-4.

Atoms numbering as in Figure 2b.14	Practical Bond lengths	Theoretical Bond lengths	Atoms numbering as in Figure 2b.14	Practical Bond angles	Theoretical Bond angles
Complex 1					
U(1)-O(1)	1.762(7)	1.81052	O(2)-U(1)-O(1)	178.8(4)	177.56383
U(1)-O(5)	2.337(8)	2.37473	O(1)-U(1)-O(7)	92.6(3)	86.18490
U(1)-O(6)	2.416(7)	2.40007	O(2)-U(1)-O(3)	88.0(3)	91.38749
U(1)-O(2)	1.756(7)	1.79245	O(5)-U(1)-O(7)	72.1(3)	72.62033
U(1)-O(3)	2.366(8)	2.35395	O(5)-U(1)-O(6)	71.2(3)	69.60423
U(1)-O(4)	2.411(8)	2.40833	O(3)-U(1)-O(6)	75.1(3)	75.40828
U(1)-O(7)	2.393(7)	2.37527	O(3)-U(1)-O(4)	71.3(3)	70.10830
			O(7)-U(1)-O(4)	70.4(3)	72.60965
Complex 2					
Atoms numbering as in Figure 2b.14	**Practical Bond lengths**	**Theoretical Bond lengths**	**Atoms numbering as in Figure 2b.14**	**Practical Bond angles**	**Theoretical Bond angles**
U(1)-O(1)	1.7722(15)	1.79267	O(1)-U(1)-O(2)	179.11(8)	178.03015
U(1)-O(5)	2.3833(13)	2.43056	O(1)-U(1)-O(7)	88.95(7)	92.46929
U(1)-O(6)	2.3477(14)	2.43472	O(2)-U(1)-O(7)	90.24(7)	86.15223
U(1)-O(2)	1.7746(15)	2.36230	O(5)-U(1)-O(7)	70.06(5)	70.08910
U(1)-O(3)	2.3666(14)	1.79469	O(6)-U(1)-O(5)	71.82(5)	70.26160
U(1)-O(4)	2.3312(14)	2.37222	O(6)-U(1)-O(3)	74.20(5)	77.21527
U(1)-O(7)	2.4300(15)	2.36815	O(4)-U(1)-O(3)	71.35(5)	70.38770
			O(4)-U(1)-O(7)	72.54(5)	72.63012
Complex 3					
Atoms numbering as in Figure 2b.14	**Practical Bond lengths**	**Theoretical Bond lengths**	**Atoms numbering as in Figure 2b.14**	**Practical Bond angles**	**Theoretical Bond angles**
U(1)-O(1)	1.763(4)	1.81085	O(2)-U(1)-O(1)	178.62(18)	177.48009
U(1)-O(7)	2.385(4)	2.37591	O(1)-U(1)-O(7)	90.05(16)	86.12653
U(1)-O(3)	2.347(4)	2.37660	O(2)-U(1)-O(7)	90.76(18)	91.35968
U(1)-O(4)	2.385(4)	2.39776	O(3)-U(1)-O(7)	71.41(13)	72.57717
U(1)-O(2)	1.759(4)	1.79277	O(3)-U(1)-O(4)	71.83(13)	69.60588
U(1)-O(5)	2.348(4)	2.35173	O(5)-U(1)-O(4)	71.93(13)	75.33490
O(5)-C(6)	2.375(4)	2.40816	O(5)-U(1)-O(6)	71.55(13)	70.13616
			O(6)-U(1)-O(7)	73.34(13)	72.68836
Complex 4					
Atoms numbering as in Figure 2b.14	**Practical Bond lengths**	**Theoretical Bond lengths**	**Atoms numbering as in Figure 2b.14**	**Practical Bond angles**	**Theoretical Bond angles**
U(1)-O(2)	1.761(6)	1.79696	O(2)-U(1)-O(1)	178.1(3)	177.90
U(1)-O(1)	1.780(6)	1.79406	O(2)-U(1)-O(5)	91.4(2)	91.37
U(1)-O(5)	2.312(6)	2.34650	O(1)-U(1)-O(5)	87.1(2)	89.21
U(1)-O(3)	2.373(6)	2.36619	O(2)-U(1)-O(3)	95.0(2)	92.70
U(1)-O(4)	2.393(6)	2.36757	O(1)-U(1)-O(3)	85.6(2)	87.94
U(1)-O(6)	2.415(5)	2.43766	O(5)-U(1)-O(3)	144.25(19)	145.99
U(1)-O(7)	2.430(5)	2.44029	O(2)-U(1)-O(4)	87.5(2)	86.43
O(3)-C(7)	1.278(10)	1.29659	O(1)-U(1)-O(4)	91.1(2)	95.66

2b.3.7 Hirshfeld surface area analysis

Using the Crystal Explorer 17.5 program, the donor-acceptor interaction sites and intermolecular contacts for all four complexes can be visualized (refer to Figures 2b.21-2b.24). The absence of prominent red spots indicates the lack of hydrogen bonds. However, as depicted in Figures 2b.21-2b.24, the weaker red markings on the d_{norm} surface suggest better proximity to neighbouring moieties or shorter contacts between halogen bonds. Additionally, alongside shorter non-covalent contacts, the red-blue regions in d_{norm} and the curved portions of the curvedness plot surrounding the aromatic rings suggest stacking, thereby enhancing the stability of the crystal lattice. The packing probability of complexes can be assessed using percentage statistics for atom-all and all-atom contacts. Notably, there are no U-all, U-U, or all-U connections in any of the four complexes, indicating that uranium does not form secondary interactions with the surrounding atoms of the molecules. Significant hydrogen interactions have been observed for all four complexes, with H-all interactions accounting for 58%, 51%, 62%, and 71% for complexes 1-4, respectively, and All-H interactions accounting for 65%, 60%, 69%, and 75% for complexes 1-4, respectively, as illustrated in Figure 2b.25. Figures 2b.26-2b.29 present 2D FP plots corresponding to all such interactions.

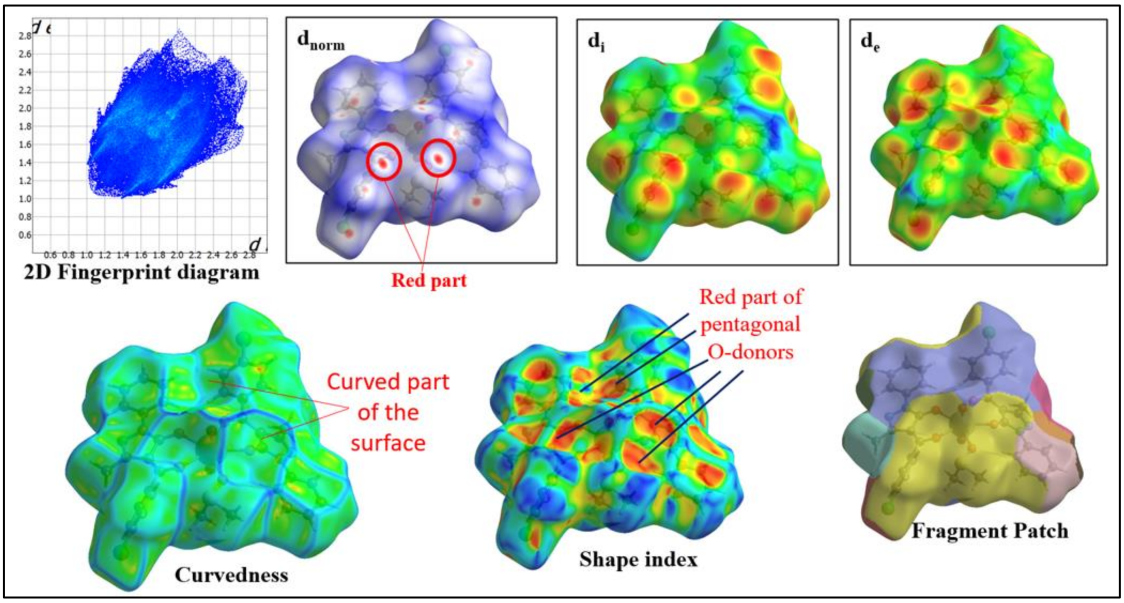

Figure 2b.21 The molecular HS for complex 1.

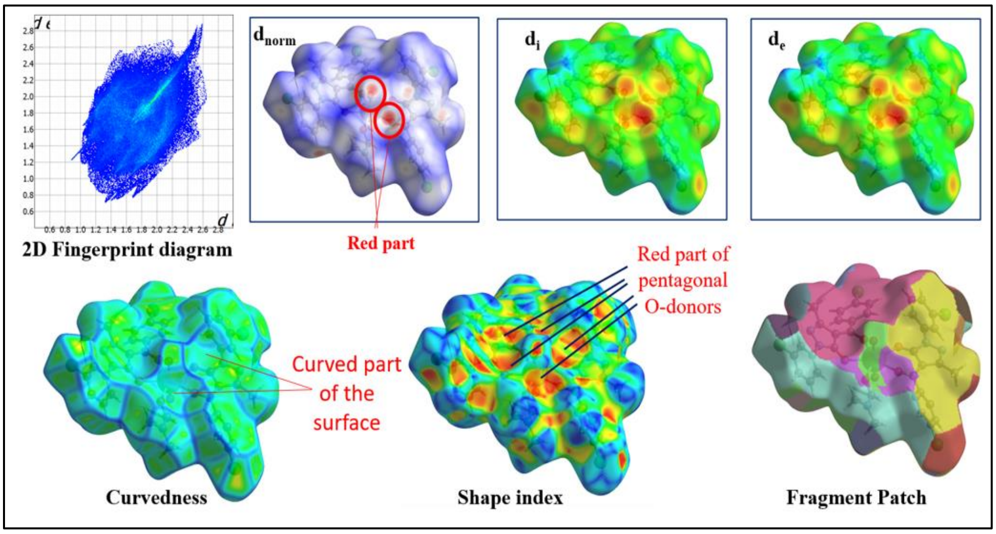

Figure 2b.22 The molecular HS for complex 2.

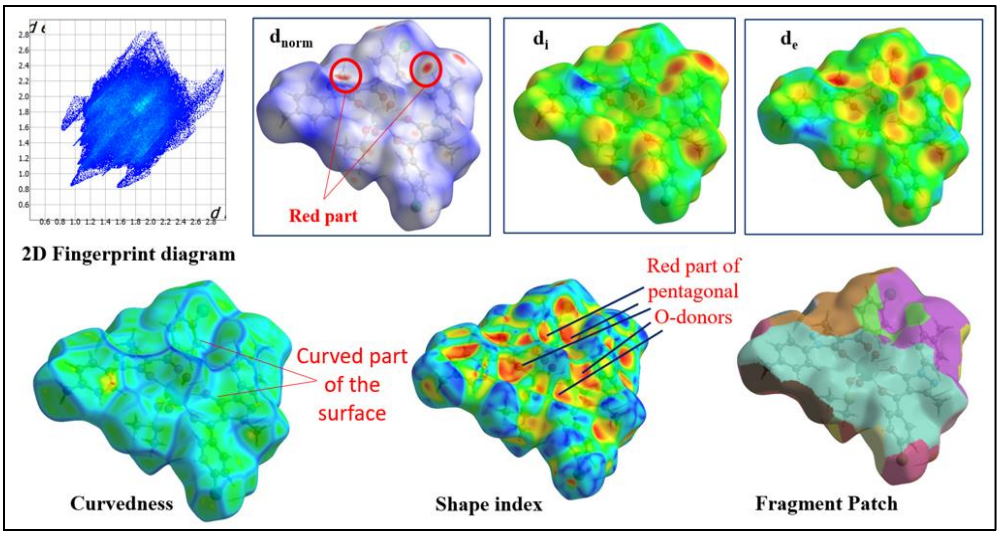

Figure 2b.23 The molecular HS for complex 3.

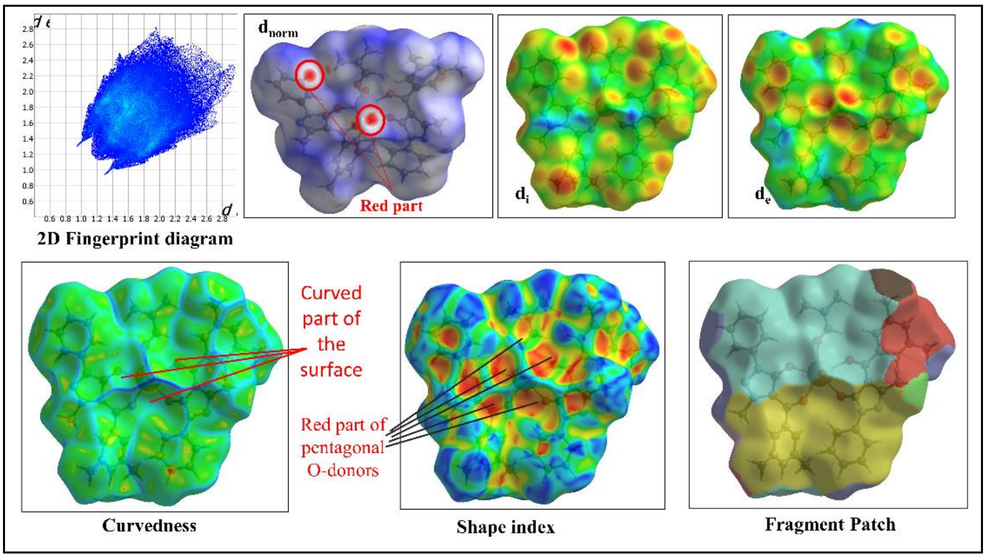

Figure 2b.24 The molecular HS for complex 4.

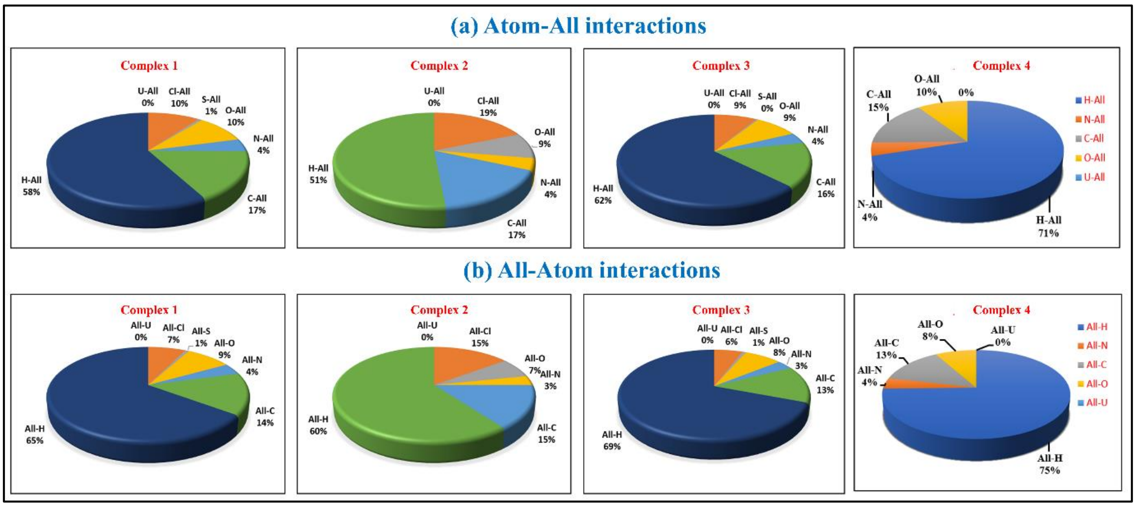

Figure 2b.25 The percentage Hirshfeld surface interactions for complexes 1-4.

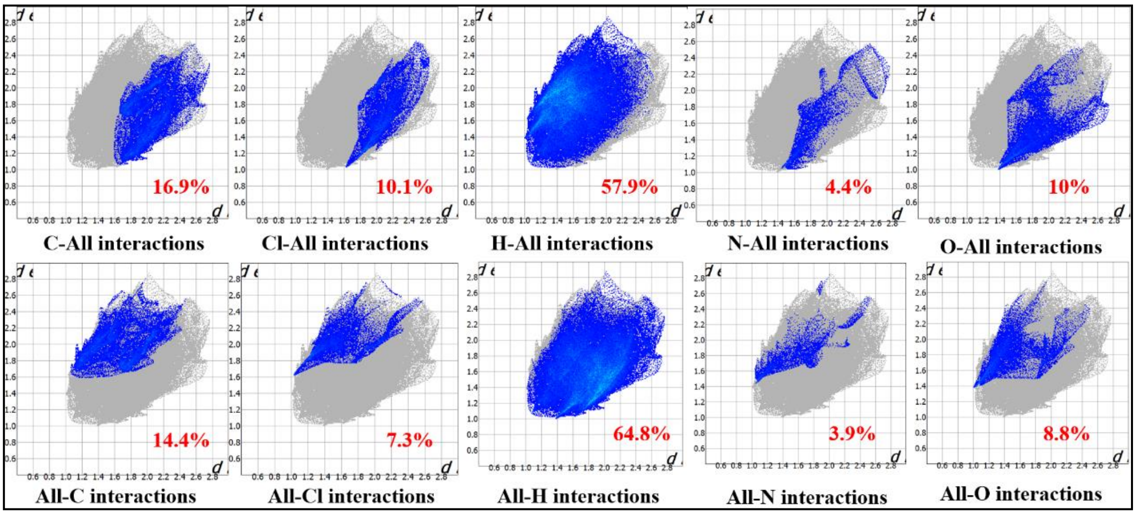

Figure 2b.26 Two-dimensional fingerprint plots for complex 1.

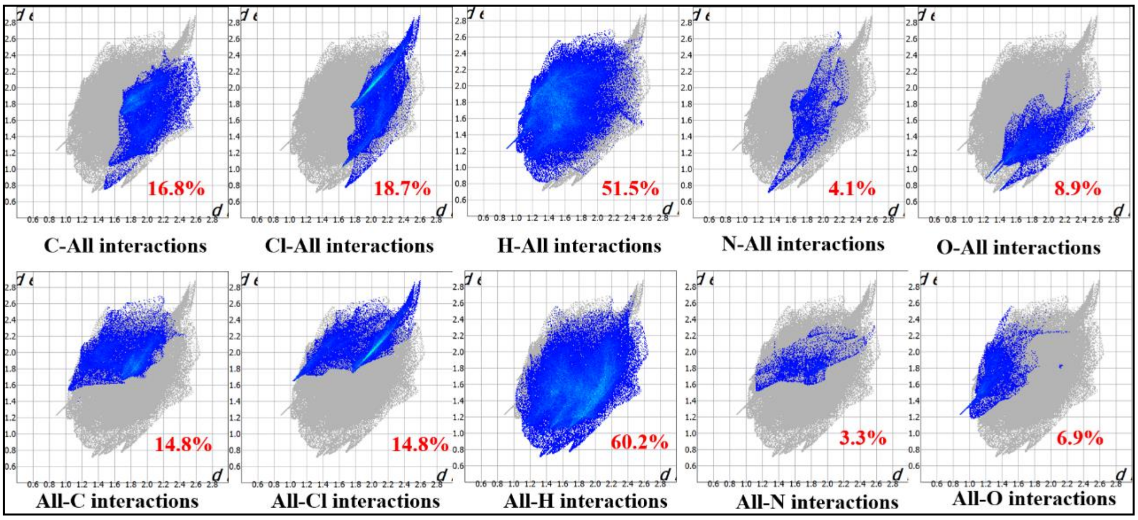

Figure 2b.27 Two-dimensional fingerprint plots for complex 2.

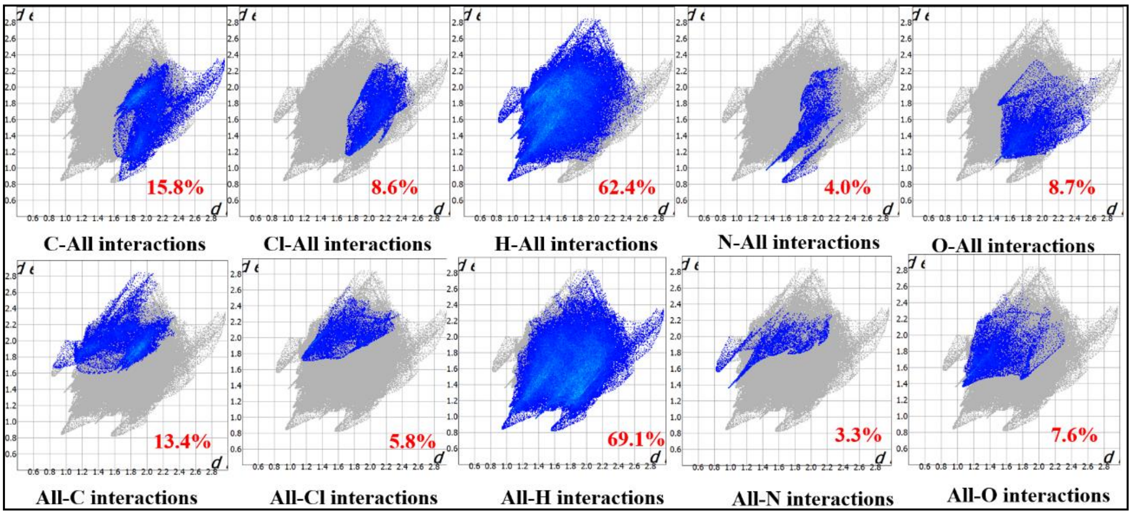

Figure 2b.28 Two-dimensional fingerprint plots for complex 3.

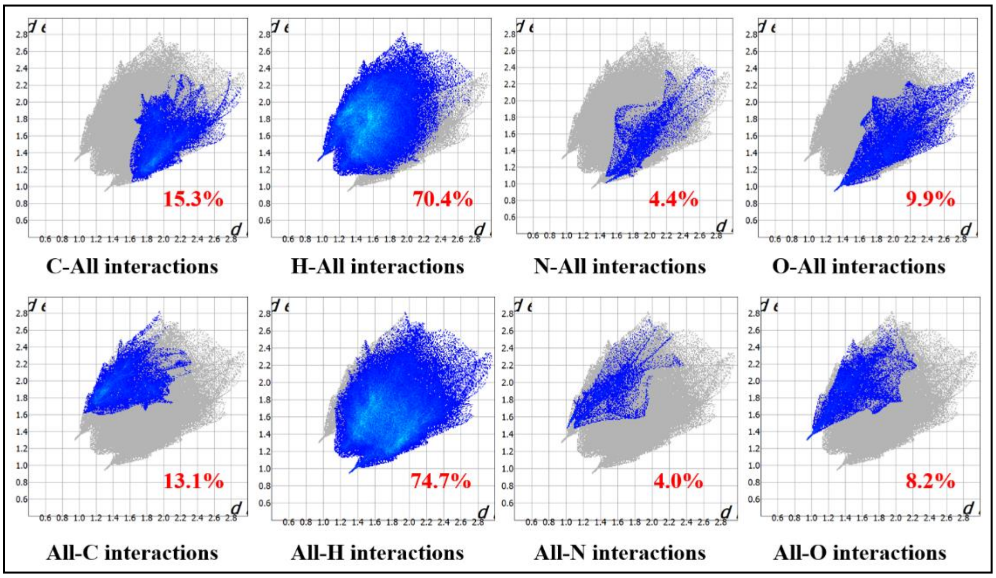

Figure 2b.29 Two-dimensional fingerprint plots for complex 4.

2b.3.8 Electronic spectral analysis

UV-Vis electronic spectral studies were conducted for all complexes in 10^{-6} M solutions of $CHCl_3$, DMF, and DMSO solvents, and the spectra are presented in Figure 2b.30. The calculation of Sinha's covalency parameters indicates a small amount of relative covalent character in all complexes. Since uranium is in a +6 oxidation state, only $n \rightarrow \pi^*$, $\pi \rightarrow \pi^*$, and LMCT transitions appeared for complexes in the 200-500 nm range, respectively. By utilizing the values of ν_{comp} from Table 2b.7 and the corresponding ν_{aquo} value (207.3 nm) and averaging over all the transitions, we can compute the values of δ for all solvent systems [41]. These values show the trend of covalent character in the order DMSO > DMF > $CHCl_3$ for all complexes.

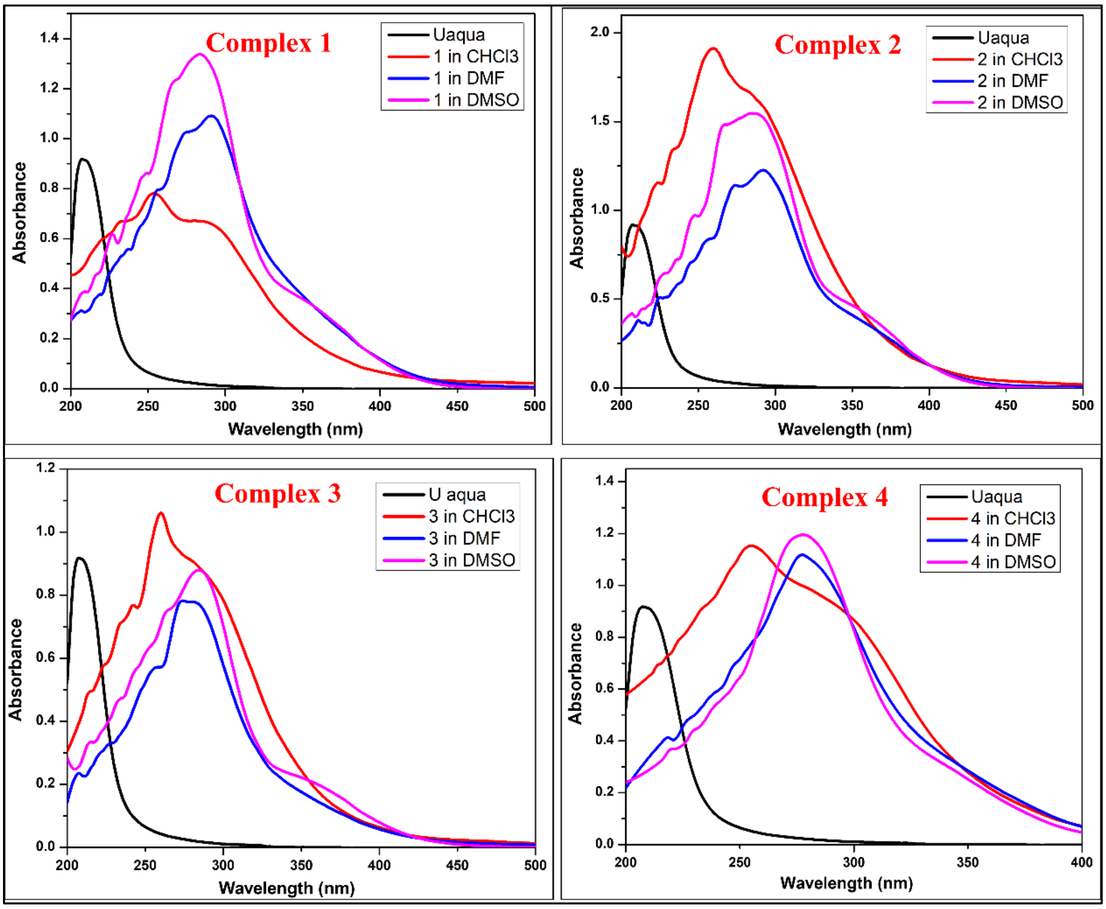

Figure 2b.30 Electronic spectra of complexes 1-4 in $CHCl_3$, DMF and DMSO solvents.

Table 2b.7 Values of Sinha's covalency parameter δ for complexes 1-4 in different solvents.

Complex	**1**	**2**	**3**	**4**	**1**	**2**	**3**	**4**	**1**	**2**	**3**	**4**
Solvent	**$CDCl_3$**				**DMF**				**DMSO**			
ν_{comp} value (nm)	253.9	261.09	260.03	255.0	290.5	291.7	284.0	277.1	283.8	283.0	283.0	277.8
$\delta = \frac{1-\beta}{\beta}$	−0.180	−0.200	−0.202	−0.185	−0.286	−0.286	−0.270	−0.250	−0.270	−0.265	−0.265	−0.252

2b.3.9 Electrochemical analysis

Cyclic voltammetry was conducted, and the corresponding cyclic voltammogram is depicted in Figure 2b.31. Due to the reduction of the uranyl ion ($UO_2^{2+} + e^- \rightarrow UO_2^{+}$), complex 1 exhibits a cathodic potential (E_{Pc}) of −0.94 V and an anodic potential (E_{Ac}) of approximately −0.78 V, indicating the reverse reaction ($UO_2^{+} \rightarrow UO_2^{2+} + e^-$) [17,21]. The E value approaching −0.16 V suggests an irreversible redox reaction. Similarly, Complex 2 displays E_{Pc}, E_{Ac}, and ΔE values of −0.972, −0.822, and

−0.15 V, respectively. Complex 3 shows E_{Pc}, E_{Ac}, and ΔE values of −0.968, −0.797, and −0.171 V, respectively. Complex 4 exhibits E_{Pc}, E_{Ac}, and ΔE values of −1.024, −0.745, and −0.279 V, respectively. The reduction DPV diagram depicted in Figure 2b.32 corresponds to the observed sharp increase.

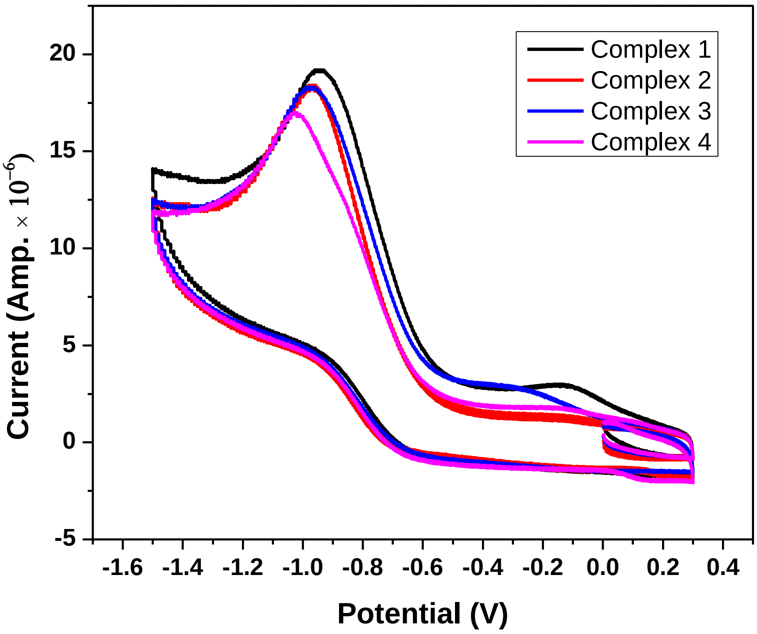

Figure 2b.31 Cyclic voltammograms of complexes 1-4 in DMSO at 25°C.

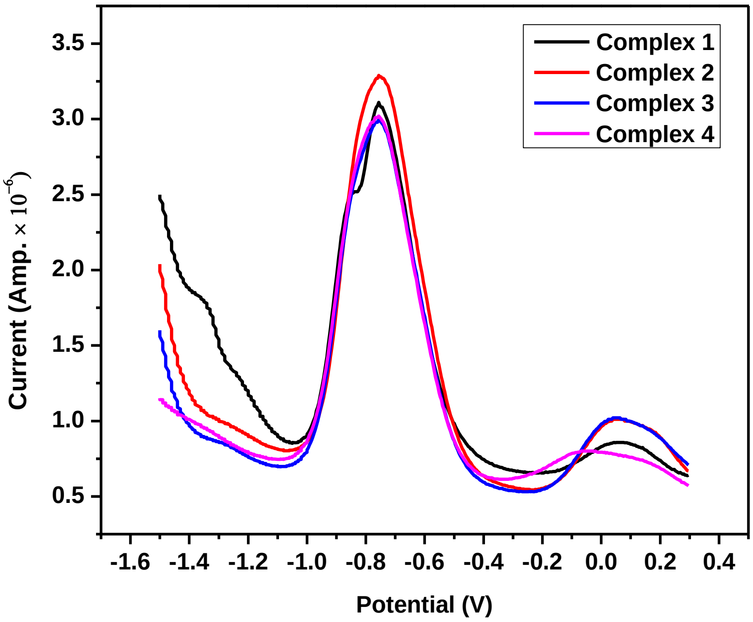

Figure 2b.32 DPV plots of complexes 1-4 in DMSO at 25°C.

2b.4 Conclusions

In this study, we synthesized complexes 1, 2, 3, and 4 of uranyl acylpyrazolone to explore their covalent character sequence, crystal structure, and redox properties. These complexes feature two σ-donating acylpyrazolones and one solvent arranged in an equatorial pentagonal plane with stable pentagonal bipyramidal geometry. Characterization data for these complexes were extensively utilized to analyze their structure, geometry, and composition. FTIR and single-crystal spectral characterization techniques provided valuable information regarding stretching frequencies, average bond lengths of axial uranyl bonds, values of average bond lengths on the pentagonal equatorial plane, solvent coordination on the fifth site of a pentagonal plane, and the type of aryl group on the nitrogen of the pyrazolone ring, shedding light on their impact on covalency order in the complexes. Single crystals of complexes 1 and 3 were obtained in DMSO, while those of complexes 2 and 4 were obtained in DMF solvent. Although all complexes have monoclinic crystal systems, complex 1 has a different space group. Theoretical global metrics further enriched our understanding of the complexes' features. Computational DFT calculations effectively correlated with experimental values. The sequence of covalency, determined as complexes 2 > 3 > 1 > 4, was confirmed through FTIR, XRD data, and DFT computation analysis. Hirshfeld plots were used to analyze donor-acceptor interaction sites and intermolecular contacts. Additionally, CV-DPV analysis revealed that the complexes undergo irreversible reduction. By comprehensively understanding the covalent character of these complexes and their order, we can investigate a wide range of chemical properties and potential applications within the uranyl acylpyrazolone series.

References

[1] R.J.M. Konings, O. Beneš, J.-C. Griveau, 2.01 - The Actinides Elements: Properties and Characteristics, in: R.J.M. Konings (Ed.), Comprehensive Nuclear Materials, Elsevier, Oxford, 2 (2012) 1–20. https://doi.org/10.1016/B978-0-08-056033-5.00008-2.

[2] E. Capelli, R.J.M. Konings, 7.07 - Halides of the Actinides and Fission Products Relevant for Molten Salt Reactors, in: R.J.M. Konings, R.E. Stoller (Eds.), Comprehensive Nuclear Materials (Second Edition), Elsevier, Oxford, 7 (2020) 256–283. https://doi.org/10.1016/B978-0-12-803581-8.11794-1.

[3] R.C. Ewing, Safe management of actinides in the nuclear fuel cycle: Role of mineralogy, Comptes Rendus. Géoscience 343 (2011) 219–229. https://doi.org/10.1016/j.crte.2010.09.003.

[4] A.Yu. Romanchuk, I.E. Vlasova, S.N. Kalmykov, Speciation of Uranium and Plutonium From Nuclear Legacy Sites to the Environment: A Mini Review, Front Chem 8 (2020). https://www.frontiersin.org/articles/10.3389/fchem.2020.00630.

[5] G.J. Lumetta, J.C. Braley, S.I. Sinkov, J.C. Carter, Separating the Minor Actinides Through Advances in Selective Coordination Chemistry, United states (2012). https://doi.org/10.2172/1094957.

[6] A.E. Clark, P. Yang, J.C. Shafer, Coordination of Actinides and the Chemistry Behind Solvent Extraction, in: Experimental and Theoretical Approaches to Actinide Chemistry, (2018) 237–282. https://doi.org/10.1002/9781119115557.ch5.

[7] K.L. Nash, C. Madic, J.N. Mathur, J. Lacquement, Actinide Separation Science and Technology, in: L.R. Morss, N.M. Edelstein, J. Fuger (Eds.), The Chemistry of the Actinide and Transactinide Elements, Springer Netherlands, Dordrecht, (2006) 2622–2798. https://doi.org/10.1007/1-4020-3598-5_24.

[8] F.D. White, M.L. Marsh, Chapter 308 - Recent advances in chemistry of transuranium elements in non-aqueous media, in: J.-C.G. Bünzli, V.K. Pecharsky (Eds.), Handbook on the Physics and Chemistry of Rare Earths, Elsevier, 55 (2019) 123–158. https://doi.org/10.1016/bs.hpcre.2019.07.001.

[9] A. Rump, S. Eder, A. Lamkowski, C. Hermann, M. Abend, M. Port, A quantitative comparison of the chemo- and radiotoxicity of uranium at different enrichment grades, Toxicol Lett 313 (2019) 159–168. https://doi.org/10.1016/j.toxlet.2019.07.004.

[10] T. Yamamura, Y. Shiokawa, H. Yamana, H. Moriyama, Electrochemical investigation of uranium β-diketonates for all-uranium redox flow battery, Electrochim Acta 48 (2002) 43–50. https://doi.org/10.1016/S0013-4686(02)00546-7.

[11] K.C. Mullane, P. Hrobárik, T. Cheisson, B.C. Manor, P.J. Carroll, E.J. Schelter, 13C NMR Shifts as an Indicator of U–C Bond Covalency in Uranium(VI) Acetylide Complexes: An Experimental and Computational Study, Inorg Chem 58 (2019) 4152–4163. https://doi.org/10.1021/acs.inorgchem.8b03175.

[12] P. Thuéry, J. Harrowfield, Cavity Formation in Uranyl Ion Complexes with Kemp's Tricarboxylate: Grooved Diperiodic Nets and Polynuclear Cages, Inorg Chem 60 (2021) 1683–1697. https://doi.org/10.1021/acs.inorgchem.0c03205.

[13] T. Yamamura, Y. Shiokawa, H. Yamana, H. Moriyama, Electrochemical investigation of uranium β-diketonates for all-uranium redox flow battery, Electrochim Acta 48 (2002) 43–50. https://doi.org/10.1016/S0013-4686(02)00546-7.

[14] K.C. Mullane, P. Hrobárik, T. Cheisson, B.C. Manor, P.J. Carroll, E.J. Schelter, 13C NMR Shifts as an Indicator of U–C Bond Covalency in Uranium(VI) Acetylide Complexes: An Experimental and Computational Study, Inorg Chem 58 (2019) 4152–4163. https://doi.org/10.1021/acs.inorgchem.8b03175.

[15] Jos.G. Hamilton, The Metabolism of the Fission Products and the Heaviest Elements, Radiology 49 (1947) 325–343. https://doi.org/10.1148/49.3.325.

[16] K.P. Carter, K.F. Smith, T. Tratnjek, G.J.-P. Deblonde, L.M. Moreau, J.A. Rees, C.H. Booth, R.J. Abergel, Controlling the Reduction of Chelated Uranyl to Stable Tetravalent Uranium Coordination Complexes in Aqueous Solution, Inorg Chem 60 (2021) 973–981. https://doi.org/10.1021/acs.inorgchem.0c03088.

[17] G. Nocton, P. Horeglad, V. Vetere, J. Pécaut, L. Dubois, P. Maldivi, N.M. Edelstein, M. Mazzanti, Synthesis, Structure, and Bonding of Stable Complexes of Pentavalent Uranyl, J Am Chem Soc 132 (2010) 495–508. https://doi.org/10.1021/ja9037164.

[18] I. Shaikh, R.N. Jadeja, R. Patel, V. Mevada, V.K. Gupta, 4-Acylhydrazone-5-Pyrazolones and their Zinc(II) Metal Complexes: Synthesis, Characterization, Crystal Feature and Antimalarial Activity, J Mol Struct 1232 (2021) 130051. https://doi.org/10.1016/j.molstruc.2021.130051.

[19] I. Shaikh, R.N. Jadeja, R. Patel, Three mixed ligand mononuclear Zn(II) complexes of 4-acyl pyrazolones: Synthesis, characterization, crystal study and anti-malarial activity, Polyhedron 183 (2020) 114528. https://doi.org/10.1016/j.poly.2020.114528.

[20] A.I. Vogel, Vogel's textbook of quantitative chemical analysis, Fifth edition. Harlow, Essex, England: Longman Scientific & Technical; New York: Wiley (1989). https://search.library.wisc.edu/catalog/999612906602121.

[21] A.K. Patel, R.N. Jadeja, H. Roy, R.N. Patel, S.K. Patel, R.J. Butcher, Pseudo-tetrahedral copper(II) complex derived from N'-[(2E,3Z)-4-hydroxy-4-phenylbut-3-en-2-ylidene]acetohydrazide: Synthesis, molecular structure, quantum chemical investigations, antioxidant and antiproliferative properties, J Mol Struct 1185 (2019) 341–350. https://doi.org/10.1016/j.molstruc.2019.03.004.

[22] G.M. Sheldrick, SHELXT – Integrated space-group and crystal-structure determination, Acta Acta Crystallogr Section A 71 (2015) 3–8. https://doi.org/10.1107/S2053273314026370.

[23] G.M. Sheldrick, Crystal structure refinement with SHELXL, Acta Crystallogr Section C 71 (2015) 3–8. https://doi.org/10.1107/S2053229614024218.

[24] W.R. Wadt, P.J. Hay, Ab initio effective core potentials for molecular calculations. Potentials for main group elements Na to Bi, J Chem Phys 82 (1985) 284–298. https://doi.org/10.1063/1.448800.

[25] P.J. Hay, W.R. Wadt, Ab initio effective core potentials for molecular calculations. Potentials for the transition metal atoms Sc to Hg, J Chem Phys 82 (1985) 270–283. https://doi.org/10.1063/1.448799.

[26] J.J. Koenderink, A.J. van Doorn, Surface shape and curvature scales, Image Vis Comput 10 (1992) 557–564. https://doi.org/10.1016/0262-8856(92)90076-F.

[27] M.J., Frisch, G.W., Trucks, H.B., Schlegel, G.E., Scuseria, M.A., Robb, J.R., Cheeseman, G., Scalmani, V., Barone, B., Mennucci, G.A., Petersson, H., Nakatsuji,

M., Caricato, X., Li, H.P., Hratchian, A.F., Izmaylov, J., Bloino, G., Zheng, J.L., Sonnenberg, M., Hada, M., Ehara, K., Toyota, R., Fukuda, J., Hasegawa, M., Ishida, T., Nakajima, Y., Honda, O., Kitao, H., Nakai, T., Vreven, J.A., Montgomery, Jr., J.E., Peralta, F., Ogliaro, M., Bearpark, J.J., Heyd, E., Brothers, K.N., Kudin, V.N., Staroverov, R., Kobayashi, J., Normand, K., Raghavachari, A., Rendell, J.C., Burant, S.S., Iyengar, J., Tomasi, M., Cossi, N., Rega, J.M., Millam, M., Klene, J.E., Knox, J.B., Cross, V., Bakken, C., Adamo, J., Jaramillo, R., Gomperts, R.E., Stratmann, O., Yazyev, A.J., Austin, R., Cammi, C., Pomelli, J.W., Ochterski, R.L., Martin, K., Morokuma, V.G., Zakrzewski, G.A., Voth, P., Salvador, J.J., Dannenberg, S., Dapprich, A.D., Daniels, Ö., Farkas, J.B., Foresman, Orti., Gaussian 09, Revision E.01, Gaussian, Inc., Wallingford, CT (2013).

[28] J.J. Koenderink, A.J. van Doorn, Surface shape and curvature scales, Image Vis Comput 10 (1992) 557–564. https://doi.org/10.1016/0262-8856(92)90076-F.

[29] M. Dolg, U. Wedig, H. Stoll, H. Preuss, Energy-adjusted ab initio pseudopotentials for the first row transition elements, J Chem Phys 86 (1987) 866–872. https://doi.org/10.1063/1.452288.

[30] G.A. Petersson, M.A. Al-Laham, A complete basis set model chemistry. II. Open-shell systems and the total energies of the first-row atoms, J Chem Phys 94 (1991) 6081–6090. https://doi.org/10.1063/1.460447.

[31] S.P. McGlynn, J.K. Smith, W.C. Neely, Electronic Structure, Spectra, and Magnetic Properties of Oxycations. III. Ligation Effects on the Infrared Spectrum of the Uranyl Ion, J Chem Phys 35 (1961) 105–116. https://doi.org/10.1063/1.1731876.

[32] J.E. Niklas, K.M. Hunter, A.E. V Gorden, Bonding Interactions in Uranyl α-Diimine Complexes: A Spectroscopic and Electrochemical Study of the Impacts of Ligand Electronics and Extended Conjugation, Inorg Chem 58 (2019) 15088–15100. https://doi.org/10.1021/acs.inorgchem.9b01695.

[33] M.S. Nagar, P.B. Ruikar, M.S. Subramanian, Complexes of tetravalent plutonium, uranium and thorium with acylpyrazolones, Inorganica Chim Acta 141 (1988) 309–312. https://doi.org/10.1016/S0020-1693(00)83925-0.

[34] F. Marchetti, C. Pettinari, R. Pettinari, Acylpyrazolone ligands: Synthesis, structures, metal coordination chemistry and applications, Coord Chem Rev 249 (2005) 2909–2945. https://doi.org/10.1016/j.ccr.2005.03.013.

[35] W.J. Geary, The use of conductivity measurements in organic solvents for the characterisation of coordination compounds, Coord Chem Rev 7 (1971) 81–122. https://doi.org/10.1016/S0010-8545(00)80009-0.

[36] R.R. Ryan, G.D. Jarvinen, Structure of bis(4-benzoyl-2,4-dihydro-5-methyl-2-phenyl-3 H-pyrazol-3-onato- O,O')(dimethyl sulfoxide- O)dioxouranium(VI), Acta Crystallogr Section C 43 (1987) 1295–1298. https://doi.org/10.1107/S0108270187092114.

[37] F. Marchetti, C. Pettinari, C. Di Nicola, A. Tombesi, R. Pettinari, Coordination chemistry of pyrazolone-based ligands and applications of their metal complexes, Coord Chem Rev 401 (2019) 213069. https://doi.org/10.1016/j.ccr.2019.213069.

[38] Y. Singh, R.N. Patel, S.K. Patel, A.K. Patel, N. Patel, R. Singh, R.J. Butcher, J.P. Jasinski, A. Gutierrez, Experimental and quantum computational study of two new bridged copper(II) coordination complexes as possible models for antioxidant superoxide dismutase: Molecular structures, X-band electron paramagnetic spectra and cryogenic magnetic properties, Polyhedron 171 (2019) 155–171. https://doi.org/10.1016/j.poly.2019.07.015.

[39] R.N. Patel, S.K. Patel, D. Kumhar, N. Patel, A.K. Patel, R.N. Jadeja, N. Patel, R.J. Butcher, M. Cortijo, S. Herrero, Two new copper(II) binuclear complexes with 2-[(E)-(pyridine-2yl-hydrazono)methyl]phenol: Molecular structures, quantum chemical calculations, cryomagnetic properties and catalytic activity, Polyhedron 188 (2020) 114687. https://doi.org/10.1016/j.poly.2020.114687.

[40] D. Shoba, S. Periandy, M. Karabacak, S. Ramalingam, Vibrational spectroscopy (FT-IR and FT-Raman) investigation, and hybrid computational (HF and DFT) analysis on the structure of 2,3-naphthalenediol, Spectrochim Acta A Mol Biomol Spectrosc 83 (2011) 540–552. https://doi.org/10.1016/j.saa.2011.09.002.

[41] S.P. Sinha, Spectroscopic investigations of some neodymium complexes, Spectrochim Acta 22 (1966) 57–62. https://doi.org/10.1016/0371-1951(66)80008-5.

CHAPTER 2

Part (c): Uranyl(VI) Mixed-ligand complex synthesis and characterization using 4-acylhydrazone-5-pyrazolone and 4-acylpyrazolone: Covalency, crystal assay, DFT study and Hirshfeld analysis.

2c.1 Introduction

The widely recognized synthon pyrazolone plays a crucial role in synthesizing diverse compounds, offering significant potential for advancements in medicinal and coordination chemistry [1]. According to Jensen, there is a growing trend towards using the acylation technique to synthesize chelating ligands with enhanced donor atom capabilities [2]. Consequently, a plethora of acylated pyrazolones and their corresponding complexes exhibiting various geometries have become commonplace [3,4]. One notable characteristic of acylpyrazolone is its propensity to form Schiff bases, thereby augmenting their donor ability and denticity within coordination environments [5]. The Schiff bases derived from hydrazine-based compounds in conjunction with acylpyrazolone find numerous applications [6–10]. Notably, tridentate ligands originating from benzo hydrazides are esteemed for their O-N-O donor sites [11,12]. These ligands are renowned for their ability to form complexes with inner transition metals, resulting in a spectrum of geometries, including pentagonal bipyramidal, tricapped trigonal prismatic, square antiprismatic, and others [5].

Determining the nature and extent of covalency is essential, especially given the challenge of discerning inner transition metal complex features. Covalency forms the basis for describing the bonding in Ln-acylpyrazolone [13]. There's a growing interest in understanding Ln-acylpyrazolone bonding due to the observable covalent characteristics in these compounds' bonds. Actinides pose significant challenges such as radioactivity, larger size, shorter lifetime, high cost, and hazardous properties, often deter research efforts. Therefore, it becomes crucial to explore more accessible elements as representatives of certain other elements. Despite differences in chemistry, uranyl stands out as a more readily available and advantageous option compared to minor actinides like americium and curium in contemporary research [13,14].

Exploration into various stable compounds featuring UO_2^{2+} has contributed to the expansion of uranyl acylpyrazolone complexes, offering diverse growth possibilities. The synthesis of numerous pentagonal bipyramidal uranyl acylpyrazolone has been facilitated by their straightforward synthesis and propensity for crystallization [15–18]. Additionally, a handful of dioxouranium(VI) complexes within octahedral environments have been documented using Schiff bases derived from acylpyrazolone [19,20]. In Chapter 2(b), we presented a study leveraging the covalent properties of uranyl acylpyrazolone, achieving a pentagonal bipyramidal geometry through the coordination of two bidentate acylpyrazolone ligands and one solvent molecule. In this chapter, we included the synthesis of a mixed ligand uranyl complex, marking the first instance of such a synthesis aimed at assessing the combined impact of bidentate and tridentate acylpyrazolone ligands within the complex. This study provides insights into the binding, covalency, and characterization of mixed ligand uranyl complexes incorporating bidentate L^5 and tridentate L^7 acylpyrazolone ligand.

2c.2 Experimental section

2c.2.1 Materials and Methods

HL^5 and HL^7 ligands were synthesized and used by employing the methodologies given in chapter 2(a). Uranyl nitrate procured from SULAB Chemicals in Gujarat was introduced into the solution. The uranium concentration was determined using gravimetric techniques, expressed as U_3O_8 [21]. AR-grade solvents for recrystallization were purchased from CDH Chemicals, a Central Drug House (P) Ltd division.

2c.2.2 Synthesis of mixed ligand uranyl complex

The uranium complex 5 was synthesized according to the procedure outlined in Figure 2c.1 using HL^5 and HL^7 ligands.

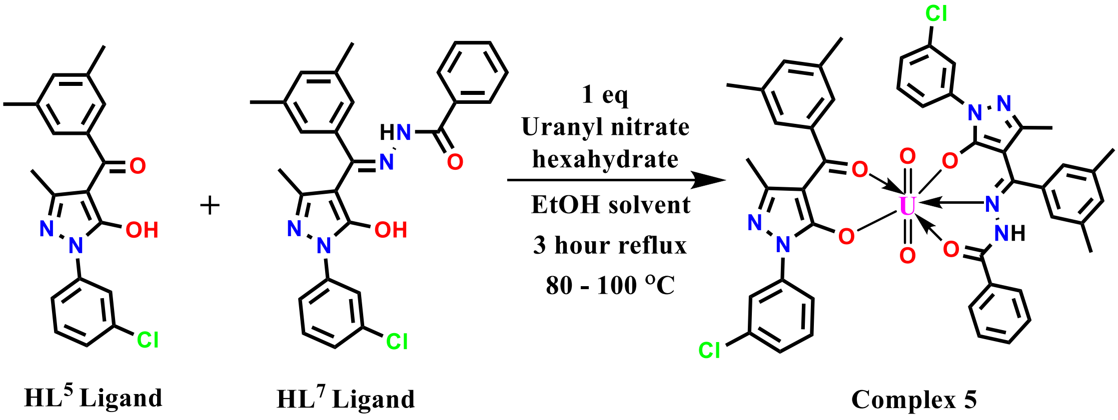

Figure 2c.1 Synthetic route for mixed ligand uranyl complex.

A 1:1 ethanolic mixture of HL^5 and HL^7 ligands was stirred at 80-100 °C for half an hour. Subsequently, an equimolar ethanolic solution of uranyl nitrate was added dropwise. The solution was refluxed for 3 hours and then transferred to a beaker. Bright prism-type orange-brown coloured crystals of the uranyl complex were obtained using a slow evaporation technique. Yield (%): 92.72%, M.P.: >200 °C, Molecular formula:

$C_{45}H_{38}Cl_2N_6O_6U$, Formula wt: 1067.76. **FTIR (KBr, cm^{-1}):** 3426 (m, $\upsilon_{\text{N-H near to acylpyz}}$), 2972 (w, $\upsilon_{\text{N-H near BZ}}$), 1600 (s, $\upsilon_{\text{C=O benzoyl / benzo hydrazone}}$), 1557 (s, $\upsilon_{\text{C=O acylpyz}}$), 1476, 1436 (s, $\upsilon_{\text{C=N acylpyz}}$), 914 (s, $\upsilon_{\text{U=O axial asym.}}$), 776 (s, $\upsilon_{\text{U=O axial sym.}}$). **^{1}H-NMR δ-ppm (400MHz, DMSO d$_6$):** 11.026 (s, 1H, near benzo hydrazone), 2.397 (s, 6H, L^5-$CH_{3\text{(dimethyl benzoyl)}}$), 2.297 (s, 6H, L^7-$CH_{3\text{(dimethyl benzoyl)}}$), 1.963 (s, 3H, L^7-$CH_{3\text{(acylpyz)}}$), 1.466 (s, 3H, L^5-$CH_{3\text{(acylpyz)}}$), 7.0-8.6 (m, Ar-H).

2c.2.3 X-ray crystallographic examination

X-ray crystallographic analysis was conducted on all four uranyl complexes using Mo-K$_\alpha$ ($\lambda = 0.71073$ Å) radiation and graphite monochromator. The detection and refinement procedures were performed using methods outlined in previously published papers from our laboratory. [22]. The diffraction data were solved using the SHELXT software [23], while computation was done using the crystallographic software SHELXL-2018/3 [24].

2c.2.4 Physical measurements and characterization techniques

Analogous methodologies, models, instruments, or instruments were employed to analyze the data of the synthesized compounds, using techniques such as FTIR, ^{1}H-NMR, CV-DPV, and TG-DTA, following procedures outlined in previously published articles from our laboratory [22,25]. Electrochemical analysis of the complexes in DMSO containing 0.1 M TBAP as the supporting electrolyte was conducted using cyclic voltammetry with a three-electrode system under de-aerated conditions and a BAS 100 electrochemical analyzer. A glassy-carbon electrode and platinum wire were the working and counter electrodes. The reversibility of the electrochemical process was evaluated following standard procedures, and all potentials were recorded against an Ag/AgCl reference electrode. Nitric acid decomposition of the complexes facilitated volumetric and gravimetric measurement of uranium content, expressed as U_3O_8.

2c.2.5 Computational study

Geometry optimizations and DFT computations were performed on all four complexes employing the B3LYP method [26–29] and executed using the GAUSSIAN 16 software [29,30]. Input file processing was conducted using Gaussview 6.0 [31,32]. The SDD basis set was used for all components in the three complexes. With this method, calculations were performed to analyze molecular structure, vibrational properties, and other relevant factors.

2c.3 Results and Discussion

This mixed ligand uranyl acylpyrazolone complex exhibits exceptional stability at ambient temperatures, with uranyl forming covalent bonds with both ligands. Furthermore, the subsequent section elucidates the extent of covalent bonding along with crystal formations.

2c.3.1 FTIR spectral analysis

Valuable insights into complex formation can be derived from the FTIR spectra, particularly by analyzing the C=O/C=N bands, O-H/N-H stretching, and U-O vibrations. HL^5 exhibits $\upsilon_{C=O\ \text{dimethyl-benzoyl}}$ and $\upsilon_{C=O\ \text{acyl-pyz}}$ bands at 1621 and 1589 cm^{-1}, respectively. In contrast, HL^7 displays bands corresponding to $\upsilon_{C=O\ \text{BZ group}}$, $\upsilon_{C=O\ \text{dimethyl-benzoyl}}$, and $\upsilon_{C=O\ \text{acyl-pyz}}$ at 1640, 1595, and 1595 cm^{-1}, respectively. The uranyl complex exhibits bands for $\upsilon_{C=O\ \text{dimethyl-benzoyl}}$, $\upsilon_{C=O\ \text{BZ group}}$, and $\upsilon_{C=O\ \text{acyl-pyz}}$ at 1600, 1600, and 1557 cm^{-1}, respectively. A notable observation is the reduction in $\upsilon_{C=O}$ values for both ligands upon complexation. This indicates a weakening of the C=O bonds due to charge donation to the uranyl ion in complex 5, thus confirming complex formation. Additional pertinent data regarding $\upsilon_{C=N}$ frequencies, O-H/N-H stretching, and U-O ($\upsilon_{as}/\upsilon_{s}$) vibrations can be found in Table 2c.1. The FTIR spectrum for complex 5 is depicted in Figure 2c.2.

Table 2c.1 The FTIR values for HL^5, HL^7 ligands and complex 5 (in cm^{-1}).

Code	HL^5 Ligand	HL^7 Ligand	Complex 5
$\nu_{(C=O)}$ benzoyl	1621	-	1600
$\nu_{(C=O)}$ acyl	1589	1595	1557
$\nu_{(C=O)}$ benzohydrazide	-	1640	1600
cyclic $\nu_{(C=N)}$	1554	1518	1476
$\nu_{C\text{-}C}$ aromatic	1344	1368	1374
$\nu_{(N\text{-}N)}$	1176	1142	1145
C-H in plane deformation	1080	1064	1067
$\nu_{as\ (U=O)}$	-	-	914
$\nu_{s\ (U=O)}$	-	-	776

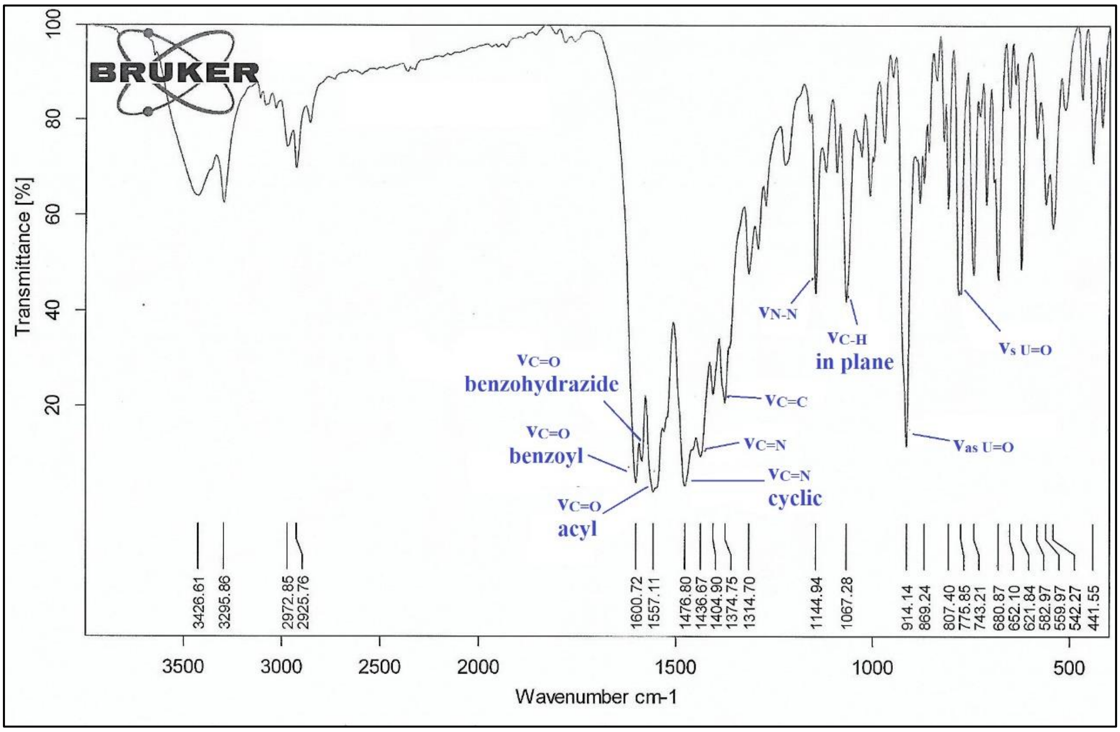

Figure 2c.2 FTIR spectrum of complex 5.

2c.3.2 ^{1}H-NMR spectroscopic study

The NMR spectrum of complex 5 was taken in DMSO-d_6 solvent and presented in Figure 2c.3. Synthesized complex 5 shows N-H singlet at 11.026 δ, CH_3 singlet of L^5-dimethylbenzoyl at 2.397 δ, CH_3 singlet of L^7-dimethylbenzoyl at 2.297 δ, CH_3 singlet of L^5-pyrazolone ring at 1.466 δ, CH_3 singlet of L^7-pyrazolone ring at 1.963 δ, and aromatic proton peaks in 7.0-8.6 δ range in ^{1}H-NMR spectrum (See Figure 2c.3).

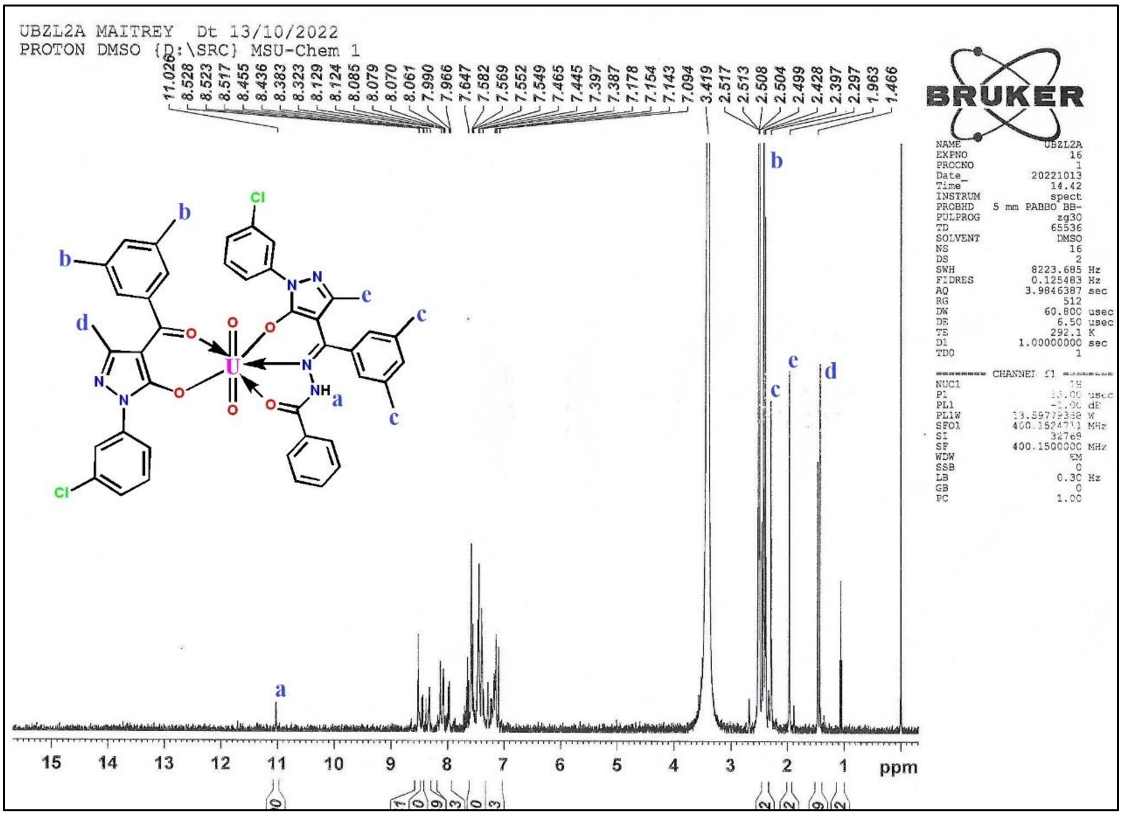

```
NAME          UBZL2A
EXPNO             16
PROCNO             1
Date_       20221013
Time           14.42
INSTRUM        spect
PROBHD   5 mm PABBO BB-
PULPROG         zg30
TD             65536
SOLVENT         DMSO
NS                16
DS                 2
SWH         8223.685 Hz
FIDRES      0.125483 Hz
AQ         3.9846387 sec
RG               512
DW            60.800 usec
DE              6.50 usec
TE             292.1 K
D1        1.00000000 sec
TD0                1

======== CHANNEL f1 ========
NUC1              1H
P1             13.00 usec
PL1            -1.00 dB
PL1W     13.59779358 W
SFO1     400.1524711 MHz
SI             32768
SF       400.1500000 MHz
WDW               EM
SSB                0
LB              0.30 Hz
GB                 0
PC              1.00
```

Figure 2c.3 ^{1}H-NMR spectrum of complex 5.

2c.3.3 Thermogravimetric analysis

The thermogravimetric (TGA) analysis of complex 5 reveals a two-step degradation process. Initially, up to 100 °C, solvent removal from the complex, prepared in ethanol, leads to an 8.8% mass loss. At 61.8 °C, a notable shift of 48.1 μg/min is observed in the DTG curve. The second step, occurring above 300 °C, involves the removal of ligands L^5 and L^7 from the pentagonal plane. This step is characterized by a distinct peak in the DTA curve, with the DTG curve showing significant shifts at 341.9 °C and 393.4 °C, with values of 122.8 μg/min and 209.0 μg/min, respectively. Ultimately, the metal component undergoes the transformation into uranium oxide (U_3O_8). The TG curve for complex 5 is depicted in Figure 2c.4.

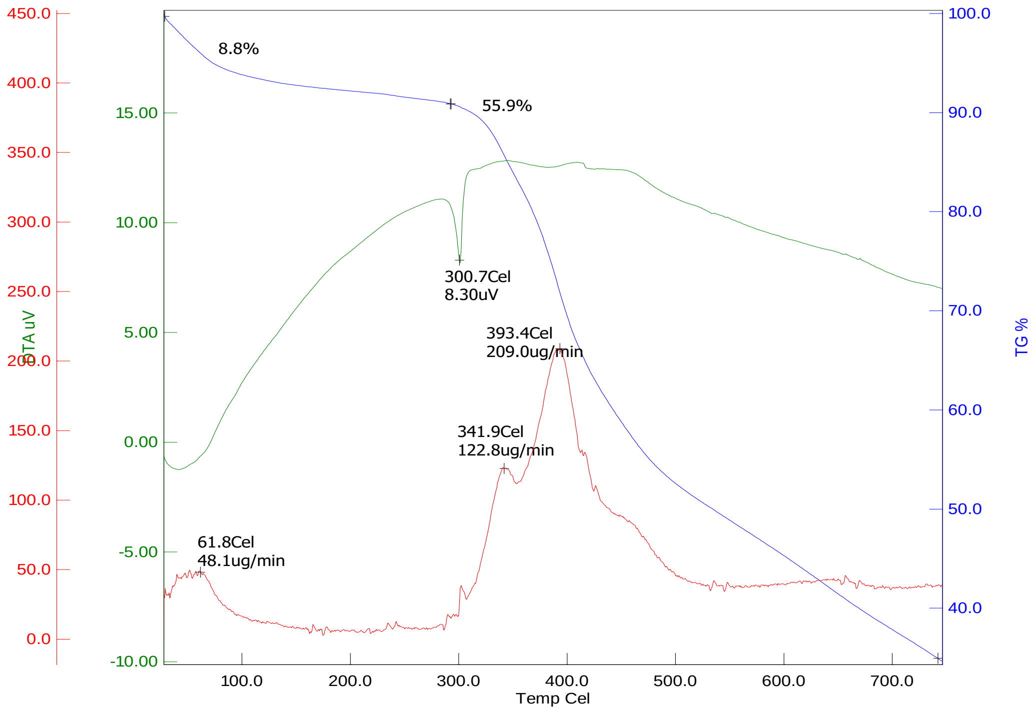

Figure 2c.4 Thermogravimetric curve of complex 5.

2c.3.4 Molar conductivity measurements

The molar conductivity value for solution of complex 5 in DMF was determined to be 4.23 cm^2 mol^{-1}. This relatively low value suggests the absence of charged species within the coordination sphere of the complex, indicating non-electrolytic behaviour [33].

2c.3.5 Single crystal X-ray diffraction analysis

The X-ray crystallographic analysis of complex 5 revealed red-coloured prism-type crystals with a monoclinic system and $P\ 2_1/c$ space group, exhibiting a pentagonal bipyramidal geometry [See Figure 2c.5 and Table 2c.2]. In this crystal, uranyl is bonded to one tridentate L^7 ligand and one bidentate L^5 ligand, forming a complex crystal structure. Upon binding, a six-membered ring forms between the L^5 ligand and the pyrazolone side of the L^7 ligand, while only the benzhydrazone side of the L^7 ligand stabilizes with a five-membered ring formation.

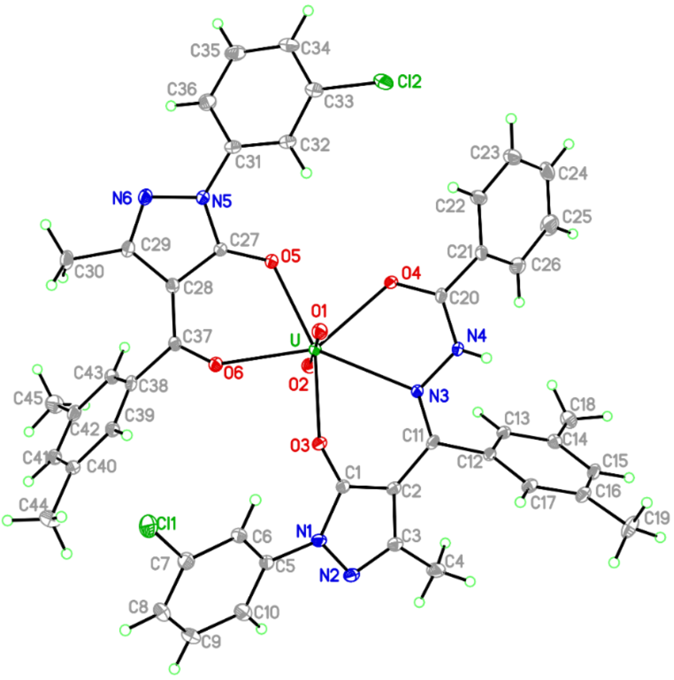

Figure 2c.5 Molecular structure of complex 5 drawn at 50 % probability level.

The complex displays an average axial U=O distance of 1.778 Å, with $d_{U\text{-}O(1)}$ measured at 1.784(3) Å and $d_{U\text{-}O(2)}$ at 1.772(3) Å [See Table 2c.3]. The equatorial U-O/N distances on the pentagonal plane measure 2.404 Å, with $d_{U\text{-}O(3)}$ at 2.286(3) Å, $d_{U\text{-}O(6)}$ at 2.338(3) Å, $d_{U\text{-}O(5)}$ at 2.351(3) Å, $d_{U\text{-}O(4)}$ at 2.407(3) Å, and $d_{U\text{-}N(3)}$ at 2.638(3) Å. The longer bond length of U-N(3) (2.638(3) Å) indicates weaker bonding strength compared to O-atom donors. Axial uranyl U-O bonds exhibit shorter lengths than their equivalent equatorial bonds due to a double bond character. Additionally, the smaller distances of U-O(5) (2.351(3) Å) in the L^5 ligand and U-O(3) (2.286(3) Å) in the L^7 ligand suggest the stronger donating ability of the C=O group of the pyrazolone ring.

The uranyl O(2)-U-O(1) angle of 179.06° indicates a tendency towards greater axial linearity in the complex [15,17,18,34–37]. Furthermore, due to the tridentate O-N-O binding by the L^7 ligand, angles O(4)-U-N(3) and O(3)-U-N(3) measure 62.78° and 69.85°, respectively, smaller than the ideal pentagonal angle of 72°. Consequently, angles O(4)-U-O(5) (73.74°), O(5)-U-O(6) (73.31°), and O(6)-U-O(3) (83.49°) are higher than 72°. These structural features collectively influence the covalent character of the synthesized complex. Lower U-(O5) and U-O(6) bond length values suggest a greater covalent character of uranyl with the L^5 ligand. Secondary interactions such as N(4)-H(1)···O(1)#1, C(4)-H(4C)···O(2)#2, C(6)-H(6A)···O(3), C(30)-H(30B)···Cl(2)#3, and C(32)-H(32A)···O(5) are also observed [See Table 2c.4].

Table 2c.2 Structural refinement data for complex 5.

Code	Complex 5
CCDC number	2220754
Empirical formula	$C_{45}H_{38}ClN_6O_6U$
Formula weight	1067.74
Temperature	100(2) K
Wavelength	0.71073 Å
Crystal system	Monoclinic
Space group	$P\,2_1/c$
Unit cell dimensions	a = 10.6155(7) Å, b = 16.1944(12) Å, c = 24.5072(16) Å, α= 90°, β= 99.168(2)°, γ=90°
Volume	4159.3(5) Å^3
Z	4
Density (calculated)	1.705 Mg/m^3
Absorption coefficient	4.088 mm^{-1}
F(000)	2096
Final R indices [I>2sigma(I)]	R_1 = 0.0380, wR_2 = 0.0829
R indices (all data)	R_1 = 0.0608, wR_2 = 0.0933
Theta range for data collection	2.36 to 30.22°.
Index ranges	−15<=h<=15, −23<=k<=21, −35<=l<=35
Reflection collected	99178
Independent reflections	12707 [$R_{(int)}$ = 0.1378]
Completeness to theta = 25.242°	99.9%
Absorption correction	None
Refinement method	Full-matrix least-squares on F^2
Goodness-of-fit on F^2	1.032
Data / restraints / parameters	12707 / 0 / 550

Table 2c.3 Bond parameters for complex 5.

Atoms	Bond lengths	Atoms	Bond lengths	Atoms	Bond angles	Atoms	Bond angles
U-O(2)	1.772(3)	O(4)-C(20)	1.258(4)	O(2)-U-O(1)	179.06(13)	O(3)-U-O(5)	156.06(9)
U-O(1)	1.784(3)	O(5)-C(27)	1.280(4)	O(2)-U-O(3)	95.63(11)	O(6)-U-O(5)	73.31(9)
U-O(3)	2.286(3)	O(6)-C(37)	1.275(4)	O(1)-U-O(3)	84.21(11)	O(2)-U-O(4)	93.41(12)
U-O(6)	2.338(3)	N(3)-C(11)	1.306(5)	O(2)-U-O(6)	86.31(11)	O(1)-U-O(4)	87.40(11)
U-O(5)	2.351(3)	N(3)-N(4)	1.396(4)	O(1)-U-O(6)	92.75(11)	O(3)-U-O(4)	129.19(9)
U-O(4)	2.407(3)	N(4)-C(20)	1.325(5)	O(3)-U-O(6)	83.49(9)	O(6)-U-O(4)	147.06(9)
U-N(3)	2.638(3)	C(11)-C(12)	1.497(5)	O(2)-U-O(5)	88.80(11)	O(5)-U-O(4)	73.74(9)
O(3)-C(1)	1.293(4)	C(20)-C(21)	1.475(5)	O(1)-U-O(5)	90.97(11)	O(2)-U-N(3)	79.95(11)
N(5)-N(6)	1.404(4)	N(5)-C(27)	1.355(5)	O(3)-U-N(3)	69.85(9)	O(1)-U-N(3)	100.85(11)
N(6)-C(29)	1.315(5)	C(28)-C(29)	1.435(5)	O(4)-U-N(3)	62.78(9)	C(37)-C(28)-C(27)	122.0(3)

Table 2c.4 Hydrogen bonds for complex 5 [Å and °].

D-H···A	d(D-H)	d(H···A)	d(D···A)	<(DHA)
N(4)-H(1)···O(1)#1	0.71(5)	2.38(5)	2.924(4)	135(5)
C(4)-H(4C)···O(2)#2	0.98	2.59	3.402(6)	140.8
C(6)-H(6A)···O(3)	0.95	2.31	2.904(5)	120.1
C(30)-H(30B)···Cl(2)#3	0.98	2.86	3.533(4)	126.5
C(32)-H(32A)···O(5)	0.95	2.23	2.867(5)	123.5

Symmetry transformations used to generate equivalent atoms: #1 -x,-y+1,-z+2

2c.3.6 DFT computational analysis

Complex 5 underwent DFT computational analysis to explore and correlate its chemical and physical properties by examining theoretically optimized geometry (Figure 2c.6), frontier orbitals, bond parameters, and vibrations [36,38,39]. The electronic energies of all optimized compounds were determined to be −39.57, −49.90, and −106.53 keV, respectively. Increasing energy values indicate a rising stability hierarchy, with the uranyl complex demonstrating the highest stability owing to its more negative electrical energy.

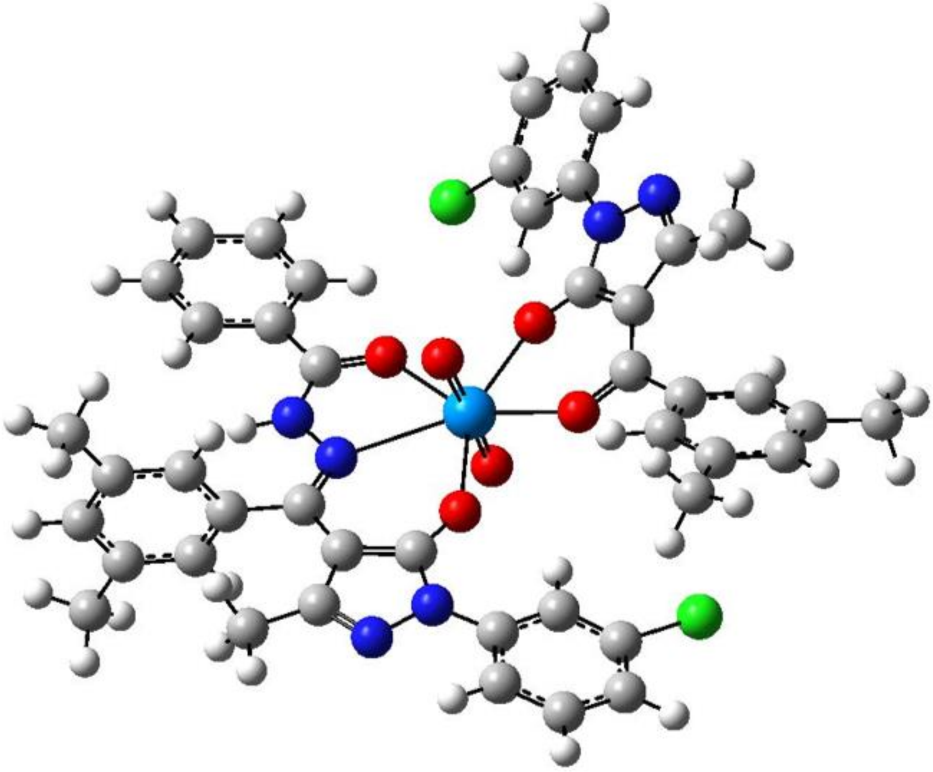

Figure 2c.6 DFT optimized geometry of complex 5.

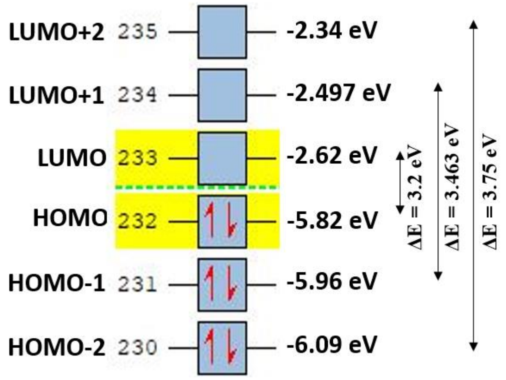

Figure 2c.7 HOMO-LUMO energy value for complex 5.

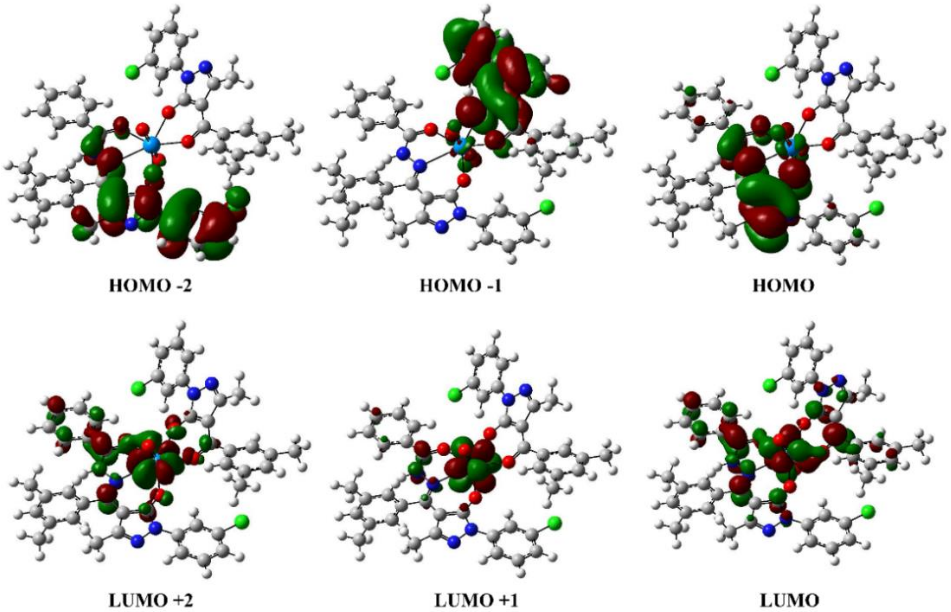

Figure 2c.8 HOMO-LUMO frontier orbitals for complex 5.

Figures 2c.7 and 2c.8 illustrate the HOMO, HOMO−1, and HOMO−2 with energies of −5.82, −5.96, and −6.09 eV for complex 5, respectively. The LUMO, LUMO+1, and LUMO+2 energies are −2.669, −2.627, and −2.33 eV, respectively, located near the metal center. Chemical stability is reflected in the $E_{HOMO-LUMO}$, $E_{HOMO-1-LUMO-1}$, and $E_{HOMO-2-LUMO-2}$ values, measured at 3.2, 3.463, and 3.75 eV for complex 5. The presence of paired electrons in all HOMOs explains the diamagnetic behaviour of the complex. Comparison of DFT data between L^5 and L^7 from Chapter 2(a) reveals a narrowing of the energy gap when progressing from L^5 to L^7 and subsequently to complex 5. Global parameters provide comprehensive insights into the characteristics of synthesized complexes, as detailed in Table 2c.5. For further investigation, Table 2c.6 presents significant theoretical bond lengths and angles, which closely resemble experimental values.

Table 2c.5 Global index parameters for complex 5.

Properties of Complex	**Mathematical Formula**	**Complex 5**
E_{HOMO}	E_{HOMO}	−2.62
E_{LUMO}	E_{LUMO}	−5.82
ΔE	$\Delta E = E_{LUMO} - E_{HOMO}$	3.2
Ionization potential (IP)	$IP = -E_{HOMO}$	2.62
Chemical Potential (μ)	$\mu = \frac{1}{2} (E_{Homo} + E_{Lumo})$	5.82
Electron affinity (EA)	$EA = -E_{LUMO}$	−4.22
Electronegativity (EN)	$EN = -\frac{1}{2} (E_{Homo} + E_{Lumo})$	1.6
Global Hardness (η)	$\eta = -\frac{1}{2} (E_{Homo} - E_{Lumo})$	0.312
Softness (S)	$S = 1/2\eta$	4.22
Electrophilicity index (ω)	$\omega = \mu^2/2\eta$	5.556

Table 2c.6 Bond parameters comparison for complex 5.

Atoms numbering as in Figure 2c.5	**Experimental Bond lengths (in Å)**	**Theoretical Bond lengths (in Å)**	**Atoms numbering as in Figure 2c.5**	**Experimental Bond angles (in °)**	**Theoretical Bond angles (in °)**
U-O(2)	1.772(3)	1.7979	O(2)-U-O(1)	179.06(13)	176.72
U-O(1)	1.784(3)	1.7935	O(3)-U-O(6)	83.49(9)	81.21
U-O(3)	2.286(3)	2.2931	O(6)-U-O(5)	73.31(9)	71.21
U-O(6)	2.338(3)	2.3393	O(3)-U-N(3)	69.85(9)	68.42
U-O(5)	2.351(3)	2.3604	O(4)-U-N(3)	62.78(9)	62.30
U-O(4)	2.407(3)	2.4051	O(5)-U-O(4)	73.74(9)	78.02
U-N(3)	2.638(3)	2.7335	O(1)-U-O(3)	84.21(11)	87.69
O(3)-C(1)	1.293(4)	1.2992	O(1)-U-O(6)	92.75(11)	96.83
N(3)-C(11)	1.306(5)	1.3391	O(1)-U-O(5)	90.97(11)	89.19
O(4)-C(20)	1.258(4)	1.2812	O(1)-U-O(4)	87.40(11)	88.29
O(5)-C(27)	1.280(4)	1.2987	O(1)-U-N(3)	100.85(11)	94.83
O(6)-C(37)	1.275(4)	1.3029	O(2)-U-O(3)	95.63(11)	93.26

Theoretical vibrations offer a detailed insight into the changes occurring during complexation, as evidenced by frequency values. Generally, when theoretical values closely resemble those obtained experimentally in FTIR spectroscopic analysis, each point mentioned in the previous section gains significance. Notably, the relative influence of uranium asymmetric and symmetric vibrations provides a solid understanding of the differences between axial and equatorial bonds. Table 2c.7 presents the essential theoretical vibration values alongside actual FTIR spectrum values, offering a comparison. Additionally, Figure 2c.9 displays the DFT-optimized IR spectra, providing further clarity on the vibrational characteristics of the complex.

Table 2c.7 DFT optimized vibrational frequency comparison with experimental values in complex 5.

Code	Complex 5	
	Experimental	Theoretical
$\nu_{(C=O)}$ benzoyl	1600	1595
$\nu_{(C=O)}$ acyl	1557	1571
$\nu_{(C=O)}$ benzohydrazide	1600	1578
cyclic $\nu_{(C=N)}$	1476	1557
$\nu_{(C=N)}$	1436	1400
$\nu_{as\ (U=O)}$	914	926
$\nu_{s\ (U=O)}$	776	847

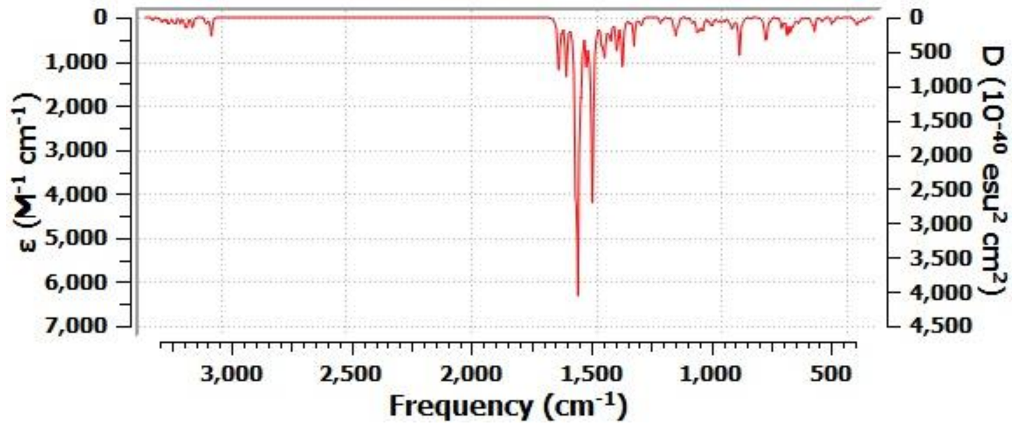

Figure 2c.9 FTIR spectrum of complex 5 optimized through computational analysis.

2c.3.7 Hirshfeld surface area analysis

Using the Crystal Explorer 17.5 program [40,41], the donor-acceptor interaction sites and intermolecular contacts for complex 5 can be visualized (refer to Figure 2c.10). As depicted in Figure 2c.10, the presence of prominent red spots on the d_{norm} surface indicates intermolecular hydrogen bonds and also suggest better proximity to neighbouring moieties or shorter contacts between halogen bonds. Additionally, the curved portions of the curvedness plot surrounding the aromatic rings suggest stacking, thereby enhancing the stability of the crystal lattice. The packing probability of complexes can be assessed using percentage statistics for atom-all and all-atom interactions. Notably, there are no U-all, U-U, or all-U connections in the complex, indicating that uranium does not form secondary interactions with the surrounding atoms of the molecules. Significant hydrogen interactions have been observed for the complex, with H-all and All-H interactions, as illustrated in Figure 2c.11. Figure 2c.12 presents 2D FP plots corresponding to all such interactions.

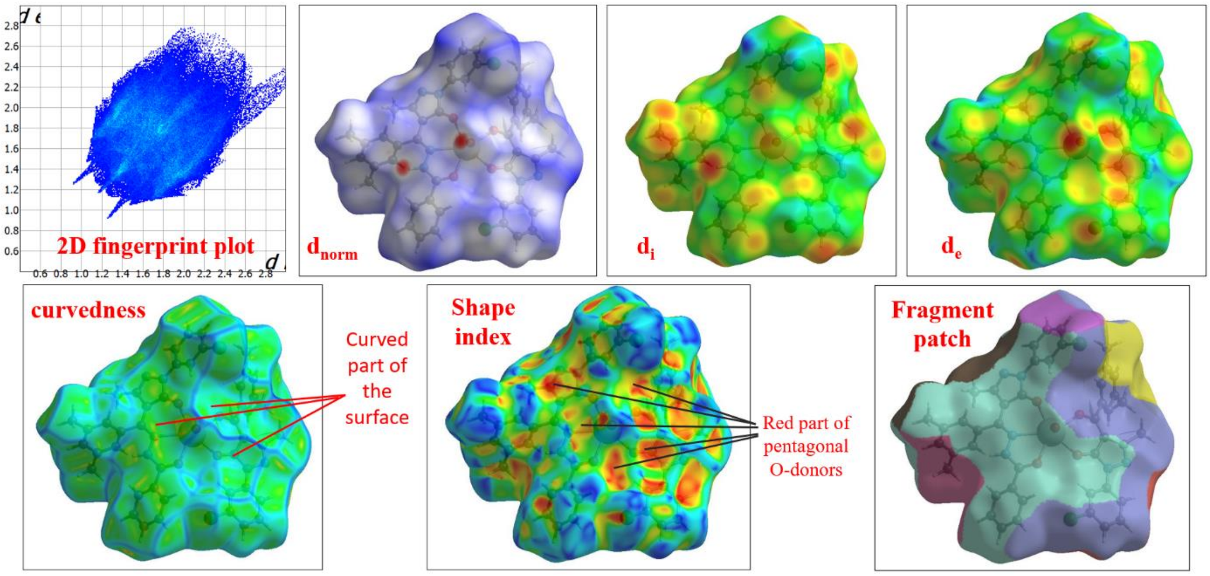

Figure 2c.10 The molecular HS for complex 5.

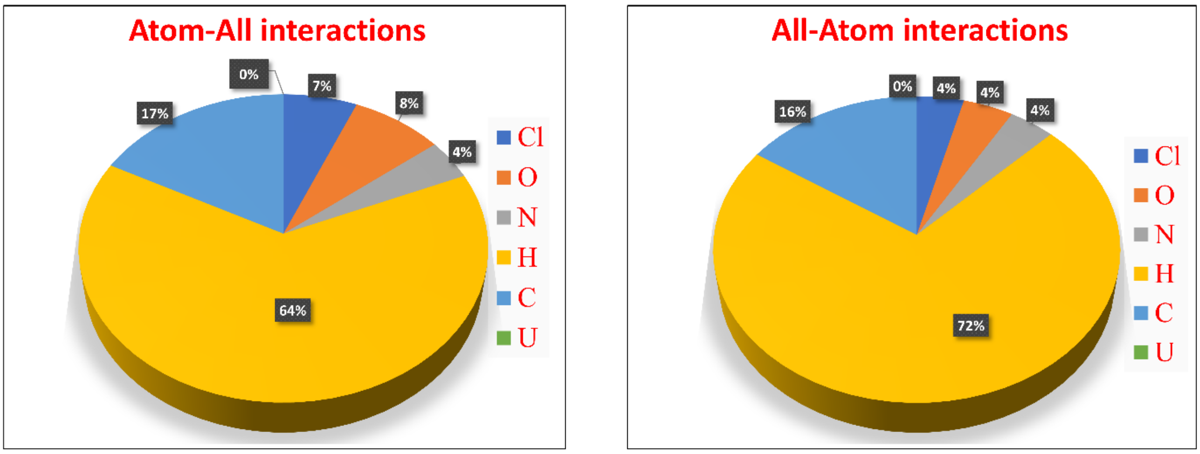

Figure 2c.11 Percentage atom-all and all-atom interactions in complex 5.

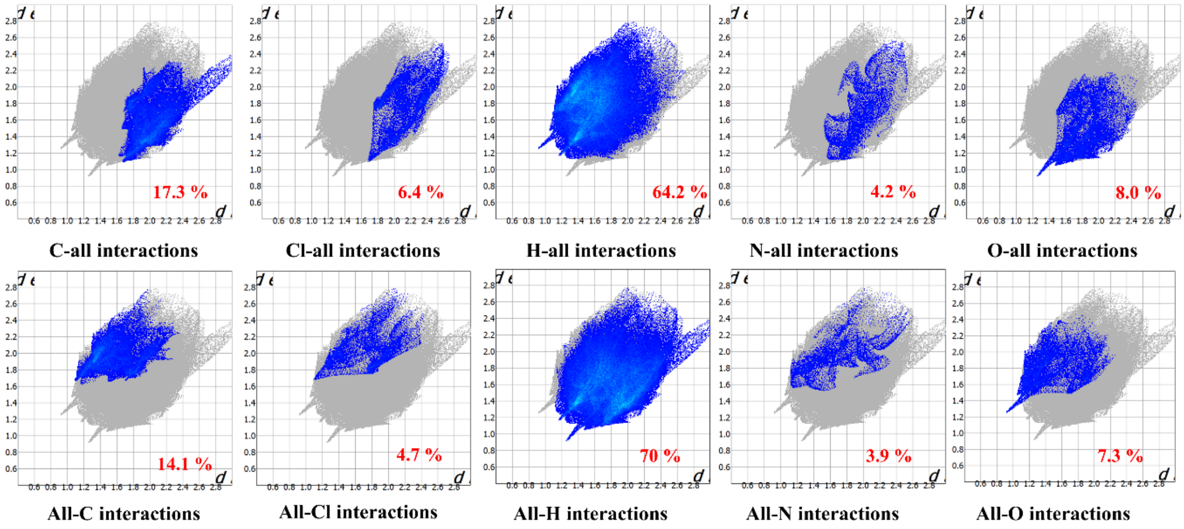

C-all interactions Cl-all interactions H-all interactions N-all interactions O-all interactions

All-C interactions All-Cl interactions All-H interactions All-N interactions All-O interactions

Figure 2c.12 2D Fingerprint map for complex 5.

2c.3.8 Electronic spectral analysis

The UV-Vis electronic spectrum analysis of the complex involved 10^{-6} M solutions in $CHCl_3$, DMF, and DMSO solvents, as depicted in Figure 2c.13. Using the average ratio (β) of LMCT transition values observed for the synthesized complex across all solvents (denoted as ν_{comp} in Table 2c.8) alongside the corresponding ν_{aqua} value (414.7 nm), the δ values were computed using the formula $\delta = \frac{1-\beta}{\beta}$ [42]. In contrast to previous findings detailed in Chapter 2(b), no evidence of solvent binding to the equatorial pentagonal position, as observed in uranyl acylpyrazolone complexes, was detected. Consequently, the trend of covalent character across all solvents remained largely consistent.

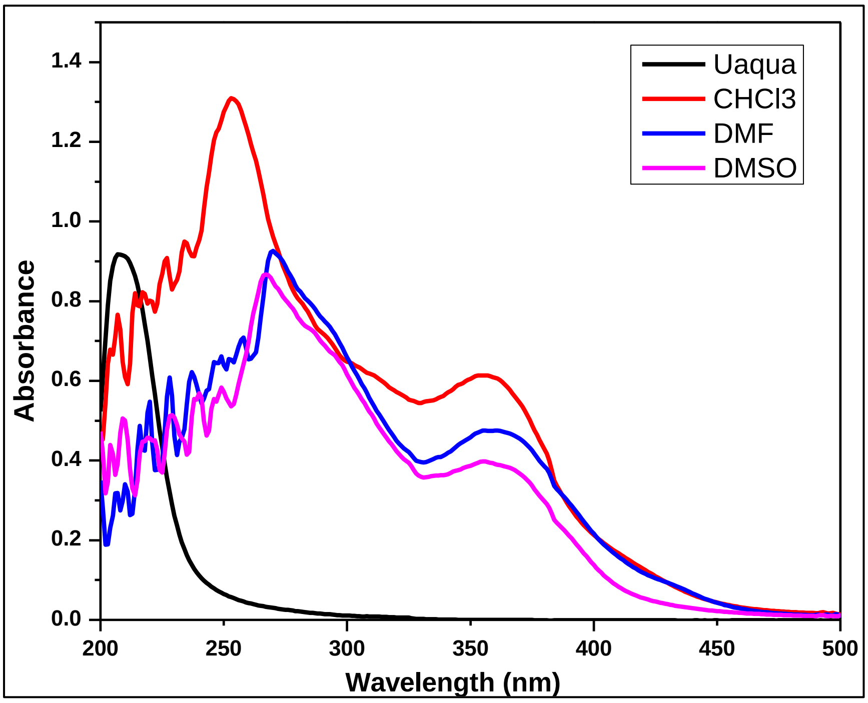

Figure 2c.13 UV-Vis plot for complex 5 in different solvents.

Table 2c.8 Sinha's covalency parameters δ for complex 5 in different solvents.

Solvent	ν_{comp} value (in nm)	$\delta = \frac{1-\beta}{\beta}$
$CHCl_3$	355.3	0.714
DMF	355.6	0.715
DMSO	354.9	0.712

2c.3.9 Electro-chemical studies

The redox potential of the UO_2^{2+}/UO_2^{+} pair directly influences the stability transition from the isolated pentagonal to the hexagonal counterpart. Consequently, cyclic voltammetry (CV) investigations provide a direct means to assess various parameters. Figure 2c.14 depicts the CV plot illustrating the electrochemical redox behaviour of complex 5. The complex exhibits an anodic potential (E_{Ac}) of approximately −0.67 V and a cathodic potential (E_{Pc}) of −0.62 V, indicative of the oxidation of the uranyl ion ($UO_2^{+} \rightarrow UO_2^{2+} + e^{-}$) and its reverse reaction ($UO_2^{2+} + e^{-} \rightarrow UO_2^{+}$). The ΔE value of −0.05 V signifies an irreversible redox reaction [22,35,43].

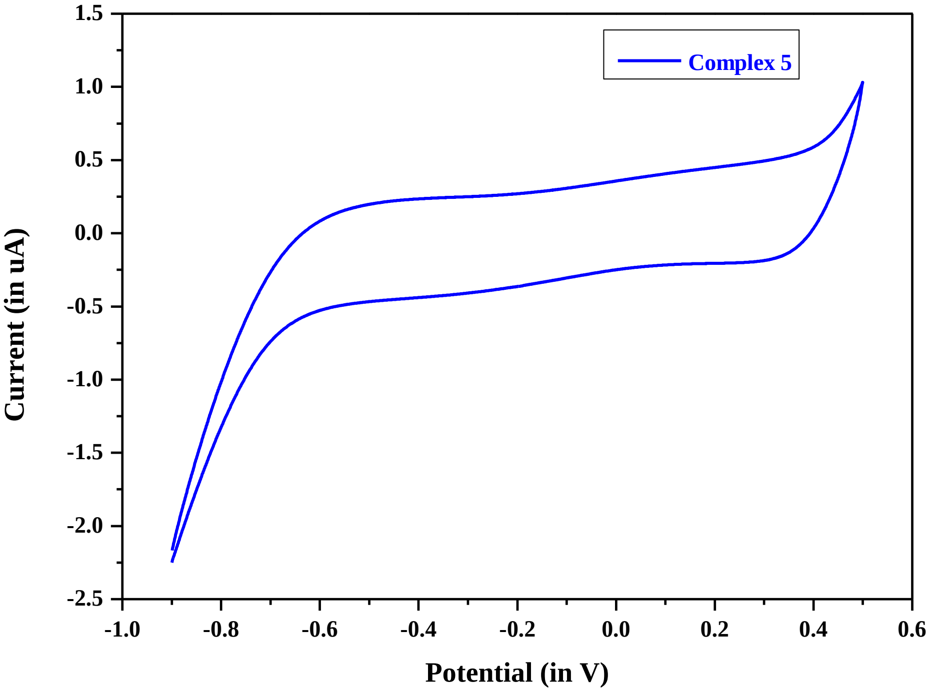

Figure 2c.14 Cyclic voltammogram of complex 5 at 25°C.

2c.4 Conclusions

This study encompasses the synthesis of a mixed ligand complex featuring a stable pentagonal bipyramidal structure, where one bidentate L^5 ligand and one tridentate L^7 ligand occupy the equatorial pentagonal plane. The structural examination of the produced complex primarily relied on FTIR, SCXRD, molar conductance, and TG-DTA techniques. The combined covalency effect of the complex, attributed to both ligands, was investigated, revealing influences from average bond length values on the pentagonal equatorial plane, uranyl axial bond lengths, ligand coordination, and the donor ability of various atoms. Sinha's parameters, derived from UV-Vis data, demonstrated essential uniformity across all solvents, indicating no solvent binding at the equatorial pentagonal site. Computational DFT calculations provided theoretical global index values and other features consistent with experimental data, facilitating a comprehensive understanding of all synthesised compounds' physical and chemical properties. Hirshfeld analysis unveiled the secondary interactions within the uranyl complex crystals. Additionally, CV analysis indicated irreversible reduction behaviour of the complex. The study suggests that a deeper exploration of chemical features and potential applications can be pursued, leveraging the Schiff base of acylpyrazolone and its covalency in uranyl complexes.

References

[1] S. Fustero, M. Sánchez-Roselló, P. Barrio, A. Simón-Fuentes, From 2000 to Mid-2010: A Fruitful Decade for the Synthesis of Pyrazoles, Chem Rev 111 (2011) 6984–7034. https://doi.org/10.1021/cr2000459.

[2] Jensen, B. Skytte, Acta Chemica Scandinavica, Acta Chem Scand 13 (1959) 1668–1670. https://doi.org/10.3891/acta.chem.scand.13-1668.

[3] F. Marchetti, C. Pettinari, R. Pettinari, Acylpyrazolone ligands: Synthesis, structures, metal coordination chemistry and applications, Coord Chem Rev 249 (2005) 2909–2945. https://doi.org/10.1016/j.ccr.2005.03.013.

[4] F. Marchetti, R. Pettinari, C. Pettinari, Recent advances in acylpyrazolone metal complexes and their potential applications, Coord Chem Rev 303 (2015) 1–31. https://doi.org/10.1016/j.ccr.2015.05.003.

[5] F. Marchetti, C. Pettinari, C. Di Nicola, A. Tombesi, R. Pettinari, Coordination chemistry of pyrazolone-based ligands and applications of their metal complexes, Coord Chem Rev 401 (2019) 213069. https://doi.org/10.1016/j.ccr.2019.213069.

[6] C. Deng, S. Abdurehman, L. Liu, D. Wu, D. Jia, R. Zhou, Synthesis, photoisomerization properties and thermal bleaching kinetics of pyrazolones containing 3-cyanobenzal, Spectrochim Acta A Mol Biomol Spectrosc 148 (2015) 318–323. https://doi.org/10.1016/j.saa.2015.04.001.

[7] H. Liu, J. Guo, D. Jia, M. Guo, F. Le, L. Liu, D. Wu, F. Li, Modulation of a solid-state reversible fluorescent photoswitching based on a controllable photochromic pyrazolones, J Solid State Chem 216 (2014) 73–78. https://doi.org/10.1016/j.jssc.2014.04.020.

[8] G. Wang, J. Qin, C.-R. Li, Z. Yang, A highly selective fluorescent probe for Al^{3+} based on quinoline derivative, Spectrochim Acta A Mol Biomol Spectrosc 150 (2015) 21–25. https://doi.org/10.1016/j.saa.2015.05.041.

[9] J. Guo, H. Yuan, D. Jia, M. Guo, Y. Li, Synthesis and improved photochromic properties of pyrazolones in the solid state by incorporation of halogen, Spectrochim Acta A Mol Biomol Spectrosc 171 (2017) 149–154. https://doi.org/10.1016/j.saa.2016.07.052.

[10] H. Chai, G. Liu, L. Liu, D. Jia, Synthesis and spectroscopic study on photochromism of a new thiosemicarbazone compound containing pyrazolone, Spectrochim Acta A Mol Biomol Spectrosc 61 (2005) 2590–2594. https://doi.org/10.1016/j.saa.2004.09.027.

[11] I. Shaikh, R.N. Jadeja, R. Patel, V. Mevada, V.K. Gupta, 4-Acylhydrazone-5-Pyrazolones and their Zinc(II) Metal Complexes: Synthesis, Characterization, Crystal Feature and Antimalarial Activity, J Mol Struct 1232 (2021) 130051. https://doi.org/10.1016/j.molstruc.2021.130051.

[12] I. Shaikh, M. Travadi, R.N. Jadeja, R.J. Butcher, J.H. Pandya, Crystal feature and spectral characterization of Zn(II) complexes containing Schiff base of Acylpyrazolone ligand with antimalarial action, J Indian Chem Soc 99 (2022) 100428. https://doi.org/10.1016/j.jics.2022.100428.

[13] J. Du, J.A. Seed, V.E.J. Berryman, N. Kaltsoyannis, R.W. Adams, D. Lee, S.T. Liddle, Exceptional uranium(VI)-nitride triple bond covalency from ^{15}N nuclear magnetic resonance spectroscopy and quantum chemical analysis, Nat Commun 12 (2021) 5649. https://doi.org/10.1038/s41467-021-25863-2.

[14] L.R. Morss, N.M. Edelstein, J. Fuger, The Chemistry of the Actinide and Transactinide Elements. 3rd edition, 2006. https://doi.org/10.1007/1-4020-3598-5.

[15] L.-M. Zhu, L.-Y. Wang, J.-R. Jin, B.-L. Li, Y. Zhang, Synthesis and structures of two uranyl β-diketonate complexes $[UO_2(DBM)_2(DEDPU)]$ and $[UO_2(PMBP)_2(DEDPU)]$, J Coord Chem 61 (2008) 917–925. https://doi.org/10.1080/00958970701413243.

[16] L.-M. Zhu, S.-W. Wang, B.-L. Li, J.-R. Jin, Y. Zhang, Syntheses and structures of two new uranyl complexes $[UO_2(DPDPU)_2(NO_3)_2](C_6H_5CH_3)$ and $[UO_2(PMBP)_2(DPDPU)](CH_3C_6H_4CH_3)_{0.5}$, J Coord Chem 59 (2006) 1609–1614. https://doi.org/10.1080/00958970600577494.

[17] Yu.M. Chumakov, P.A. Petrenko, F.G. Julea, V.I. Tsapkov, A.P. Gulea, Crystal structure of bis(4-benzoyl-3-methyl-1-phenyl-4,5-dihydro-1H-pyrazol-5-onato)-(ethanol)-dioxourane(VI) ethanol solvate, J Struct Chem 55 (2014) 1116–1119. https://doi.org/10.1134/S0022476614060183.

[18] L. Zhu, D. Yuan, B. Li, H. Li, Syntheses and structures of three disulfoxide uranyl complexes, J Coord Chem 63 (2010) 3006–3015. https://doi.org/10.1080/00958972.2010.505282.

[19] R.C. Maurya, M.N. Jaiswal, R. Verma, B. Shukla, The Coordination Chemistry of Dioxouranium(VI): Studies on Some Novel Di- and Trinuclear Dioxouranium(VI) Complexes with Pyrazolone Based Schiff Bases, Synth React Inorg Met Org Chem 28 (1998) 1265–1281. https://doi.org/10.1080/00945719809349404.

[20] A.T. Mubarak, Structural model of dioxouranium(VI) with hydrazono ligands, Spectrochim Acta A Mol Biomol Spectrosc 61 (2005) 1163–1170. https://doi.org/10.1016/j.saa.2004.06.036.

[21] A.I. Vogel, Vogel's textbook of quantitative chemical analysis, Fifth edition. Harlow, Essex, England: Longman Scientific & Technical; New York: Wiley, 1989. https://search.library.wisc.edu/catalog/999612906602121.

[22] A.K. Patel, R.N. Jadeja, H. Roy, R.N. Patel, S.K. Patel, R.J. Butcher, Pseudo-tetrahedral copper(II) complex derived from N'-[(2E,3Z)-4-hydroxy-4-phenylbut-3-en-2-ylidene]acetohydrazide: Synthesis, molecular structure, quantum chemical investigations, antioxidant and antiproliferative properties, J Mol Struct 1185 (2019) 341–350. https://doi.org/10.1016/j.molstruc.2019.03.004.

[23] G.M. Sheldrick, SHELXT – Integrated space-group and crystal-structure determination, Acta Crystallogr Section A 71 (2015) 3–8. https://doi.org/10.1107/S2053273314026370.

[24] G.M. Sheldrick, Crystal structure refinement with SHELXL, Acta Crystallogr Section C 71 (2015) 3–8. https://doi.org/10.1107/S2053229614024218.

[25] I. Shaikh, R.N. Jadeja, R. Patel, Three mixed ligand mononuclear Zn(II) complexes of 4-acyl pyrazolones: Synthesis, characterization, crystal study and anti-malarial activity, Polyhedron 183 (2020) 114528. https://doi.org/10.1016/j.poly.2020.114528.

[26] W.R. Wadt, P.J. Hay, Ab initio effective core potentials for molecular calculations. Potentials for main group elements Na to Bi, J Chem Phys 82 (1985) 284–298. https://doi.org/10.1063/1.448800.

[27] P.J. Hay, W.R. Wadt, Ab initio effective core potentials for molecular calculations. Potentials for the transition metal atoms Sc to Hg, J Chem Phys 82 (1985) 270–283. https://doi.org/10.1063/1.448799.

[28] J.J. Koenderink, A.J. van Doorn, Surface shape and curvature scales, Image Vis Comput 10 (1992) 557–564. https://doi.org/10.1016/0262-8856(92)90076-F.

[29] M.J., Frisch, G.W., Trucks, H.B., Schlegel, G.E., Scuseria, M.A., Robb, J.R., Cheeseman, G., Scalmani, V., Barone, B., Mennucci, G.A., Petersson, H., Nakatsuji, M., Caricato, X., Li, H.P., Hratchian, A.F., Izmaylov, J., Bloino, G., Zheng, J.L., Sonnenberg, M., Hada, M., Ehara, K., Toyota, R., Fukuda, J., Hasegawa, M., Ishida, T., Nakajima, Y., Honda, O., Kitao, H., Nakai, T., Vreven, J.A., Montgomery, Jr., J.E., Peralta, F., Ogliaro, M., Bearpark, J.J., Heyd, E., Brothers, K.N., Kudin, V.N., Staroverov, R., Kobayashi, J., Normand, K., Raghavachari, A., Rendell, J.C., Burant, S.S., Iyengar, J., Tomasi, M., Cossi, N., Rega, J.M., Millam, M., Klene, J.E., Knox, J.B., Cross, V., Bakken, C., Adamo, J., Jaramillo, R., Gomperts, R.E., Stratmann, O., Yazyev, A.J., Austin, R., Cammi, C., Pomelli, J.W., Ochterski, R.L., Martin, K., Morokuma, V.G., Zakrzewski, G.A., Voth, P., Salvador, J.J., Dannenberg, S., Dapprich, A.D., Daniels, Ö., Farkas, J.B., Foresman, Orti., Gaussian 09, Revision E.01, Gaussian, Inc., Wallingford, CT (2013).

[30] J.J. Koenderink, A.J. van Doorn, Surface shape and curvature scales, Image Vis Comput 10 (1992) 557–564. https://doi.org/10.1016/0262-8856(92)90076-F.

[31] M. Dolg, U. Wedig, H. Stoll, H. Preuss, Energy-adjusted ab initio pseudopotentials for the first row transition elements, J Chem Phys 86 (1987) 866–872. https://doi.org/10.1063/1.452288.

[32] G.A. Petersson, M.A. Al-Laham, A complete basis set model chemistry. II. Open-shell systems and the total energies of the first-row atoms, J Chem Phys 94 (1991) 6081–6090. https://doi.org/10.1063/1.460447.

[33] W.J. Geary, The use of conductivity measurements in organic solvents for the characterisation of coordination compounds, Coord Chem Rev 7 (1971) 81–122. https://doi.org/10.1016/S0010-8545(00)80009-0.

[34] G.D. Jarvinen, A.J. Zozulin, E.M. Larson, R.R. Ryan, Structure of bis(4-benzoyl-2,4-dihydro-5-methyl-2-phenyl-3H-pyrazol-3-onato-O,O’)dinitratobis(triphenylphosphine

oxide-O)thorium(IV), Acta Crystallogr Section C 47 (1991) 262–264. https://doi.org/10.1107/S0108270190002177.

[35] K. Mizuguchi, Y.-Y. Park, H. Tomiyasu, Y. Ikeda, Electrochemical and Spectroelectrochemical Studies on Uranyl Carbonato and Aqua Complexes, J Nucl Sci Technol 30 (1993) 542–548. https://doi.org/10.1080/18811248.1993.9734516.

[36] B.E. Klamm, C.J. Windorff, C. Celis-Barros, M.L. Marsh, T.E. Albrecht-Schmitt, Synthesis, Spectroscopy, and Theoretical Details of Uranyl Schiff-Base Coordination Complexes, Inorg Chem 59 (2020) 23–31. https://doi.org/10.1021/acs.inorgchem.9b00477.

[37] R.R. Ryan, G.D. Jarvinen, Structure of bis(4-benzoyl-2,4-dihydro-5-methyl-2-phenyl-3 H-pyrazol-3-onato- O,O')(dimethyl sulfoxide- O)dioxouranium(VI), Acta Crystallogr Section C 43 (1987) 1295–1298. https://doi.org/10.1107/S0108270187092114.

[38] Y. Singh, R.N. Patel, S.K. Patel, A.K. Patel, N. Patel, R. Singh, R.J. Butcher, J.P. Jasinski, A. Gutierrez, Experimental and quantum computational study of two new bridged copper(II) coordination complexes as possible models for antioxidant superoxide dismutase: Molecular structures, X-band electron paramagnetic spectra and cryogenic magnetic properties, Polyhedron 171 (2019) 155–171. https://doi.org/10.1016/j.poly.2019.07.015.

[39] R.N. Patel, S.K. Patel, D. Kumhar, N. Patel, A.K. Patel, R.N. Jadeja, N. Patel, R.J. Butcher, M. Cortijo, S. Herrero, Two new copper(II) binuclear complexes with 2-[(E)-(pyridine-2yl-hydrazono)methyl]phenol: Molecular structures, quantum chemical calculations, cryomagnetic properties and catalytic activity, Polyhedron 188 (2020) 114687. https://doi.org/10.1016/j.poly.2020.114687.

[40] C.F. Mackenzie, P.R. Spackman, D. Jayatilaka, M.A. Spackman, CrystalExplorer model energies and energy frameworks: extension to metal coordination compounds, organic salts, solvates and open-shell systems, IUCrJ 4 (2017) 575–587. https://doi.org/10.1107/S205225251700848X.

[41] P.R. Spackman, M.J. Turner, J.J. McKinnon, S.K. Wolff, D.J. Grimwood, D. Jayatilaka, M.A. Spackman, CrystalExplorer: a program for Hirshfeld surface analysis,

visualization and quantitative analysis of molecular crystals, J Appl Crystallogr 54 (2021) 1006–1011. https://doi.org/10.1107/S1600576721002910.

[42] S.P. Sinha, Spectroscopic investigations of some neodymium complexes, Spectrochim Acta 22 (1966) 57–62. https://doi.org/10.1016/0371-1951(66)80008-5.

[43] G. Nocton, P. Horeglad, V. Vetere, J. Pécaut, L. Dubois, P. Maldivi, N.M. Edelstein, M. Mazzanti, Synthesis, Structure, and Bonding of Stable Complexes of Pentavalent Uranyl, J Am Chem Soc 132 (2010) 495–508. https://doi.org/10.1021/ja9037164.

Published Papers:

ACS OMEGA

http://pubs.acs.org/journal/acsodf

Article

Synthesis, Covalency Sequence, and Crystal Features of Pentagonal Uranyl Acylpyrazolone Complexes along with DFT Calculation and Hirshfeld Analysis

Maitrey Travadi, Rajendrasinh N. Jadeja,* and Ray J. Butcher

Cite This: https://doi.org/10.1021/acsomega.2c03923

Read Online

ACCESS | Metrics & More | Article Recommendations | Supporting Information

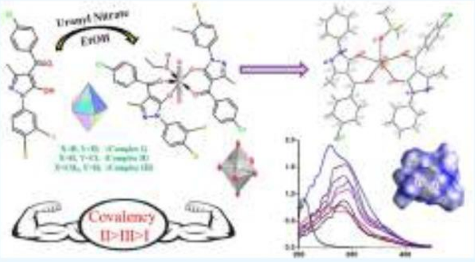

ABSTRACT: Three uranyl acylpyrazolone complexes [$UO_2(PCBPMP)_2(CH_3CH_2OH)$] (complex I), [$UO_2(PCBMCPMP)_2(CH_3CH_2OH)$] (complex II), and [$UO_2(PCBPTMP)_2(CH_3CH_2OH)$] (complex III) were synthesized from σ-donating acypyrazolone ligands to analyze their sequence of covalent characteristics, reactivity, and redox properties (PCBPMP: *p*-chlorobenzoyl 1-phenyl 3-methyl 5-pyrazolone; PCBMCPMP: *p*-chlorobenzoyl 1-(*m*-chlorophenyl) 3-methyl 5-pyrazolone; PCBPTMP: *p*-chlorobenzoyl 1-(*p*-tolyl) 3-methyl 5-pyrazolone). An examination of the structure, pentagonal bipyramidal geometry, and composition of these complexes was conducted mainly through their single-crystal X-ray diffraction (XRD) data, ^{1}H nuclear magnetic resonance (NMR) δ-values, plots of thermogravimetric-differential thermal analysis (TG-DTA), significant Fourier transform infrared (FTIR) vibrations, gravimetric estimation, and molar conductivity values. The covalency order was found to be complex II > III > I, which mainly depends on values of stretching frequencies, average bond lengths of axial uranyl bonds, values of average bond lengths on the pentagonal equatorial plane, solvent coordination on the fifth site of a pentagonal plane, and the type of aryl group on the nitrogen of the pyrazolone ring. This was confirmed by FTIR spectroscopy and single-crystal spectral characterization. To verify experimental results by comparison with theoretical results, density functional theory (DFT) calculations were carried out, which further gives evidence for the covalency order through theoretical frequencies and the gap of highest occupied molecular orbital (HOMO)−lowest unoccupied molecular orbital (LUMO) energies. Theoretical bond properties were also examined by the identification of global index parameters. Intermolecular noncovalent surface interactions were studied by the Hirshfeld surface analysis. The irreversible redox behavior of uranyl species was identified through electrochemical cyclic voltammetry-differential pulse voltammetry (CV-DPV) plot analysis.

1. INTRODUCTION

The application of actinides in the fields of nuclear weapons, defense operations, and energy production has been increasing in the last few decades.[1−3] As a part of their application in the nuclear fuel cycle and weapon synthesis, uranium and plutonium speciation is necessary to understand their migration methods.[4] Uranium and Thorium are the most important of the many elements of the actinide series as enduring elements to understand their properties by building complexes. In the field of coordination chemistry, solvent extraction is a crucial method among the current techniques for the separation of actinide series.[5,6] Because of the various ionic and covalent characteristics, the ion-exchange approach is also a feasible and powerful method for their separation.[7]

Despite many exceptional separation methods being available, it is very difficult and dangerous to explore all details of actinides in addition to being expensive. In such a situation, studying a less-expensive element as a representative of a few elements is significant. Although the chemistry of uranium is different from that of other actinides, the ^{238}U isotope of uranium is easily available at reasonable prices and superior to other minor actinides such as americium and curium at present. Redox variability is a vital concept in separation and corrosion science because uranium can exist in different oxidation states.[8] Moreover, due to a simple synthesis method and the instantaneous crystal-forming capacity of uranium complexes, they are preferably studied among the actinides series by most of the viable approaches mentioned. In terms of efficacy, there are numerous advantages of uranium such as its

Received: June 27, 2022
Accepted: August 9, 2022

Polyhedron 223 (2022) 115956

Contents lists available at ScienceDirect

Polyhedron

journal homepage: www.elsevier.com/locate/poly

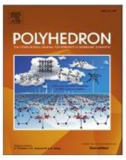

Synthesis, covalency parameters, energy calculations and crystal features of acylpyrazolone derived pentavalent Uranyl complex along with DFT and Hirshfeld analysis

Maitrey Travadi[a], R.N. Jadeja[a,*], Ray J. Butcher[b]

[a] Department of Chemistry, Faculty of Science, The Maharaja Sayajirao University of Baroda, Vadodara 390002, India
[b] Department of Inorganic & Structural Chemistry, Howard University, Washington, DC 22031, USA

ARTICLE INFO

Keywords:
Uranyl acylpyrazolone complex
Pentavalent bipyramidal geometry
Sinha's covalency parameters
Global index parameters
DFT
Interaction energies
Energy frameworks
And Hirshfeld analysis

ABSTRACT

A σ-donating acylpyrazolone DMBPMP (4-(3,5-dimethyl benzoyl) 1-phenyl 3-methyl 5-pyrazolone) ligand and its Uranyl acylpyrazolone complex [$UO_2(DMBPMP)_2(EtOH)$] were synthesized to analyze the nature of covalency, reactivity, and redox properties. The structure, pentavalent bipyramidal geometry, and complex composition are mainly scrutinized through their single-crystal x-ray crystal data, molar conductivity, gravimetric estimation, FTIR significant vibrations, δ-values of ^{1}H NMR, ^{13}C NMR and TG-DTA plots. The covalency of the Uranyl complex mainly depends on average bond length values on the pentagonal equatorial plane, Uranyl axial bond lengths, stretching frequency values, coordinated solvent on the fifth coordination site, and different aryl group substitution on the first position of the pyrazolone ring; and it can be confirmed through FTIR, single-crystal, and electronic UV–Vis spectral characterization methods. The UV–Vis data was also valuable for identifying n → π*, π → π*, and LMCT transitions and calculating Sinha's covalency parameters, which shows that the complex can show maximum covalent character in DMSO solvent and covalency decreases in DMSO > DMF > Ethyl acetate > Ethanol > $CHCl_3$ order. DFT calculations were performed to get an excellent correlation and comparison with all experimental values. This correlation and comparision is helpful to identify global index parameters to get an idea of the physical as well as chemical properties of such systems and to confirm the characteristics theoretically by HOMO-LUMO energy gap, theoretical vibrations, natural electronic configuration, and NBO charges. The Hirshfeld surface analysis was also carried out to identify the crystal strength through interaction energies and energy frameworks in the ligand and intermolecular non-covalent surface interactions with fingerprint plot details in both ligand and complex. Electro-chemical analysis in CV-DPV plots provides information on the redox properties of uranyl moiety.

1. Introduction

In addition to the larger size, the f-block elements located at the bottom of the periodic table have a much more unique colour, source, texture, properties and utility than other block elements. In all these elements, the Actinide series has many challenges for their study, examination and characterization due to lesser production (in nanograms), anomalous chemical properties, larger size, radioactive behaviour, and shorter lifetime. Still, the significance of the Actinide series for nuclear weapon synthesis, energy production, optical instruments, and defense operations has been increasing in the research area over the past few years [1-3]. As part of applications in the weapon synthesis and nuclear energy fuel cycle, the speciation of Uranium and Plutonium are well known for their migration pathways [4]. Due to transuranium elements' volatile and reactive nature, only Uranium and Thorium are the essential elements of the actinide series as enduring elements to understand their properties by building complexes. Many separation methods like fractional crystallization, fractional precipitation, solvent extraction, ion exchange, etc., play a vital role in analyzing the characteristics of actinides for application purposes and play an essential function in the modern-day actinide series separation method [5,6]. An ion-exchange method is also prevalent and effective in the separation method due to the diverse ionic and covalent characteristics of actinides [7].

Despite many different separation methods, it is extremely difficult,

---

Abbreviations: HSAB, Hard and soft acid-base; DMBPMP, 4-(3,5-dimethyl benzoyl 1-phenyl 3-methyl 5-pyrazolone.

* Corresponding author.

E-mail address: rjadeja-chem@msubaroda.ac.in (R.N. Jadeja).

https://doi.org/10.1016/j.poly.2022.115956
Received 11 May 2022; Accepted 6 June 2022

Journal of Molecular Structure 1281 (2023) 135137

Contents lists available at ScienceDirect

Journal of Molecular Structure

journal homepage: www.elsevier.com/locate/molstr

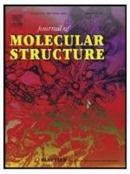

Uranyl(VI) Mixed-ligand complex synthesis and characterization using 4-acylhydrazone-5-pyrazolone and 4-acylpyrazolone: Covalency, crystal assay, DFT study and Hirshfeld analysis

Maitrey Travadi[a], Rajendrasinh N. Jadeja[a,*], Ray J. Butcher[b]

[a] Department of Chemistry, Faculty of Science, The Maharaja Sayajirao University of Baroda, Vadodara 390002, India
[b] Department of Inorganic & Structural Chemistry, Howard University, Washington, DC 22031, USA

ARTICLE INFO

Article history:
Received 24 November 2022
Revised 12 January 2023
Accepted 8 February 2023
Available online 10 February 2023

Keywords:
Bidentate acylpyrazolone ligand
Tridentate Schiff base ligand
Pentagonal bipyramidal uranyl complex
Sinha's parameter
Global index values
Hirshfeld analysis

ABSTRACT

Newly prepared bidentate HL^A and tridentate Bz-HL^A ligands were used to synthesize the novel uranyl mixed ligand $[UO_2(HL^A)(Bz\text{-}HL^A)]$ complex with pentagonal bipyramidal geometry. HL^A ligand was prepared via the common acylation method, and the Bz-HL^A ligand was prepared using the Schiff base reaction of HL^A with a benzohydrazide molecule. FTIR, ^1H and ^{13}C NMR, SCXRD, molar conductance, and TG-DTA were mainly implemented to examine the structure of produced compounds. The combined covalency effect of complex due to both ligands has been studied, which was discovered to be influenced by the average bond length values on the pentagonal plane, uranyl axial bond lengths, ligand coordination, and donor ability of various atoms. To demonstrate that solvents have no impact on the covalency of the synthesised complex, Sinha's covalency parameters were computed using UV–vis data. DFT calculations were performed in order to validate experimental findings in comparison to theoretical findings, and theoretical bond characteristics were also investigated through the recognition of global index values. Hirshfeld surface analysis was used to examine the crystal strength, energy characteristics and non-covalent surface interactions. Analysis using cyclic voltammetry(CV) shows that the complex is irreversibly reducing. Understanding the Schiff base of acylpyrazolones and their covalency in uranyl complexes allow for the investigation of a wide range of chemical properties and applications.

1. Introduction

The well-known synthon pyrazolone is used to create a variety of compounds with tremendous potential for advancements in the fields of medicinal and coordination chemistry [1]. According to Jensen, the acylation technique is becoming more popular for creating chelating ligands with increasing donor atom abilities [2]. It is common to find a lot of these acylated pyrazolones as well as their complexes in different geometries [3,4]. One reaction that distinguishes acylpyrazolones is the formation of Schiff bases, which boosts donor ability and denticity in the coordination background [5]. There are several uses for schiff bases formed from hydrazine-based compounds with acylpyrazolones [6–10], but tridentate ligands obtained from benzohydrazides are notably well-recognised for their O–N–O donor sites [11,12]. These aforementioned ligands can combine with inner transition metals to produce complexes with a range of geometries, including pentagonal bipyramidal, tricapped trigonal prismatic, square antiprismetic, etc. [5].

The nature and amount of covalency must be determined since it is arduous to identify the features of inner transition metal complexes and because covalency serves as the foundation for descriptions of the bonding of Ln-acylpyrazolones [13]. Growing interest has been shown in the study of Ln-acylpyrazolone bonding because these compounds' bonds frequently exhibit covalency criteria that may be easily measured. Since actinides have a number of notable drawbacks, including radioactivity, larger size, lower lifetime, very expensive, dangerous, etc., they are typically not investigated in the research. In this case, it can be important to consider a readily accessible element as a representation of a few other elements. Although the chemistry of uranyl differs from that of other actinides, it is more readily available and more advantageous today than minor actinides like americium and curium [14,15].

Research on various stable compounds with UO_2^{2+} has led to the enlargement of uranyl acylpyrazolone complexes, which provide a wide range of growth options. Numerous pentagonal bipyramidal uranyl acylpyrazolones were produced due to their simplicity of synthesis and crystal-forming capacity [16–19]. A few diox-

---

* Corresponding author.
E-mail address: rjadeja-chem@msubaroda.ac.in (R.N. Jadeja).

https://doi.org/10.1016/j.molstruc.2023.135137